

10
15
20
25

AD-A270 834

UMENTATION PAGE

Form Approved
OMB No. 2304-0188

19

4. TITLE AND SUBTITLE		REPORT DATE August 23, 1993	3. REPORT TYPE AND DATES COVERED 4/1/90-3/31/93
Suppressed Electron-Phonon Scattering in Superlattices		5. FUNDING NUMBERS DAAL03-90-G-0083	
6. AUTHOR(S) Y.-P. Chen, A. Clark, L.F. Eastman, T. LeTran, P. Mandeville, H.C. Park, B.K. Ridley, W.J. Schaff, T.-K. Yoo		7. PERFORMING ORGANIZATION NAME(S) AND ADDRESS(ES) Cornell University School of Electrical Engineering Ithaca, New York 14853-5401	
8. PERFORMING ORGANIZATION REPORT NUMBER (Final)			
9. SPONSORING MONITORING AGENCY NAME(S) AND ADDRESS(ES) U.S. Army Research Office P. O. Box 12211 Research Triangle Park, NC 27709-2211		10. SPONSORING MONITORING AGENCY REPORT NUMBER ARO 26 755.5-EL	
11. SUPPLEMENTARY NOTES The view, opinions and/or findings contained in this report are those of the author(s) and should not be construed as an official Department of the Army position, policy, or decision, unless so designated by other documentation.			
12a. DISTRIBUTION AVAILABILITY STATEMENT Approved for public release; distribution unlimited.		12b. DISTRIBUTION CODE	
13. ABSTRACT (Maximum 200 words) This report covers a three-year study of scattering of electrons by phonons in superlattices. The usual bulk polar optical phonons were confined to the quantum wells by the abrupt interfaces with the barriers. In short period superlattices this in turn would be expected to lower the rate of scattering of electrons by these phonons. This study showed that the room temperature mobility was reduced, rather than enhanced as expected from the phonon confinement. Interface phonon scattering was studied to show that it was the cause of the reduced mobility at room temperature. At lower temperatures, such as 77K and lower, the electron mobility measured was higher in the short period superlattice case when the barriers seen by the electrons were AlAs. In order to avoid the interface phonon scattering, a graded composition quantum well was used. Devices made from such structures had improved electron mobility, breakdown voltage, and gate leakage.			
14. SUBJECT TERMS 		15. NUMBER OF PAGES 84	
		16. PRICE CODE	
17. SECURITY CLASSIFICATION OF REPORT UNCLASSIFIED	18. SECURITY CLASSIFICATION OF THIS PAGE UNCLASSIFIED	19. SECURITY CLASSIFICATION OF ABSTRACT UNCLASSIFIED	20. LIMITATION OF ABSTRACT UL

187, 1540 9, 130 3500

A standard linear barcode is located in the bottom right corner of the page.

14. SUBJECT TERMS

15. NUMBER OF PAGES

84

16. PRICE CODE

17. SECURITY CLASSIFICATION
OF REPORT
UNCLASSIFIED

18. SECURITY CLASSIFICATION
OF THIS PAGE
UNCLASSIFIED

19. SECURITY CLASSIFICATION
OF ABSTRACT
UNCLASSIFIED

20. LIMITATION OF ABSTRACT

**Best
Available
Copy**

Suppressed Electron-Phonon Scattering in Superlattices
Final Report

Y.-P. Chen,
A. Clark,
L.F. Eastman,
T. LeTran,
P. Mandeville,
H.C. Park,
B.K. Ridley,
W.J. Schaff,
T.-K. Yoo

August 1993

U.S. Army Research Office

DAAL03-90-G-0083
26755-EL

Cornell University
Ithaca, New York 14853

APPROVED FOR PUBLIC RELEASE;
DISTRIBUTION UNLIMITED.

Accession For	
NTIS	CRA&I
DTIC	TAB
Unannounced	
Justification	
By	
Distribution /	
Availability Codes	
Dist	Avail and / or Special

The views, opinions, and/or finds contained in this report are those of the author(s) and should not be construed as an official Department of the Army position, policy, or decision, unless so designated by other documentation.

Table of Contents

	Page
I. Overview - L.F. Eastman	1
II. On the Suppression of Phonon-Electr in Short Periodic AlAs/GaAs Multiple Structures - T.T. LeTran, W.J. Schaff, B.K. Ridley, Y.-P. Chen, A. Clark, S. O'Keefe, and L.F. Eastman	2
2.1 Abstract	2
2.2 Introduction	2
2.3 Samples	3
2.4 Data and Discussions	6
2.5 Conclusions	9
2.6 References	11
III. Optical Mode Hybrids in Quantum Wells, Superlattices and Slabs - B.K. Ridley	14
3.1 Abstract	14
3.2 Introduction	14
3.3 Continuum Optica Modes	15
3.4 Boundary Conditions	17
3.5 Hybrid Optical Modes	18
3.6 Interaction with Electrons	19
3.7 Results	21
3.8 Conclusions	31
3.9 References	32
IV. Double Modulation-Doped AlGaAs/InGaAs Heterostructure with a Graded Composition in the Quantum Well - T.-K. Yoo, P. Mandeville, H. Park, W.J. Schaff, and L.F. Eastman	34
V. Publications	37
VI. Personnel	38
VII. Inventions	38
Appendix Papers Published	39

I. Overview - L.F. Eastman

Both experimental and theoretical studies have been made on the use of AlAs/GaAs short period superlattices to suppress phonon-electron scattering, for improved electron transport parallel to the heterojunctions. The structures would be applicable to MODFET devices. These two efforts, experimental and theoretical, are reported separately in the following two sections. In spite of the confinement of the GaAs polar optical phonons in the short period superlattice channels, the electrons had lower mobility at room temperature than they would have in a single, thick GaAs channel. The added scattering by phonons due to the added abrupt heterojunction interfaces was determined to be the cause of the reduced mobility. The abrupt interfaces that occur, even with a single, uniform composition channel, also limit the room-temperature mobility. In order to concentrate the electrons in the region of the channel away from the interfaces, graded InGaAs, with a higher Indium fraction in the center of the channel was studied. This yielded 10% higher mobility at room temperature, and MODFET's fabricated from the graded-channel material showed other important improvements in breakdown voltage and gate leakage. A reprint by a visitor is attached to cover this important new concept, for which an invention disclosure has been filed at Cornell. A new project on the graded-composition channel has been initiated with ARO and ARL support.

II. On the Suppression of Phonon-Electron Scattering in Short Periodic
AlAs/GaAs Multiple Quantum Well Structures - T. T. LeTran, W.J.
Schaff, B.K. Ridley, Y.P. Chen, A. Clark, S. O'Keefe, and L. F.
Eastman

2.1 Abstract

The suppression of longitudinal optical phonon (LOP)-electron scattering was sought in multiple quantum well (MQW) structures. The structures had GaAs well widths - 12, 15 and 20 mono-layers (ML) and AlAs barrier widths = 2 and 4 ML. The MQWs were grown in the channel of GaAs/Al_{0.3}Ga_{0.7}As modulation doped field effect transistors (MODFETs) without gates. The Hall mobility and carrier sheet density were measured by the van der Pauw method. The Hall mobility of the MQW samples were found to be less than that of the control samples (without MQW) at room temperature, but was better at temperatures lower than 50 K. The reduction of the room temperature mobility was due to interaction of the well electrons with the interface polaritions from the AlAs barriers. The increase of the low temperature mobility was due to reduced remote ionized impurity scattering of the well electrons. The evidence of performance improvement of MQW devices at room temperature due to suppression of electron-LOP scattering is thus disputed by this study. The results of an experiment made elsewhere, which appeared to show the contrary, can be interpreted using arguments other than the suppression of electron-LOP scattering in MWQs.

2.2 Introduction

In recent years, the possibility of electron mobility enhancement by suppression of phonon-electron interaction in multi-quantum well (MQW) structures has raised considerable interest 1-5. The suppression is sought by the confinement of longitudinal optical phonons (LOP) inside the

quantum wells that have different coupling constant and ion masses than the barriers. The interaction of 2D-LOP/2D-electrons gets weaker as the well width decreases, in contrast to the 3D-LOP/2D-electron system.² On the other hand, interface polariton (IP) interaction with free carriers becomes more important as the well width decreases in systems of finite barriers.³⁻⁵

A study of several different GaAs/AlAs multi-quantum well samples is reported here. It indicates that there may be an upper limit of electron mobility parallel to the AlAs/GaAs MQW plane due to the interplay between LOP and IP scattering of electrons. This study confirms the importance of IP scattering in very narrow wells (12 to 20 atomic layers). The latter is shown to outweigh the benefit of suppression of LOP scattering.

2.3 Samples

Two control samples and MQW structures of different well and barrier widths were examined. Fig. 2.1 shows the first control sample's (REF) structure. The 2000Å n-GaAs cap layer, the 800Å Al_{0.3}Ga_{0.7}As uniform donor layer, the 150Å spacer layers and the GaAs channel were grown by MBE on (100) GaAs at 620°C. The donor concentration was 2x8¹⁸ cm⁻³. The second control sample, REF+4, is similar to the REF, except that there is a 4 ML thick AlAs-barrier between the spacer and the channel. All parameters in the other samples were kept the same as the REF's, except that they have AlAs/GaAs multiple quantum well in their channel. Six such samples were studied: MQW(12/2), MQW(15/2), MQW(20/2), MQW(12/4), MQW(15/4), MQW(20/4), where the numbers in brackets represent the well and barrier widths in number of ML, respectively. Fig. 2.2 shows the band structure of the MQW(15/4) sample. Note the large density of the low mobility electrons in the cap and donor layers.

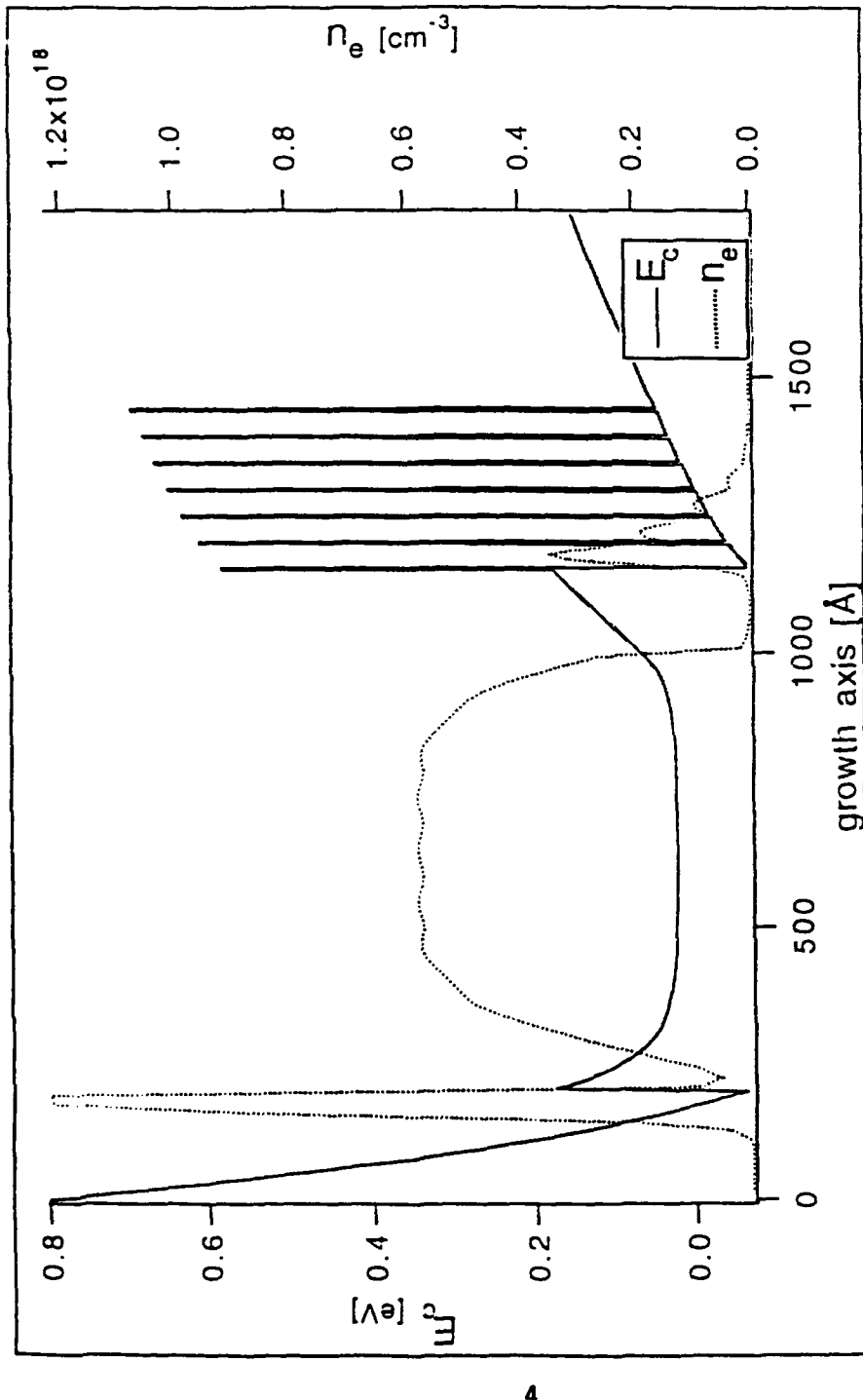


Figure 2.1. The structure of the control sample REF. It consists of a 200 Å n-GaAs cap layer, a 800 Å Al_{0.3}Ga_{0.7}As uniform donor layer (2 × 10¹⁸ cm⁻³ n-doped), a 150 Å spacing layers and the GaAs channel. The REF+4 has an additional 4 ML of AlAs between the spacer and the channel. The energy band E_c is shown by the solid line; the bulk density of free electrons is shown by the dotted line.

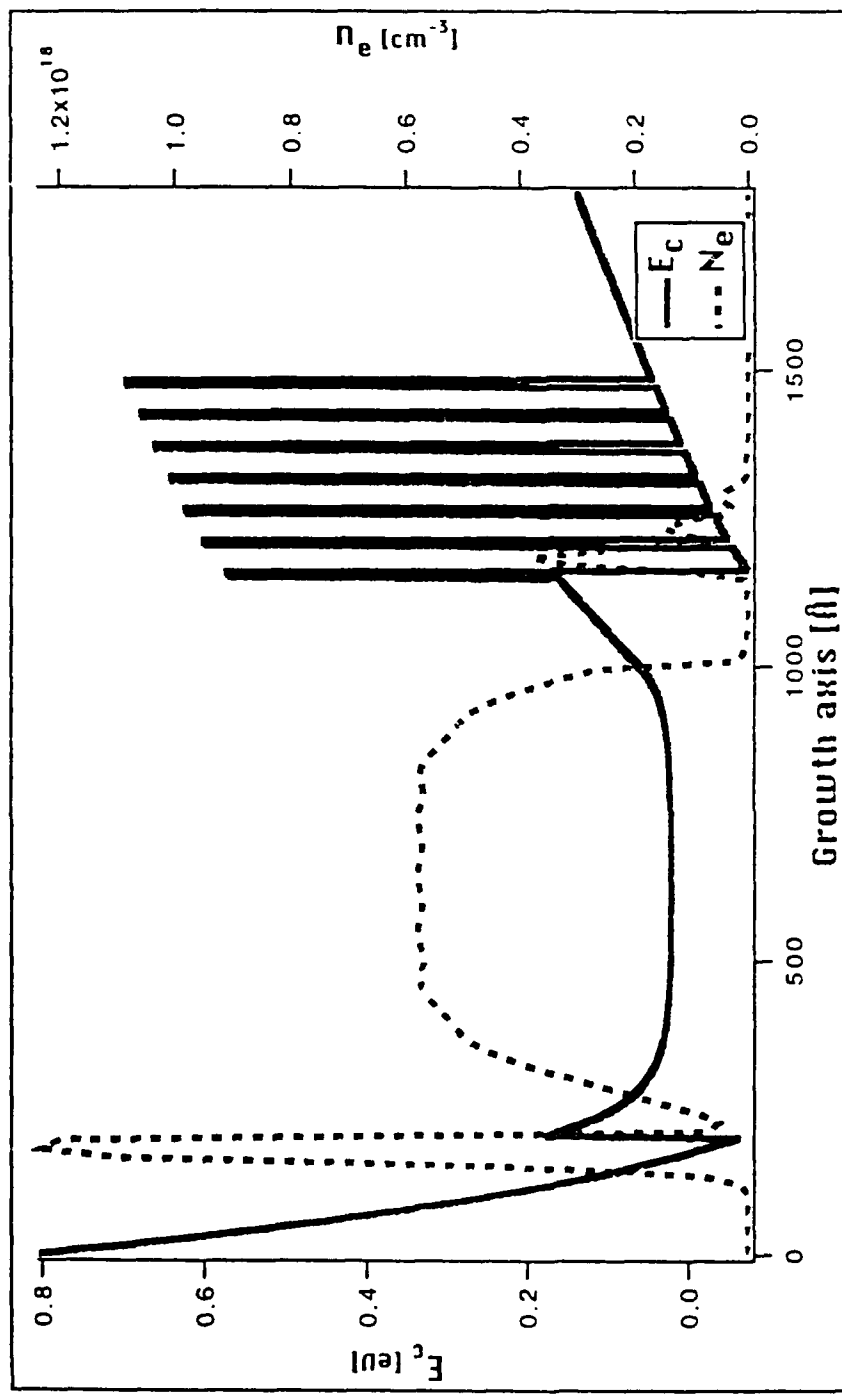


Figure 2.2. The structure of a typical MQW sample, the MQW(15/4). It consists of the REF plus a short periodic MQW structure in its channel. The energy band E_c is shown by the solid line; the bulk density of free electrons is shown by the dotted line.

The barriers in the MQW samples were kept thin to minimize the possibility of carriers being scattered into the X-valleys of AlAs, while still being large enough to confine LOP to within the wells. For example, the energy gap between the X-level of the AlAs barrier and the first Γ -level of the GaAs well is 0.38 eV in the MQW(15/2) sample. The fraction of the well's electrons being scattered into the barriers is approximately 10^{-7} . In the MQW(15/4), the fraction is just 1%. The upper limit of the well width is roughly 30 ML, above which the confinement of LOP may not be appreciable.² If the wells were narrower than 10 ML, the electronic subband levels would rise above the barriers causing the carriers to be deconfined by the MQW, as shown by computer simulations that solve the Schrödinger and Poisson equations self-consistently.

2.4 Data and Discussions

The sample's Hall mobility and carrier sheet density were measured by the van der Pauw method. The magnetic field was 2 kiloGauss. The samples were exposed only to diffused ambient light shortly before the measurements. To minimize the contribution of the parallel conduction in the donor layer to the total mobility, the samples were etched with the solution $H_3PO_4:H_2O_2:H_2O = 3:1:50$ until their individual Hall mobility reached a maximum value.

The mobilities after etching and the carrier sheet densities are shown in Table 2.1. The REF's mobility was $7590 \text{ cm}^2\text{V}^{-1}\text{s}^{-1}$ at room temperature, comparable to the value of REF+4, taking into account its lower carrier sheet density. The MQW samples, however, all showed lower room temperature mobilities than the control samples. Among them, the MQW(15/x) samples had the highest mobilities. At $T = 77\text{K}$, the mobility

of the MQW samples approached that of the control samples, except for the MQW(20x) samples

Table 2.1. The Hall mobility and carrier sheet density of the samples at room and liquid nitrogen temperature. The control sample REF has the basic MODFET structure; REF+4 has an additional 4 ML thick AlAs between the AlGaAs spacer and the GaAs channel. The samples MQW(x/y) have x ML of GaAs as well and y ML of AlAs as barriers.

	T=300K μ [cm ² V ⁻¹ s ⁻¹]	N _S [10 ¹¹ cm ⁻²]	T=77K μ [10 ³ cm ² V ⁻¹ s ¹]	N _S [10 ¹¹ cm ⁻²]
REF	7590	5.44	189	5.52
REF+4	8200	4.12	193	4.15
MQW(12/2)	5287	2.94	191	1.80
MQW(12/4)	5189	2.00	180	1.48
MQW(15/2)	6318	3.16	198	2.20
MQW(15/4)	6682	2.49	181	2.66
MQW(20/2)	6024	3.72	124	2.48
MQW(20/4)	5055	3.31	153	1.90

The true mobility of the GaAs channel (and its MQW) is given by the Petriz model:⁶

$$\mu_{\text{channel}} = \frac{1}{2} \mu_{\text{AlGaAs}} \left(1 + \sqrt{1 - 4\mu N \frac{(\mu_{\text{AlGaAs}} - \mu)}{\mu_{\text{AlGaAs}}^2 N_{\text{channel}}}} \right)$$

where μ and M are the effective mobility and carrier sheet density at $T = 300\text{K}$, respectively; N_{channel} is the sheet density measured at $T \leq 50\text{K}$; μ_{channel} and N_{channel} are the true mobility and sheet density at $T = 300\text{K}$, respectively. μ_{AlGaAs} is the mobility of the free electrons inside the donor layer at 300K ; its value is conventionally taken to be 500 to $1000 \text{ cm}^2\text{V}^{-1}\text{s}^{-1}$. Thus $\mu_{\text{channel}} \approx 9600 \text{ cm}^2\text{V}^{-1}\text{s}^{-1}$ and $8700 \text{ cm}^2\text{V}^{-1}\text{s}^{-1}$ for the REF and MQW (15/x) samples, respectively.

The lower mobility of the MQW samples is readily understood by the hybrid model of phonons in superlattice structures. This model is presented in a paper submitted elsewhere.⁷ In the case of the AlAs/GaAs MQW structure, the LOP-like hybrid modes of the AlAs barriers are not coupled to the interface polaritons (IP). The latter thus interact strongly with the electrons in the well region. Although the interaction of electrons and LOP is reduced in the MQW samples, the increasing strength of the electrons-barrier IP scattering enhances the overall scattering rate as the well width decreases, and hence reduces the mobility. The channel mobility calculated by this model was $6120 \text{ cm}^2\text{V}^{-1}\text{s}^{-1}$ for an infinite MQW with 15 ML thick GaAs wells and 2 ML thick AlAs barriers, compared to

the actual value of $8700 \text{ cm}^2 \text{V}^{-1} \text{s}^{-1}$ of the (short periodic) MQW(15/2) sample.

The dependence of the Hall mobility and carrier sheet density on temperature was also investigated. To minimize the persistent photoconductivity effect, the samples were kept in the dark for at least 10 hours before being measured in a continuous flow cryostat fed by liquid helium. The results for the REF, MQW(15/2) and MQW(15/4) are shown in Fig. 2.3. One observes that the mobility of the MQW samples raised above that of the REF at $T \leq 50\text{K}$. The MQW(15/2)'s mobility was $1.4 \times 10^6 \text{ cm}^2 \text{ V}^{-1} \text{ s}^{-1}$, twice as high as the REF's ($6.9 \times 10^5 \text{ cm}^2 \text{V}^{-1} \text{s}^{-1}$) at $T = 11\text{K}$. The sheet desntiy of the MQW samples were considerably lower than that of the REF because they were etched, as mentioned above.

The improved mobility of the MQW samples indicates that the electron-IP interaction is no longer the dominant scattering mechanism at low temperatures. Our low temperature simulations showed a smaller field across the spacer layer in the MQW samples than in the REF, which reduced the effect of remote ionized impurity scattering. More important, the improved mobility shows that the interface roughness scattering is not a factor in lowering the MQW sample's mobility at room temperature.

2.5 Conclusions

We have tested several short periodic MQW structures for the enhancement of their room temperature mobility due to the suppression of electron-LOP scattering. The results were interpreted as negative. The best room temperature mobility was achieved by the MQW with 15 ML thick GaAs wells and 2 or 4 ML thick barriers. It was roughly 10% lower than that of the samples without the MQW. This result was readily explained by the strong interaction of the well electrons with the IP-like

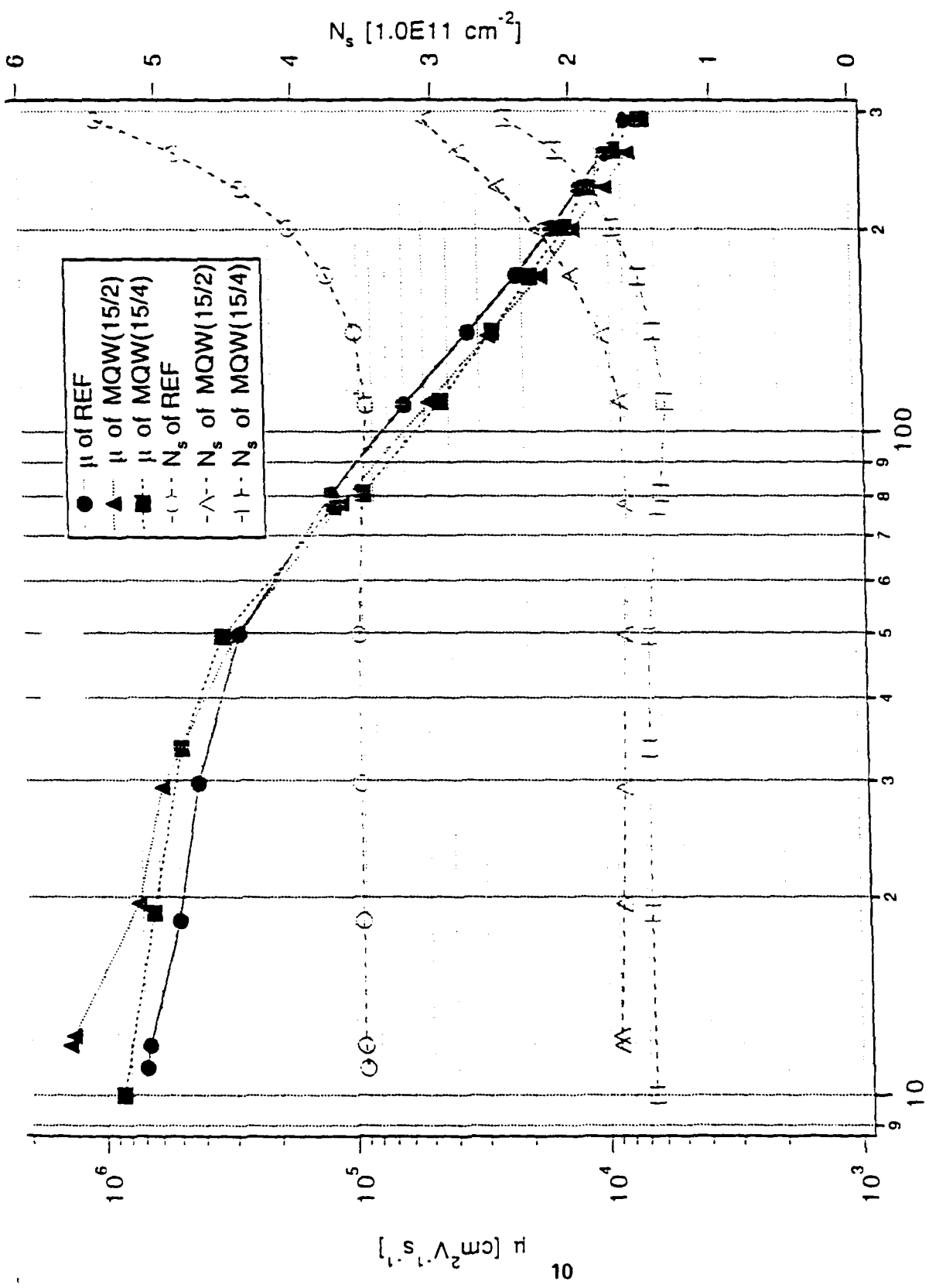


Figure 2.3. The mobility μ and carrier sheet density N_s of the REF, MQW(15/4) and MQW(15/2) as functions of temperature. μ of REF is higher than the other two at room temperature, but decreases relatively at $T \leq 50\text{K}$. The sheet densities of the MQW samples are lower than that of REF because the latter were etched.

hybrid modes from the AlAs barriers. At low temperatures, the MQW samples' mobility was higher than that of the control samples, due to reduced remote ionized impurity scattering.

To the best of our knowledge, the enhancement of room temperature mobility by suppression of electron-LOP scattering has yet to be experimentally proven. The results of Zhu et.al.⁸ that appeared to confirm the opposite may actually be explained using some alternative arguments. The energy band structure and the bulk carrier density of the samples are shown in Fig. 2.4. The MQW's wall and barrier thickness are 8 ML and 4ML, respectively. These narrow wells raise the electron subbands over the barriers, spilling most of the electrons onto the AlAs/GaAs-substrate interface, which is both smooth he ionized donors. The major contribution to the total mobility is from the 2DEG at this interface, not from the electrons in the MQW structure. In case of the control sample, the electrons stay inside the GaAs well and are subjected to more interface roughness and ionized impurity scattering, as compared to the majority of the electrons in the MQW sample; hence the mobility is considerably lower. Please not that both of these samples have lower room temperature mobility than bulk GaAs.

2.6 References

1. F. A. Riddoch and B.K. Ridley, J. Phys. C: Solid State Phys. 16, 6971 (1983).
2. N. Sawaki, J. Phys. C: Solid State Phys., 19, 4965 (1986).
3. K.W. Kim, A.R. Bhatt, M.A. Stroscio, P.J. Turley and S.W. Teitsworth, Appl. Phys. Lett., 72 2282 (1991).
4. B.K. Ridley, Phys. Rev. B 47, 4592 (1993).
5. M.A. Stroscio, G.J. Iafrate, K.W. Kim, M.A. Littlejohn, H. Goronkin, G.N. Maracas, Appl. Phys. lett. 59, 1093 (1991).
6. R.L. Petritz, Phys. Rev. 110, 1254 (1958).

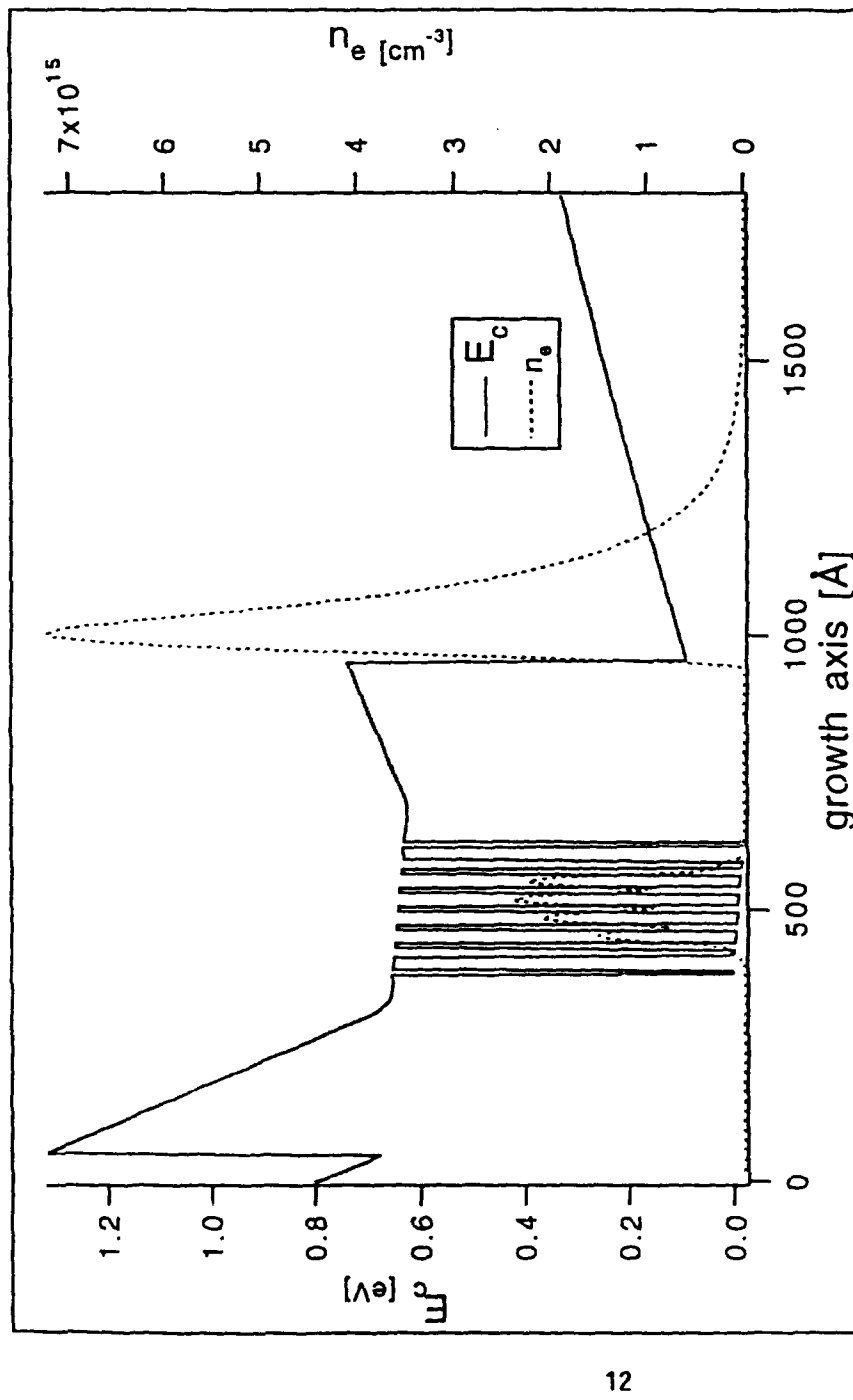


Figure 2.4. A different design of MQW structures, as of Zhu et.al. (a) shows the control sample with its GaAs well at the center, where the free electrons are concentrated. The sharp gap on the right is the AlAs/GaAs-substrate interface.

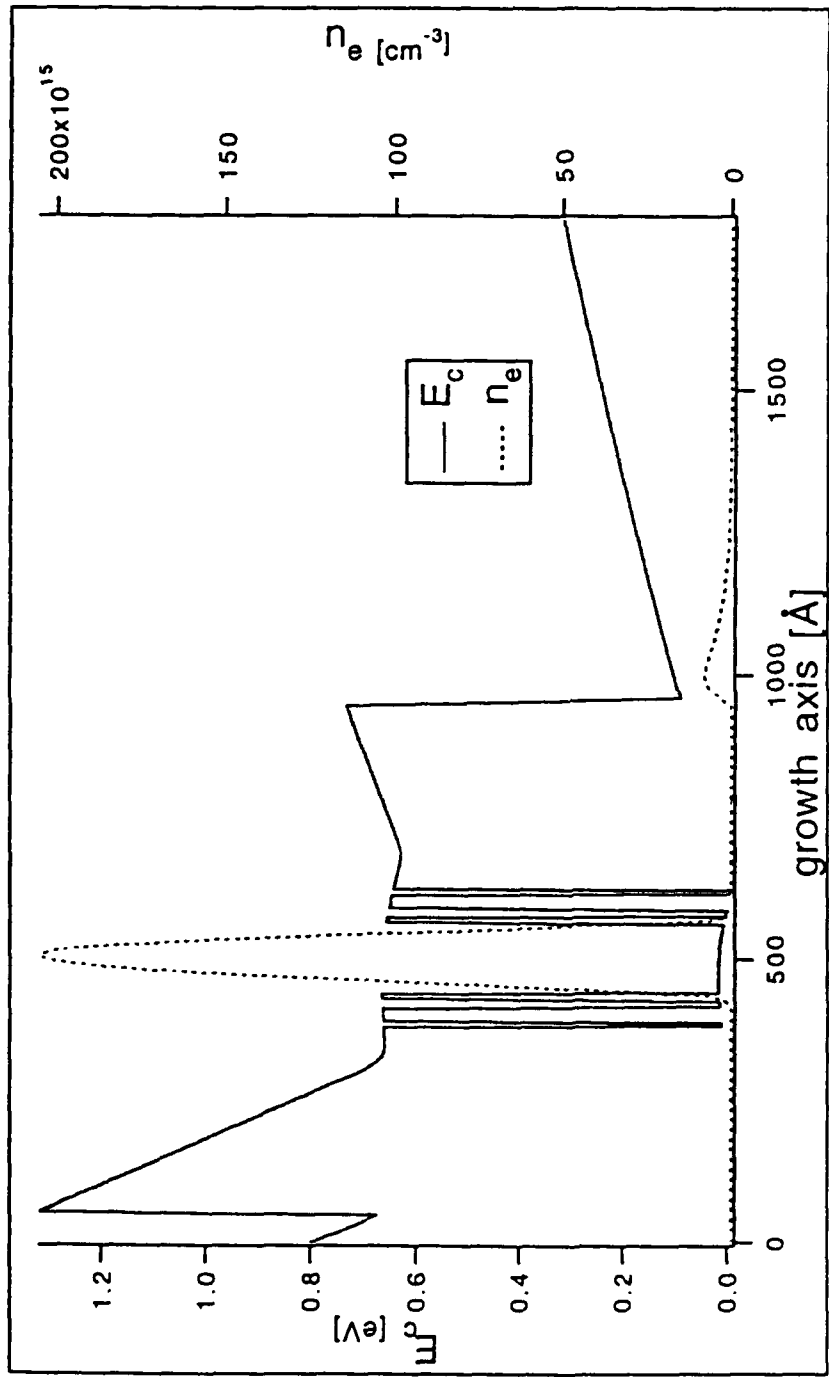


Figure 2.4. A different design of MQW structures, as of Zhu et.al. (b) shows the MQW structure. The MQW with well width = 8 ML and barrier width = 4 ML is grown onto the GaAs. Since the wells are small, the free electrons are spilled into the smooth AlAs/GaAs-substrate interface.

- 7.T.T. LeTran, W.J. Schaff, B.K. Ridley, Y.P. Chen, A. Clark, S. O'Keefe, and L.F. Eastman, submitted to *J. Appl. Phys.* (1993).
8. X.T. Zhu, H. Goronkin, G.N. Maracas, R. Droopad, M.A. Stroscio, *Appl. Phys. Lett.* **60**, 2141 (1992).

III. Optical Mode Hybrids in Quantum Wells, Superlattices and Slabs - B.K. Ridley

3.1 Abstract

The presence of interfaces causes the hybridization of LO and TO modes in non-polar material and of LO, TO and interface polaritons (IP) in polar material. Hybridization arises as a consequence of the necessity to satisfy simultaneously electromagnetic and mechanical boundary conditions. Optical mode analogues of surface Rayleigh waves appear in non-polar slabs, and in polar superlattices the involvement of interface polaritons causes significant dispersion and anisotropy. Results from a continuum theory are shown to describe experimental results reasonably well. Hybridization affects the quantum properties due to the coherent mixing of LO, TO and IP, and this, in turn, affects the interaction with electrons. Estimates of the electron-hybridon scattering rate in GaAs quantum wells are presented.

3.2 Introduction

The advent of layered semiconductor structures has generated the need for a simple analytical description of the way in which confinement of electrons and phonons affects their interaction. While effective-mass theory has been found to be adequate for electron confinement, obtaining an equivalent theory for optical phonons has been more problematic, particularly in polar material. The main difficulties have been to do with boundary conditions and the nature of the basic interaction of confined

modes with electrons. Recently, continuum models of confined optical modes which overcome these difficulties to varying degrees have begun to emerge [1-3], and to show agreement with Raman scattering data [4]. A subject of recent discussion [5,6] has been the nature of the electron-polariton interaction - whether it is via a vector or a scalar potential - and this has now been resolved [7]. An outline of a continuum model for confined optical vibrations is presented here, along with some of the results generated by it.

Section 3.3 reviews the basic equations which describe bulk waves in an elastically isotropic continuum, Section 3.4 discusses the boundary conditions which forces the mixing of optical modes and Section 3.5 describes the form of the hybrid modes produced. The interaction of these hybrid modes with electrons is discussed in Section 3.6. Some results of the theory are presented in Section 3.7 and the dispersion predicted in an AlAs/GaAs superlattice is compared with experiment. It is also shown that hybrid modes can have either LO-like or IP (interface polariton)-like properties, and the strength of interaction with electrons can be highly anisotropic. The paper concludes with a brief discussion in Section 3.8 of some of the problems.

3.3 Continuum Optical Modes

For simplicity, the medium supporting optical vibrations is considered to be an isotropic elastic continuum in which long-wavelength modes obey an equation of motion of the form:

$$\rho \frac{\partial^2 \mathbf{u}}{\partial t^2} = -\rho \omega_{TO}^2 \mathbf{u} + e_i \mathbf{E} - c_{11} \nabla (\nabla \cdot \mathbf{u}) + c_{44} \nabla \times \nabla \times \mathbf{u} \quad (1)$$

where \mathbf{u} is the relative displacement of the ions, ρ is the reduced density, ω_{TO} is the natural frequency of vibration, e_i is the effective ionic charge density (zero for non-polar material), \mathbf{E} is the macroscopic electric field, and c_{11}, c_{44} are optical-mode elastic constants which quantify the stress in the medium and, associated with it, the dispersion relation. In the absence of free charge the electric field must satisfy

$$\nabla \cdot \epsilon(\omega) \mathbf{E} = 0 \quad (2)$$

and any transverse part of the field will obey the electromagnetic wave equation:

$$\frac{\partial^2 \mathbf{E}_T}{\partial t^2} = \frac{1}{\mu_0 \epsilon(\omega)} \nabla^2 \mathbf{E}_T \quad (3)$$

where $\epsilon(\omega)$ is the permittivity (in general, frequency dependent) and μ_0 is the permeability of free space in the case, as assumed here, of non-magnetic material. The ionic displacement can be factorized into longitudinal and transverse parts:

$$\mathbf{u} = \mathbf{u}_L + \mathbf{u}_T, \quad \nabla \times \mathbf{u}_L = 0, \quad \nabla \cdot \mathbf{u}_T = 0, \quad (4)$$

and travelling-wave solutions for longitudinal optical (LO), transverse optical (TO) and polaritons (P) emerge, with the properties:

$$LO \quad \omega^2 = \omega_{LO}^2 - v_L^2 k^2, \quad \epsilon(\omega) = 0, \quad \mathbf{E}_L = -\frac{e_i}{\epsilon_\infty} \mathbf{u}_L = -\left[\rho(\omega_{LO}^2 - \omega_{TO}^2)\right]^{1/2} \mathbf{u}_L$$

(a)

$$TO \quad \omega^2 = \omega_{TO}^2 - v_T^2 k^2, \quad \epsilon(\omega) = \infty, \quad \mathbf{E}_T = 0, \quad (b) (5)$$

$$P \quad \omega^2 = \frac{k^2}{\mu_0 \epsilon(\omega)}, \quad \epsilon(\omega) = \epsilon_\infty \frac{(\omega_{LO}^2 - \omega^2)}{(\omega_{TO}^2 - \omega^2)}, \quad \mathbf{E}_T = s \mathbf{E}_L, \quad (c)$$

where $\omega_{LO}^2 = \omega_{TO}^2$. ($\epsilon_s / \epsilon_\infty$). ϵ_s and ϵ_∞ are the zero- and high-frequency permittivities, $v_L^2 = c_{11} / \rho$, $v_T^2 = c_{44} / \rho$, and $s = (\omega^2 - \omega_{TO}^2) / (\omega_{LO}^2 - \omega_{TO}^2)$.

These three types of mode provide the basis of a continuum model of confinement.

3.4 Boundary Conditions

At each interface both electromagnetic and mechanical connection rules must be satisfied. (Fundamentally, there are only electromagnetic conditions, but it is convenient to distinguish short range elements by the label "mechanical".) The EM conditions are the standard ones, i.e., continuity of tangential field and of perpendicular electric displacement. The mechanical conditions are less obvious. For acoustic waves these conditions would amount to entailing the continuity of displacement and of stress for equilibrium to be maintained. Macroscopic stress must enter the conditions for optical modes, but since the latter involve internal motion within a primitive unit cell, the situation is more complicated, as has been demonstrated using a linear chain model [8]. However, in linear chain models the interface is assumed to be located with precision, but its precise

location affects the transfer matrix, and so in reality some averaging is necessary, and this reduces the importance of microscopic stresses. Thus taking a boundary condition based upon macroscopic stress only is likely to be reasonably realistic. The mechanical connection rule is therefore taken to be the continuity of macroscopic stress and displacement, in an "acoustic" approximation.

The situation here is not unlike that for electrons. The wavefunction for electrons is a Bloch function consisting of a microscopic part describing the charge in each unit cell and an envelope function. Strictly, both parts must be considered in ensuring continuity of current at a boundary, but it is often a good approximation to restrict the matching procedure to the envelope function only. Our "acoustic approximation" is a somewhat analogous procedure which throws all the emphasis on the macroscopic property.

3.5. Hybrid Optical Modes

In order to satisfy these boundary conditions for p-polarized modes (i.e., modes with polarization in the plane of incidence) it is necessary to take a linear combination of the bulk solutions having identical frequencies and identical in-plane wavevector. (For the s-polarized TO mode this procedure is unnecessary. It is only with p-polarized modes that problems exist.) In a single layer $-a/2 \leq z \leq a/2$ with the x-axis parallel to the direction of propagation, the resultant p-polarized hybrids have relative ionic displacements of the form:

$$u_x = k_x A [\cos k_L z + c_T \cos k_T z - c_p \cos k_p z] e^{i(k_x x - \omega t)} \quad (6)$$

$$u_z = ik_L A \left[\sin k_L z - c_T \frac{k_x^2}{k_L k_T} \sin k_T z + c_p \frac{k_x}{k_L k_p} \sin k_p z \right] e^{i(k_x x - \omega t)}$$

where the subscripts L, T and P refer respectively to the LO, TO and P components. A second form with sine replacing cosine also exists. In the surrounding material $|z| > a/2$, the solutions in most cases consist of components which exponentially decay away from the layer. For given frequency and in-plane wave vector the wavevector k_L , k_T and k_p are all determined. The boundary conditions select the allowed frequencies and quantify the fractional amplitudes c_T and c_p . Standard quantization procedure determines the amplitude A, and expresses u in terms of annihilation and creation operators. (Strictly, hybrids of the same parity should be subjected to a rigorous orthogonalization procedure but in many cases of interest the departure from orthogonality is small and can be neglected. Of course, opposite parity modes are always orthogonal). In non-polar material, $c_p = 0$. In polar material at in-plane wavevectors of order 10^6 cm^{-1} , typically involved in the interaction with electrons, the unretarded limit can be taken for the polariton, which then turns out to be an interface mode with $k_p \approx -ik_x$. At frequencies above ω_{TO} in polar material the TO component is also an interface mode with $k_T = -i\alpha_T$. For frequencies significantly above ω_{TO} , α_T is typically so large that its precise magnitude cannot be predicted accurately by a long-wavelength model with quadratic dispersion, and it is then necessary to obtain it from the complex vibrational band structure predicted by lattice dynamics.

3.6 Interaction with Electrons

Discussion here will be limited to the polar interaction. The latter is

affected by hybridization in several ways. First, the Fröhlich interaction with LO modes is reduced by confinement (which puts a lower limit on the total wavevector) a reduction which increases with decreasing well-width. Second, the interaction with IP (interface polariton) modes is also modified by confinement in some cases through the coherent association with the LO component. When this occurs this interaction also diminishes with decreasing well-width. However, for strongly polar materials in which the LO and TO bands do not overlap (e.g., AlAs) there exist frequencies for which the LO component must be replaced by a mode drawn from the LO/LA branch of the complex vibrational band structure. In this case the IP mode would act approximately as an unhybridized mode, and its interaction with electrons would then increase with diminishing well-width. (Such a behaviour is predicted in the case of AlAs/GaAs from lattice dynamics [[9]]). It turns out that in the case of a slab with stress-free surfaces, hybridization is weak, and the IP mode is expected to interact with electrons approximately in the familiar unhybridized way. But for cases where the mechanical mismatch effectively reduces the relative ionic displacement to zero at the interface, and where LO/IP hybridization can take place strongly, the polar interaction with well modes will under some circumstances diminish in strength with diminishing well-width. Finally, the polar interaction will be affected by the more complex dispersion which occurs as a result of LO/IP hybridization. This is particularly the case in superlattices, where the dispersion becomes highly anisotropic, and consequently, so does the interaction with electrons.

The interaction of interface polaritons with electrons takes place (in the usual Coulomb gauge) via a vector potential \mathbf{A} - specifically as $-e \mathbf{A} \cdot \mathbf{p}/m^*$, where \mathbf{p} is the momentum operator and m^* is the effective mass of

the electron. Polaritons, being transverse EM modes, do not have a scalar potential ϕ , and so the IP interaction is not like that for LO modes. However, in many cases it has been assumed without proof that in the unretarded limit it is permissible to calculate the interaction as if the IP mode had a scalar potential associated with it. This matter has been clarified recently [7]. In the unretarded limit for interface polaritons it is possible to associate a potential Λ with the mode such that $\mathbf{A} = -\hbar \nabla \Lambda / e$. A unitary transformation generated by the operator $U = \exp(-i\Lambda)$ then converts the Hamiltonian, to first order, into one which contains an operator which behaves like a scalar potential ϕ plus a self-energy term. For real transitions involving matrix elements on the energy shell the use of $e\phi$ gives exactly the same results as $e \mathbf{A} \cdot \mathbf{p}/m^*$, but for virtual and higher order transitions this would not be true. Thus, either \mathbf{A} or ϕ can be used in the unretarded limit provided only scattering rates are required.

The interaction with holes involves the deformation potential associated with all three components of the hybrid, and this will be true also for electrons in L-valleys. While deformation potential scattering by LO and TO modes is familiar enough, that by interface polaritons is novel.

3.7. Results

The theory has been applied to the cases of a slab with stress-free surfaces, and to a quantum well and a superlattice with rigid interfaces. In the case of the non-polar slab the theory mixes LO and TO guided waves and predicts the existence of a surface wave which is the optical mode analogue of the Rayleigh wave [10]. In the case of a polar slab, hybridization turns out to be weak [11] and the modes can be described to a good approximation purely by taking EM boundary conditions, as was done by Fuchs and Kliewer long ago [12].

In the case of a polar quantum well with $u = 0$ at the interfaces, hybridization is strong at all frequencies provided, there is no LO/TO gap at the zone boundary[3]. Such is the case with GaAs, and Fig. 3.1 shows the dispersion, with the influence of the IP mode evident in producing anti-crossings and mode conversions. In particular, the LO1 mode with $k_L = \pi/a$ converts to an LO3-like mode with $k_L = 2.86 \pi/a$, while the LO3 moves toward LO5. Fig. 3.2 shows the intrasubband scattering rates at threshold in an infinitely deep quantum well associated with LO-like hybrids. Although the IP component of the hybrid enhances the interaction significantly from the bare LO contribution it gets weaker with narrowing wells.

Approximately pure IP modes exist at and around special points in the dispersion. These points are where the IP dispersion crosses the dispersion of an LO mode of symmetry *opposite* to that of the IP, and are thus identified by special pairings of k_L, k_x . These IP-like hybrids will interact with electrons somewhat differently from the interaction associated with LO-like hybrids. Being limited to small regions of k_L, k_x space they will not be as generally available as LO-like modes for scattering purposes and so their contribution to the overall scattering rate is expected to depend more sensitively on the specific structure. This adds to the difficulty of estimating scattering rate in the presence of hybridization.

The superlattice dispersion of GaAs hybrids when $\tanh \alpha_T a \approx 1$ is given by

$$\begin{aligned} & \sin k_L a (2rs^2d + (k_x^2/k_L^2) \sinh k_x a \sinh k_x b) + 2s(k_x/k_L) \\ & [\sinh k_x b + rsinh k_x a \cos k_x (a+b) - \cos k_L a (\cosh k_x a \sinh k_x b + rsinh k_x a \cosh k_x b)] = 0 \end{aligned} \quad (7)$$

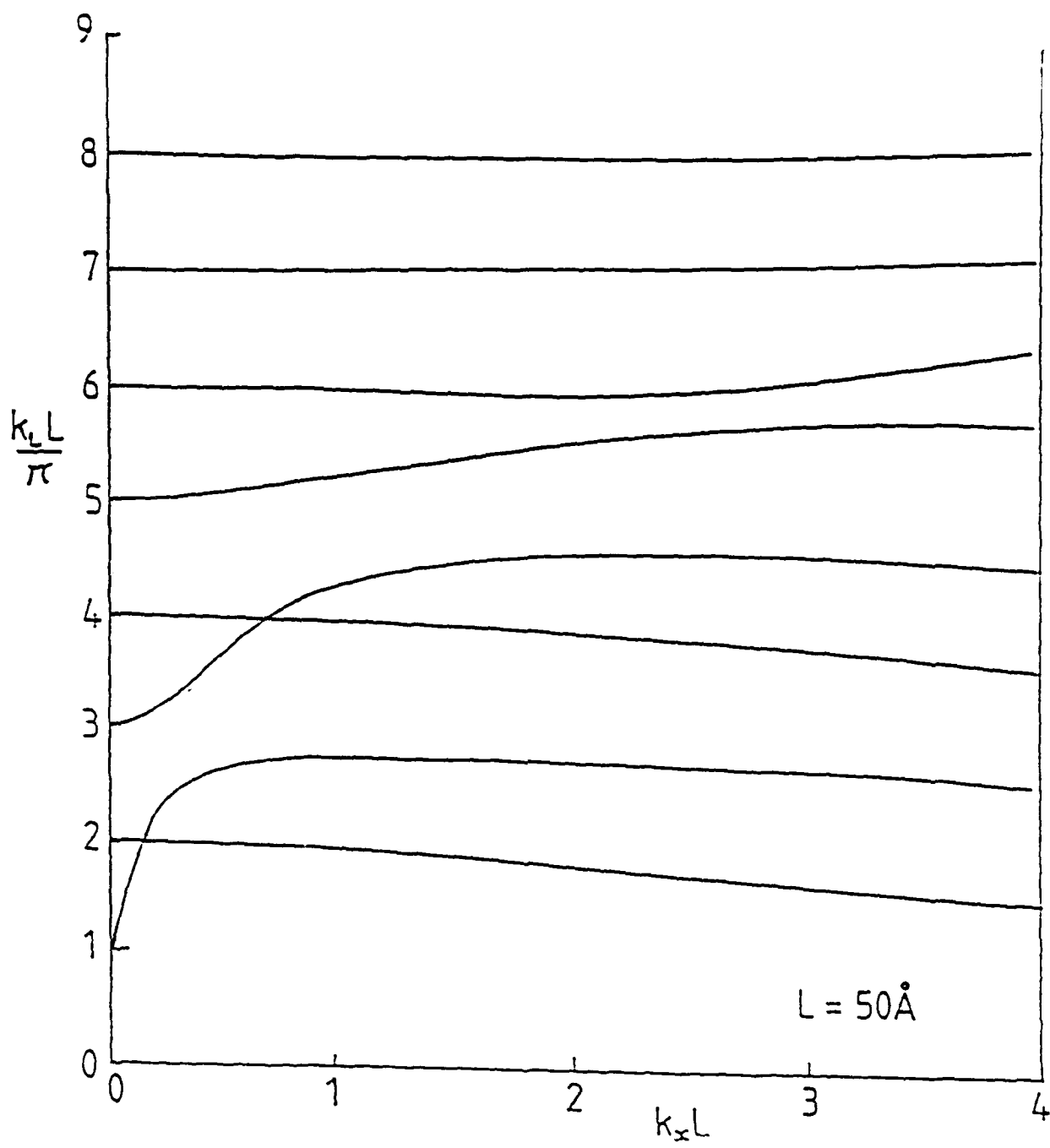


Figure 31. Dispersion of hybrid optical modes in a 50 \AA GaAs quantum well.

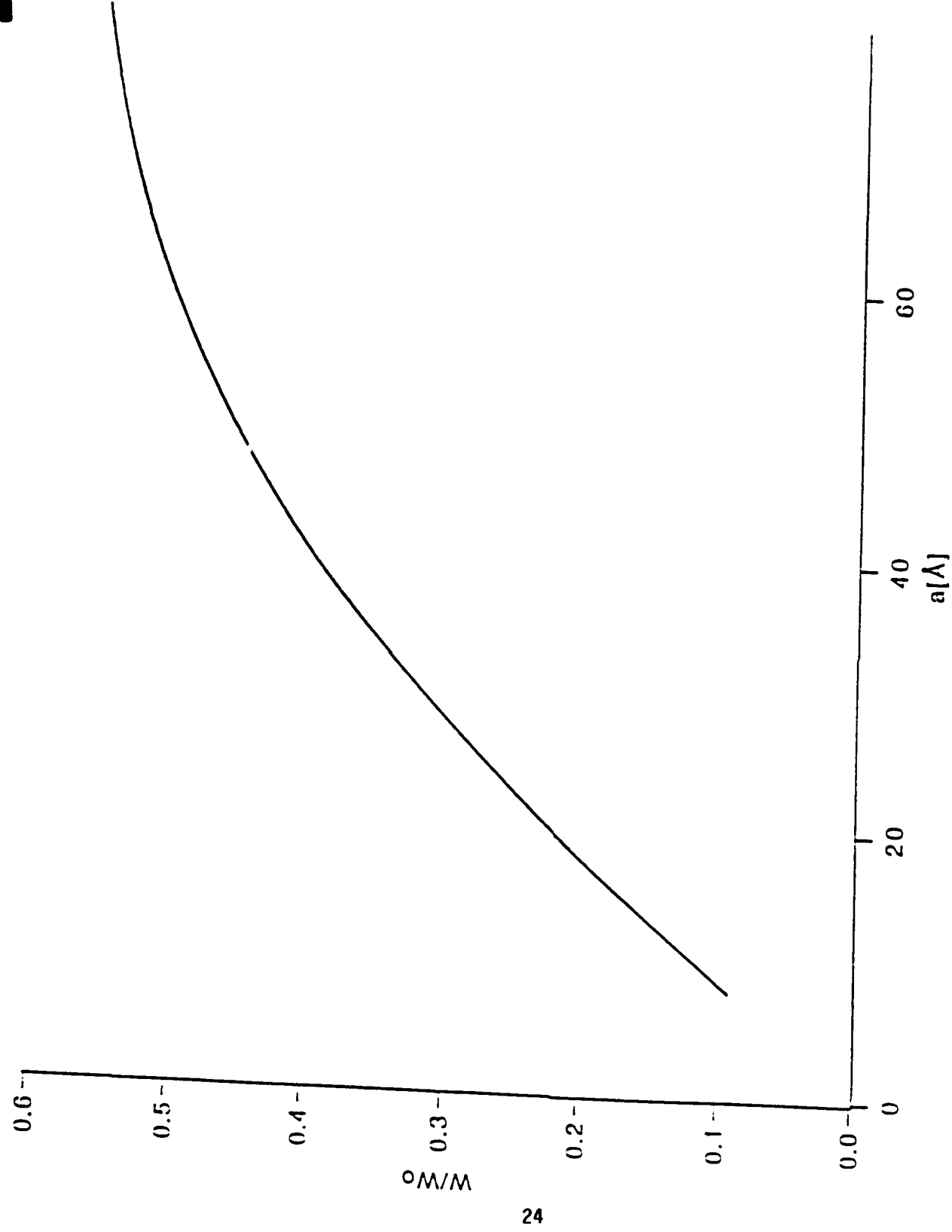


Figure 3.2. Intrasubband scattering rates at threshold for LO-like modes in a GaAs infinitely deep quantum well.

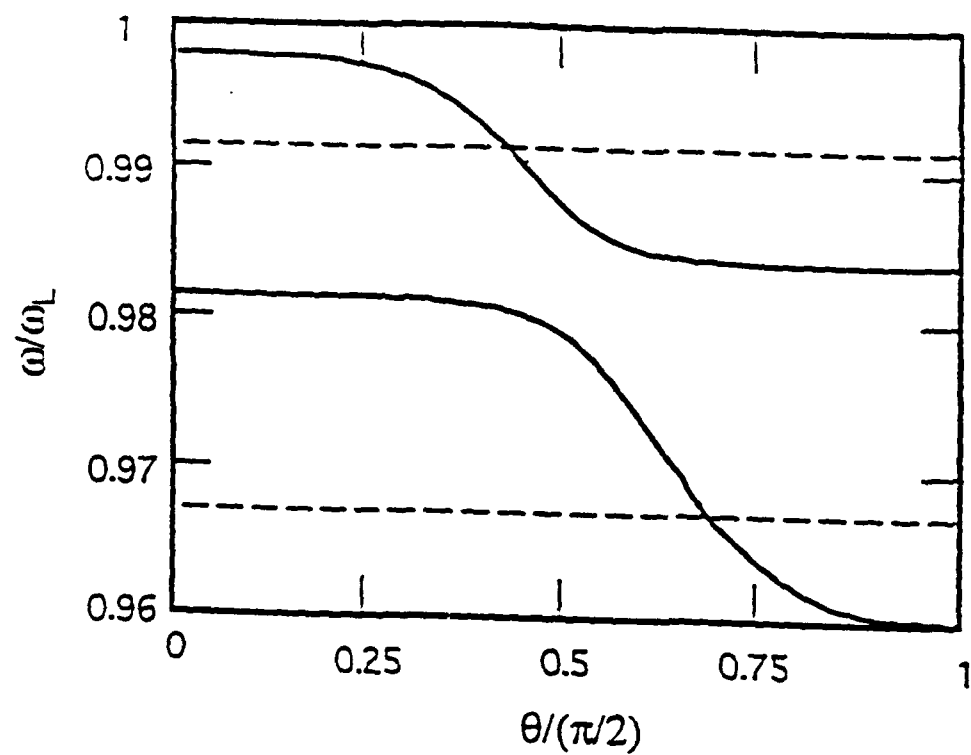


Figure 3.3. Dispersion of a 12/12 monolayer GaAs/AlAs superlattice as a function of angle θ where $\tan \theta = k_x/k_z$.

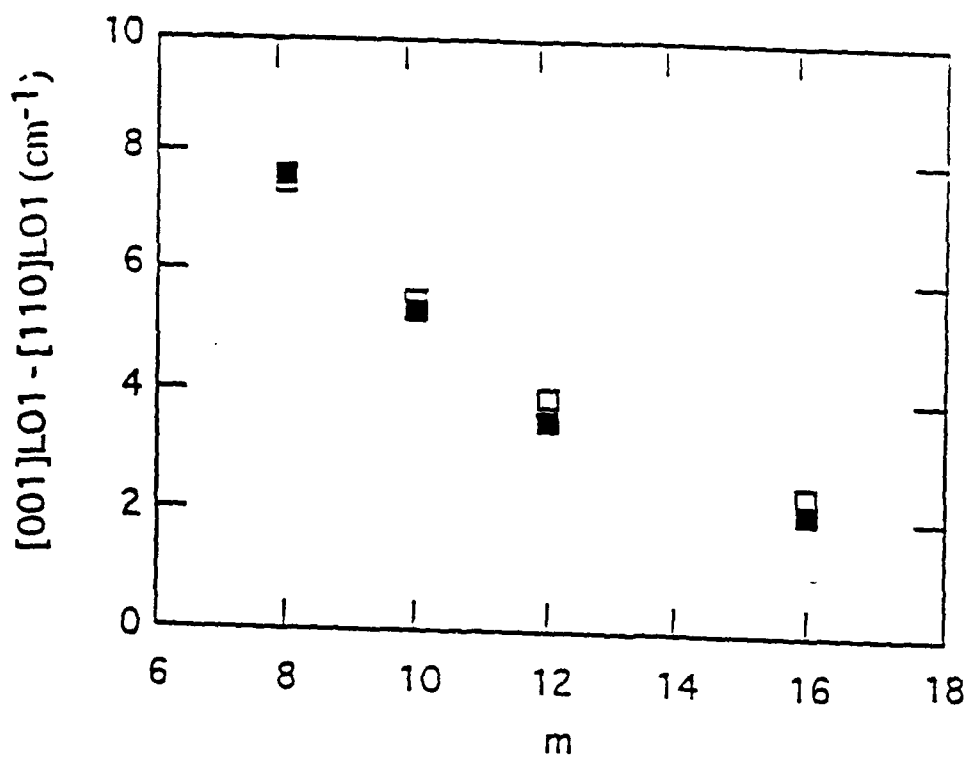


Figure 3.4. The change of frequency of the LO1 mode from on-axis to in-plane propagation as a function of m the number of monolayers in a m/m GaAs/AlAs superlattice. Open squares: theory; closed squares experiment [4].

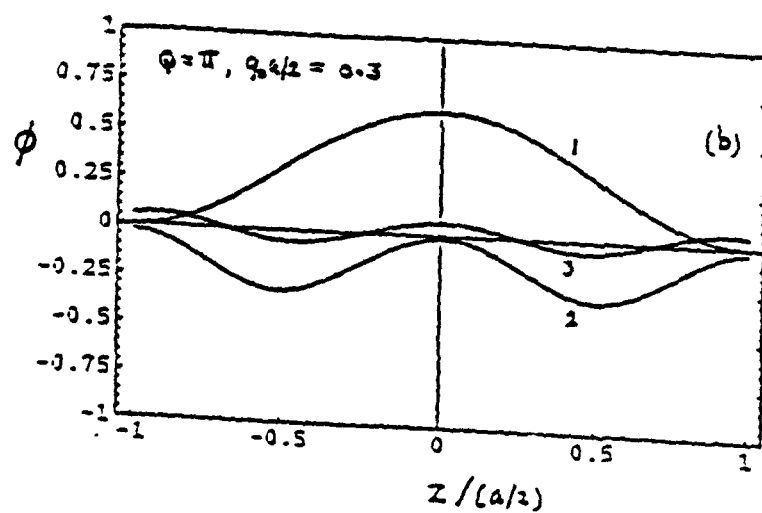
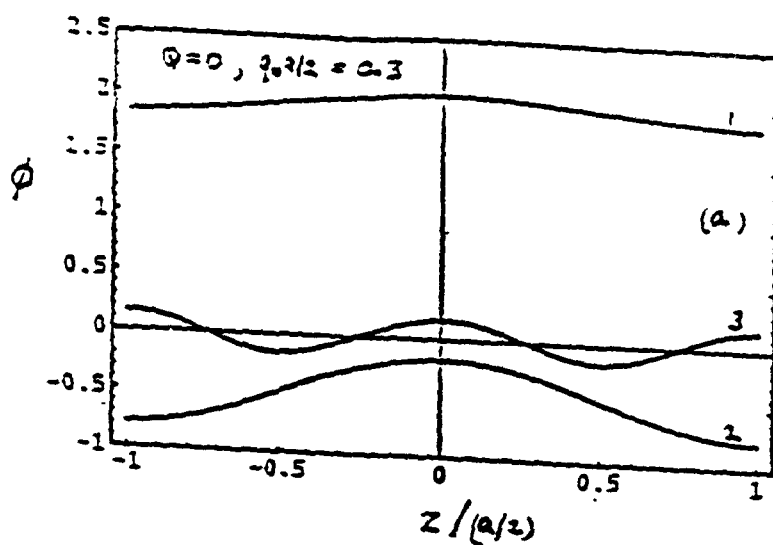


Figure 3.5. Patterns of potential for the first three symmetric modes in a GaAs quantum well of a model GaAs/AlAs superlattice. The barrier width is 5.66\AA and the in-plane wavevector equals that at the threshold of emission ($2.52 \times 10^6\text{cm}^{-1}$). (a) $Q \equiv k_z(a+b0) = 0$; (b) $Q = \tau$.

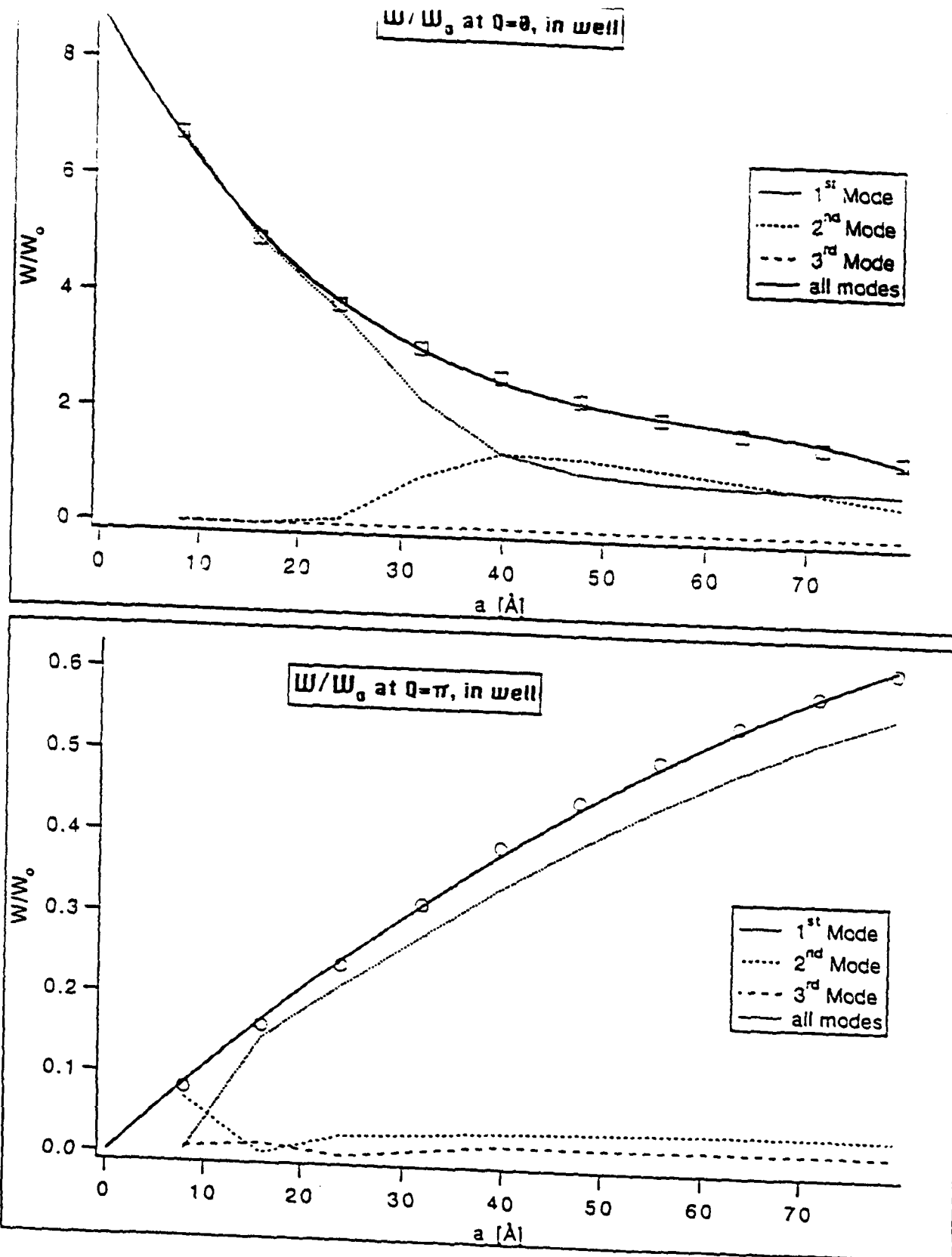


Figure 3.6. Intrasubband scattering rates at threshold for GaAs modes in the model GaAs/AlAs superlattice with $b = 5.66\text{ \AA}$; contributions of the first three symmetrical modes are shown. (a) $Q = 0$; (b) $Q = \pi$.

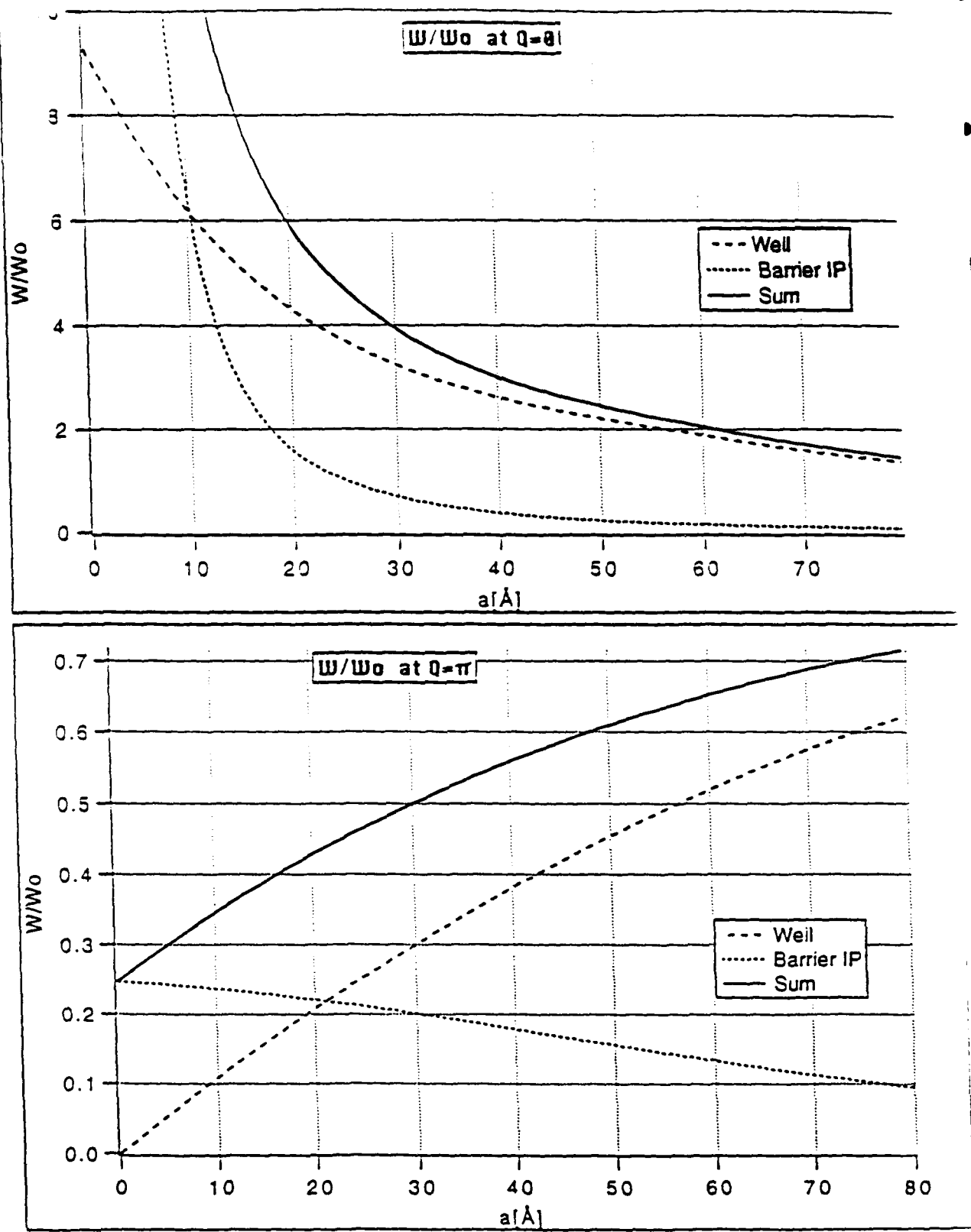


Figure 3.7. Intrasubband scattering rates at threshold for well and barrier modes for the same system as Figs. 5 and 6: (a) $Q = 0$; (b) $Q = \pi$. Note that the sum ignores the difference in threshold energy of well and barrier modes.

3.8 Conclusions

In spite of the above agreement with experiment, it is too early to be entirely confident that a continuum approach to the problem of optical vibrations in layered material is generally adequate. Indeed, we have already seen that in some circumstances modes are called for whose amplitudes vary significantly over a distance of order of the unit cell dimension. Such components of a hybrid cannot be described adequately without help from lattice dynamics. Experimental data is still sparse for layered material in which the elastic boundary condition is not as simple as $u = 0$, such as, for example, $Al_xGa_{1-x}As/GaAs$ with $x \sim 0.3$, though this system introduces the added complication of a two-mode spectrum. For the polar slab with stress-free surfaces hybridization turns out to be too weak for the approach to be distinguishable from a conventional dielectric continuum model. Which is support of a kind, since there is a lot of experimental evidence for the latter model in this particular case. A prediction for the non-polar slab is the existence of optical Rayleigh waves, and this should be amenable to experimental test.

The importance of a continuum model resides in its usefulness for transport theory. Its predictions concerning the scattering of electrons in real systems have still to be worked out. Unfortunately the paradigmatic system, $AlAs/GaAs$, contains the problem of describing dispersion in $AlAs$, which is small. How small determines the degree of LO/IP hybridization and this, in turn, crucially determines the strength of fringing fields in the $GaAs$ which can scatter electrons. Hitherto, it has been assumed that no LO/IP hybridization occurs in $AlAs$ [15], but this assumption needs examination. It leads to the conclusion that scattering in narrow wells is dominated by the unhybridized $AlAs$ IP mode, and there is experimental

support for this [16]. Nevertheless, the whole question of hybridization in materials with zone-edge gaps in the optical mode spectrum needs to be investigated.

The results of the scattering rate in a superlattice with narrow opaque barriers presented here shows that IP-like hybrids belonging to the well make a significant contribution. Although hybridization produces highly modified properties it is still possible to identify LO-like and IP-like hybrids, which are responsible for highly anisotropic scattering rates.

Finally, it should be recalled that the deformation potential interaction with holes or with L-valley electrons will involve the interface polariton component of a hybrid as well as the LO and TO parts. A comprehensive description of the interaction of hybrid optical modes with holes does not yet exist, but is certainly needed.

3.9 References

- [1] X. Zianni, P.N. Butcher and I. Dharssi *J. Phys. Condens. Matt.* **4** L77 (1992).
- [2] K.J. Nash *Phys. Rev.* **B46** 7723 (1992).
- [3] B.K. Ridley *Proc. SPIE Symp. on 'Compound Semiconductor Physics and Devices - High Speed Electronics and Optoelectronics'*, Somerset, NJ **1675** 492 (March 1992).
Phys. Rev. **B47** 4592 (1993).
- [4] M. Haines and G. Scamarcio *NATO ARW "Phonons in Nanostructures"* St. Filiu, Spain, (1992).
- [5] M. Babiker and B.K. Ridley **B43** 9096 (1991); **B15** (1993) (reply to comment by Knipp and Reinecke).
- [6] P.A. Knipp and T.L. Reinecke *Phys. Rev.* **B15** (1993) (comment on above paper).
- [7] M. Babiker, N.C. Constantinou and B.K. Ridley, submitted for publication
- [8] H. Akera and T. Ando *Phys. Rev.* **B40** 2914 (1989).
- [9] H. Rucker, E. Molinari and P. Lugli *Phys. Rev.* **B45** 6747 (1992).

- [10] B.K. Ridley Phys. Rev. B44 9002 (1991).
- [11] B.K. Ridley, O. Al-Dossary, N.C. Constantinou and M. Babiker
submitted for publication
- [12] R. Fuchs and K.L. Kliewer Phys. Rev. A140 2076 (1965).
- [13] N.C. Constantinou, O. Al-Dossary and B.K. Ridley Solid St. Commun
86 191 (1993).
- [14] T. Tsuchiya, H. Akera and T. Ando Phys. Rev. B39 6025 (1980).
- [15] O. Al-Dossary, M. Babiker and N.C. Constantinou Semicond. Sci.
Technol. 7 B91 (1992).
- [16] K.T. Tsen, K.R. Wald, T. Ruf, P.Y. Yu and H. Morkoc Phys Rev.
Lett. 67 2557 (1991).
- [17] K. Huang and B-F Zhu Phys. Rev. B38 13, 377 (1988).
- [18] B.K. Ridley Phys. Rev. B39 5282 (1989).

Double modulation-doped AlGaAs/InGaAs heterostructure with a graded composition in the quantum well

Tae-Kyung Yoo,^{a)} Pierre Mandeville, Hyunchang Park, William J. Schaff,
and Lester F. Eastman

School of Electrical Engineering and National Nanofabrication Facility, Cornell University, Ithaca,
New York 14853-5401

(Received 11 June 1992; accepted for publication 17 August 1992)

A new double modulation-doped AlGaAs/InGaAs heterostructure with a graded composition in the InGaAs quantum well (QW) has been designed and electrically characterized. An InGaAs QW with a rectangular-like potential profile in the presence of the two dimensional electron gas is obtained by a two-step grading of the In composition, which results in a broad and symmetric electron distribution profile even under various voltages. The Hall measurement shows a very high electron mobility of $7230 \text{ cm}^2/\text{V s}$ and an electron sheet density of $4.1 \times 10^{12}/\text{cm}^2$ at room temperature. To our knowledge, this is the highest mobility ever reported so far for the double modulation-doped $\text{Al}_{0.3}\text{Ga}_{0.7}\text{As}/\text{In}_{0.2}\text{Ga}_{0.8}\text{As}$ field-effect transistor structure.

Pseudomorphic AlGaAs/InGaAs/GaAs heterostructures have been extensively investigated in recent years to improve the performance of modulation-doped field effect transistors (MODFETs) as well as opto-electronic devices.¹ The InGaAs, when grown within a certain critical layer thickness (CLT) on GaAs, can provide a larger conduction band discontinuity at the AlGaAs/InGaAs interface than that of AlGaAs/GaAs, which leads to an increase in the electron sheet density in the quantum well (QW). The electron sheet density also increases with the In amount in the InGaAs QW, though the thickness of the well is limited by a CLT capable of accommodating a misfit-dislocation-free interface.² The increase of the electron sheet density (N_s) in the QW is crucial to the performance of MODFET's including the gain cutoff frequency for high-speed operation,³ noise figure in high frequency, low-noise operation,⁴ and current-driving capability for high-power operation.⁵ In order to increase N_s without increasing the In concentration, several MODFET structures, such as a double modulation-doped field effect transistor,⁶ a doped quantum well FET,⁷ and a double quantum well MODFET,⁸ were proposed. These approaches, however, often cause the degradation of the electron transport properties. The mobilities of the electron in the doped⁶ and doped quantum well structure⁸ were quite low because of the ionized impurity scattering in the QW in the former structure, and the interference of each QW with the donor supplying layer between the QWs in the latter case. In double modulation-doped structures, it is very difficult to obtain high mobility characteristics due to the surface roughness at the interface below the QW channel¹⁰ and the Si segregation effect.¹¹ Si atoms in the donor supplying layer below the QW move nonuniformly to the vicinity of, or even into, the QW during the molecular beam epitaxy (MBE) growth. Therefore, one of the most important concerns in MODFETs is to increase the N_s without sacrificing the electron mobility for practical high-frequency applications. In this letter, we describe a new design of double

modulation-doped heterostructure and characterize the electrical properties of the MBE-grown wafers.

A typical double modulation-doped field effect transistor (D-MODFET) structure is shown in Fig. 1. It consists of an $\text{In}_{0.2}\text{Ga}_{0.8}\text{As}$ QW, the In composition of which is uniform over the QW, two GaAs/ $\text{Al}_{0.3}\text{Ga}_{0.7}\text{As}$ spacers (A and B), and two $\text{Al}_{0.3}\text{Ga}_{0.7}\text{As}$ barriers including Si atomic planar doping (APD) layers. In particular, we put a 20 Å undoped GaAs layer between the $\text{Al}_{0.3}\text{Ga}_{0.7}\text{As}$ spacer and $\text{In}_{0.2}\text{Ga}_{0.8}\text{As}$ QW, which greatly helps reduce the surface roughness at heterointerfaces, especially with high Al (30%) and In (20%) concentrations, and also allows for the change in the growth temperature from 580 °C for AlGaAs to 500 °C for InGaAs.¹² The necessity of the 20 Å of the GaAs layer between the pseudomorphic InGaAs channel and AlGaAs spacer suggests that there may be serious interface roughness at the heterointerface, even though the theoretical room-temperature mobility is dominantly determined by the optical phonon scattering rather than the remote ionized-impurity, or interface roughness, scattering.¹³

To better understand why the interface problems frequently take place in the MODFET structure, we calculated the electron distribution in the channel by solving the one-dimensional Poisson's equation and Schrödinger equation consistently and quantum-mechanically along the depth direction.¹⁴ The simulation produces conduction band energy, electron distribution profile, and subband energy levels at different gate bias voltages. Figure 2(a) presents the conduction band and electron profile of the conventional D-MODFET corresponding to the structure of Fig. 1 at zero gate voltage. Two asymmetric peaks of the distribution are located very close to each interface, which indicates that the electron transport can be very sensitive to interface properties. The two peaks will become closer to each interface and will be separated from each other further if the QW thickness becomes larger. Moreover, assuming that the electron profile can be regarded as the superposition of two distributions, each with its own peak (one closer to the top interface and the other to the bottom one), they will probably interfere together along the trans-

^{a)} On leave from GoldStar Central Research Laboratory, Seocho-Gu, Seoul 137-140, Korea.

ized with a network analyzer and a pair of microwave probes calibrated by the short-open-load-through technique on an impedance standard substrate. The current gain cutoff frequency f_{c} extrapolated at -6 dB/octave

buffer	$\text{Al}_0.3\text{Ga}_{0.7}\text{As}$	150 Å
APD**	$\text{Si}_3\text{N}_4/\text{SiO}_2$	—
Spacer A	$\text{Al}_0.3\text{Ga}_{0.7}\text{As}$	50 Å
QW	$\text{In}_{0.2}\text{Ga}_{0.8}\text{As}$	100 Å
Spacer B	$\text{Al}_0.3\text{Ga}_{0.7}\text{As}$	20 Å
W	$\text{In}_{0.2}\text{Ga}_{0.8}\text{As}$	20 Å
Spacer C	$\text{Al}_0.3\text{Ga}_{0.7}\text{As}$	50 Å
APD	$\text{Si}_3\text{N}_4/\text{SiO}_2$	—
buffer	$\text{Al}_0.3\text{Ga}_{0.7}\text{As}$	500 Å
Si	Si	2000 Å

* Unpiped ** Atomic Planar Doping *** Superlattice
 QW : $\text{In}_{0.2}\text{Ga}_{0.8}\text{As}$ Uniform-Composition Structure
 $\text{In}_{x}\text{Ga}_{1-x}\text{As}$ Graded Structure

FIG. 1. Schematic cross section of conventional and graded double modulation-doped structures: left QW conventional structure, right QW graded structure.

port path where the aspect ratio of the typical source-drain distance ($1 \mu\text{m}$) to the QW thickness (100 \AA) is more than 100. The interference of two major peaks seems to be another reason that the mobility of D-MODFETs reported so far has not been as good as that of the single-doped MODFET¹⁵ ($7000 \text{ cm}^2/\text{V s}$). Most of the best reported mobility for typical $\text{Al}_{0.3}\text{Ga}_{0.7}\text{As}/\text{In}_{0.2}\text{Ga}_{0.8}\text{As}$ D-MODFETs are scattered around $6000 \text{ cm}^2/\text{V s}$ with N_d of $3.5-4.0 \times 10^{12}/\text{cm}^2$ at room temperature.^{16,17}

To improve the interface-related mobility characteristics of the D-MODFET, we designed a new $\text{Al}_{0.3}\text{Ga}_{0.7}\text{As}/\text{In}_{0.2}\text{Ga}_{0.8}\text{As}$ D-MODFET structure by linearly grading the In composition in the channel. We attempted to make the conduction band in the channel flatter than that of the conventional D-MODFET by decreasing the In composition at the top and the bottom interfaces, and increasing the In composition at the center of the channel. This compositional grading modifies the potential shape of the QW, resulting in a rectangular-like QW, which pushes both electron peaks near the interfaces toward the QW center. As a result, a broad and relatively symmetric electron distribution can be obtained, as shown in Fig. 2(b). If we try to cause a more sophisticated In profiling such as a nonlinear or a multistep grading, more symmetric electron distributions farther from the interface can be obtained under any operating gate voltage and donor density. It is worthwhile to point out that the energy difference between the first and the second subbands of the graded structure [Fig. 2(b)] case is larger by 11 meV than that of the conventional D-MODFET [Fig. 2(a)], which implies that there is less probability of the intersubband scattering.

Based on the above band gap grading concept, we grew a conventional D-MODFET structure (sample No. 4129) with uniform In concentration of 20% in the QW, and a compositionally graded one (sample No. 4130) by MBE. In the graded structure, the In concentration is 15% at bottom interface, linearly increased up to 22% through the center, and decreased down to 15% at the top interface. The average In concentration is 18.5%. All other structural and growth parameters except in the QW structure

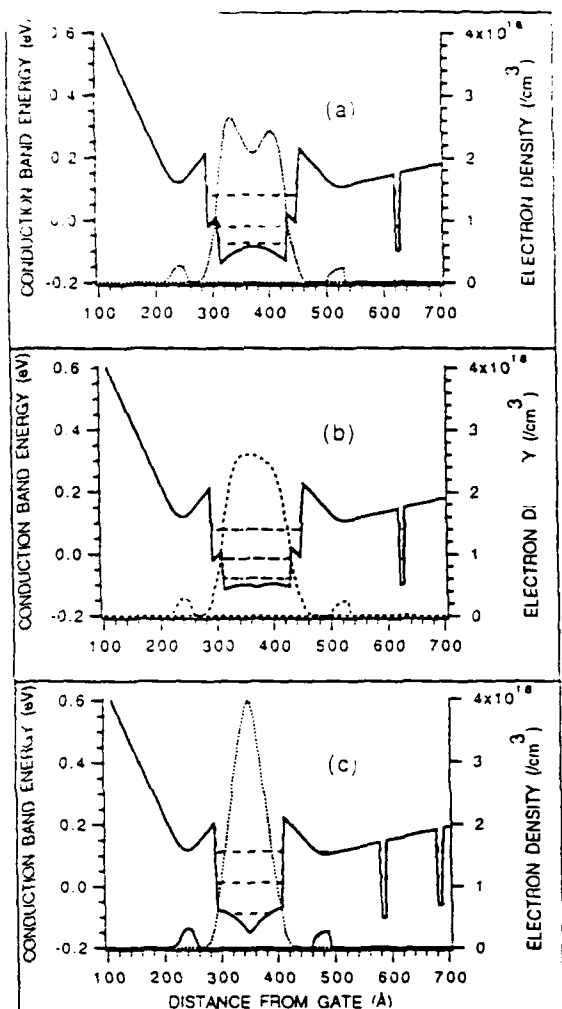


FIG. 2. Conduction band and electron distribution profiles at $V_g=0$ for the D-MODFET (a) conventional structure with uniform 20% In concentration, (b) graded structure with linear gradient of 15%-22%-15% In concentration, (c) graded structure with linear gradient of 5%-25%-5% In concentration.

were identical in both structures. In both cases, we used the well-calibrated Si APD technique and the 90 \AA $\text{Al}_{0.3}\text{Ga}_{0.7}\text{As}/10 \text{ \AA}$ GaAs superlattice buffer layers.

For accurate Hall measurements, we chose 3 samples from different positions in a 2 in. wafer for each structure and made the van der Pauw clover leaf patterns. We repeated Hall measurements after each chemical etching of the GaAs cap layer in a small step (stripping Hall measurement). The mobility and the sheet density of the conventional D-MODFET were measured to be $6520 \text{ cm}^2/\text{V s}$ and $4.1 \times 10^{12}/\text{cm}^2$ at room temperature, respectively. On the other hand, those of the graded structure were the extremely high mobility of $7230 \text{ cm}^2/\text{V s}$ and the sheet density of $4.1 \times 10^{12}/\text{cm}^2$ at room temperature. The 77 K mobility and the sheet density are also as high as $21630 \text{ cm}^2/\text{V s}$ and $3.9 \times 10^{12}/\text{cm}^2$, respectively. To our knowl-

TABLE I. Structural parameters and Hall data

Sample No	In concentration in QW (%)			Spacer thickness below QW (Å)	Hall measurement			
	Top	Center	Bottom		GaAs/AlGaAs	μ (cm ² /V s)	N ($\times 10^{12}$ cm ⁻²)	N_s (cm ⁻²)
4129	20	20	20	20/50	6520	17.830	4.1	3.8
4130	15	22	15	20/50	7230	21.630	4.1	3.9
4198	20	20	20	20/30	3030	7.260	2.2	2.0
4199	5	25	5	0/30	5390	16.050	2.5	2.2

edge, this high mobility with such a high sheet density of $4.1 \times 10^{12}/\text{cm}^2$ is the best ever reported for the AlGaAs/InGaAs D-MODFET. This mobility over $7000 \text{ cm}^2/\text{V s}$ at room temperature is quite significant because with such a high electron density, some parts of parallel conduction may still take place in the $\text{Al}_0.3\text{Ga}_0.7\text{As}$ barrier layers, where the electron mobility is quite poor.¹⁴ Table I summarizes the QW structures and Hall measurement data at 300 and 77 K.

To verify the effectiveness of the compositional grading on the mobility, we tried another MBE growth run. We intentionally degraded the mobility by using higher growth temperature to enhance the Si segregation,¹¹ and using thinner $\text{Al}_0.3\text{Ga}_0.7\text{As}$ spacer (30 Å instead of 50 Å). We grew two kinds of D-MODFET structure: one (sample No. 4198) is the conventional structure with a uniform In composition of 20%, and the other (sample No. 4199) is the graded one with a steeper gradient in In concentration. The In composition was linearly changed from 5% at both interfaces to 25% at the center, as summarized in Table I. In the latter case, we did not use the 20 Å GaAs spacer because the In concentration at the heterointerface is only 5%. According to the simulation shown in Fig. 2(c), the electron density is strongly concentrated around the QW center with the full width at half maximum less than 60 Å. Although the mobility was degraded on both structures as expected, the graded structure showed much less degraded mobility of 5390 $\text{cm}^2/\text{V s}$, compared to that of the conventional structure, 3030 $\text{cm}^2/\text{V s}$. This seems to suggest that the grading of the composition is indeed efficient in controlling the electron profile and providing the relative mobility-insensitivity to the interface conditions.

In conclusion, the potential shape of the InGaAs quantum well in AlGaAs/InGaAs MODFET structures can be controlled by the band gap grading of the well. The electron distribution profile in the rectangular-like InGaAs QW is broad and symmetric. Hall measurement shows that

the very high mobility and sheet density can be obtained at the same time in the graded structure, which can improve the performance of MODFET's.

This work was supported by the international collaboration program of the GoldStar Co. Ltd. One of the authors (Tae-Kyung Yoo) wishes to acknowledge Dr. Doyeol Ahn and Dr. In-Ku Kang of GoldStar for discussions and encouragement.

- ¹ W. J. Schaff and L. F. Eastman, *Strain-Layer Superlattice: Material Science and Technology: Semiconductor and Semimetal*, edited by T. P. Pearsall (Academic, New York, 1991), Vol. 33, Chap. 2, p. 73.
- ² J. W. Mathews and A. E. Blakeslee, *J. Cryst. Growth* **27**, 118 (1974).
- ³ L. D. Nguyen, P. J. Tasker, D. C. Raduiescu, and L. F. Eastman, *IEEE Trans. Electron Device* **ED-36**, 2243 (1989).
- ⁴ K. L. Tan, R. M. Dia, and H. C. Yen, *IEEE Electron Device Lett.* **EDL-11**, 585 (1990).
- ⁵ B. Kim, R. J. Matyi, M. Wurtele, K. Bradshaw, and H. Q. Tserng, *IEDM Tech. Dig.*, 168 (1988).
- ⁶ M. Hueschen, N. Moll, and A. Fischer-Colbrie, *IEDM Tech. Dig.* 596 (1987).
- ⁷ K. Inoue, K. Nishii, T. Matsuno, and T. Onuma, *IEDM Tech. Dig.* 422 (1987).
- ⁸ J. Dickmann, *Appl. Phys. Lett.* **60**, 88 (1992).
- ⁹ G. W. Wang, Y. K. Chen, and L. F. Eastman, *IEEE Electron Device Lett.* **EDL-9**, 4 (1988).
- ¹⁰ W.-P. Hong, J. Singh, and P. K. Bhattacharya, *IEEE Electron Device Lett.* **EDL-7**, 480 (1986).
- ¹¹ A. S. Brown, R. A. Metzger, J. A. Henige, L. Nguyen, M. Lui, and R. G. Wilson, *Appl. Phys. Lett.* **57**, 3610 (1991).
- ¹² P. Mandeville, H. Park, M. C. Foisy, R. W. Streeter, W. J. Schaff, and L. F. Eastman, presented at Workshop on Compound Semiconductor Devices and Integrated Circuits, San Rafael, Spain, May 24–27, 1992.
- ¹³ J.-K. Luo, H. Ohno, K. Matsuzaki, and H. Hasegawa, *Jpn. J. Appl. Phys.* **27**, 1831 (1988).
- ¹⁴ M. C. Foisy, Ph.D. thesis, Cornell University, 1990.
- ¹⁵ K. Hikosaka, S. Sasa, N. Harada, and S. Kuroda, *IEEE Electron Device Lett.* **EDL-9**, 241 (1988).
- ¹⁶ M.-Y. Kao, P. M. Smith, P. Ho, P. C. Chao, K. H. G. Duh, A. A. Jabra, and J. M. Ballingall, *IEEE Electron Device Lett.* **EDL-10**, 580 (1989).
- ¹⁷ P. Smith, L. Lester, P. Chao, B. Lee, R. Smith, J. Ballingall, and K. Duh, *IEDM Tech. Dig.* 854 (1987).

V. Publications

1. "Progress in High Frequency Heterojunction Field Effect Transistors", Lester F. Eastman, ESSDERC 90, Nottingham, England , (Sept. 11-13,1990) Inst. Phys. (Adam Higler) edited by W. Eccleston and P.J. Rosser, p. 619-624.
2. "High-Current Lattice-Strained $In_{0.59}Ga_{0.41}As/In_{0.52}Al_{0.48}As$ Modulation-doped Field-Effect Transistors Grown by Molecular Beam Epitaxy", J.B. Kuang, Y.K. Chen, D. Sivco, A.Y.Cho and L.F. Eastman, Appl. Phys. Lett. 57, 1784-1786 (Oct. 22, 1990).
3. "The In-plane Effective Mass in Strained-Layer Quantum Wells", B.K. Ridley, J. Appl. Phys. 68 4667-4673 (Nov. 1, 1990).
4. "Free Optical Vibrations of an Infinite Plate of Homogeneous Isotropic Elastic Matter", B.K. Ridley, Physical Review B 44 9002-9011 (Oct. 15, 1991).
5. "A Continuum Theory of Optical Phonon Hybrids and Their Interaction with Electrons in a Quantum Well", B.K. Ridley, SPIE's Symp. on Compound Semiconductor Physics and Devices - High Speed Electronics and Optoelectronics, Somerset, NJ (March 22-26, 1992) 1680, 92-100, (Ed. John Bowers/Umesh K. Mishra).
6. "Hot Carriers and the Frequency Response of Quantum Well Lasers", L.F. Lester and B.K. Ridley, J. Appl. Phys. 72 2579-2588 (Oct. 1, 1992)
7. "Optical Mode Hybrids in Quantum Wells, Superlattics and Slabs", B.K. Ridley, presented at European Physical Society Meeting, Regensburg, Germany (March 1993); Proceedings to be published.
8. "Pursuit of Phonon Scattering Suppression in Short Periodic AlAs/GaAs Multiple Quantum Well Structures", T.T. LeTran, W.J. Schaff, B.K.

Ridley, Y.-P. Chen, A. Clark and L.F. Eastman, submitted to J. Appl. Physics. (June 28, 1993).

9. "On the Suppression of Phonon-Electron Scattering in Short Periodic AlAs/GaAs Multiple Quantum Well Structures", T. T. LeTran, W.J. Schaff, B.K. Ridley, Y.-P. Chen, A. Clark, S. O'Keefe and L.F. Eastman, 14th Biennial IEEE/Cornell Conference on 'Advanced Concepts in High Speed Semiconductor Devices and Circuits', August 2-4, 1993, Proceedings to be published.

VI. Personnel

Faculty: L.F. Eastman

Senior Visitors and Staff: B.K. Ridley, W.J. Schaff and T.-K. Yoo

Graduate Students:

Y.-P. Chen

A. Clark

T. T. LeTran

H.C. Park- Ph.D. Thesis "Epitaxial Layer Design of Pseudomorphic MODFET's for High-Frequency Power Applications" (Jan. 1993).

P. Mandeville - Ph.D. Thesis "Molecular-Beam Epitaxial Growth and Characterization of Pseudomorphic Double Modulation-Doped Field Effect Transistor Structures on Gallium Arsenide" (Jan. 1993).

VII. Inventions

"Heterostructure Field Effect Transistor with a Graded Composition", T.-K. Yoo, H. Park, P. Mandeville, W.J. Schaff and L.F. Eastman, submitted October 1992 - decision by Cornell Research Foundation not to pursue patent on May 18, 1993.

Appendix
Papers Published

Progress in High Frequency Heterojunction Field Effect Transistors

Lester F. Eastman

School of Electrical Engineering and National Nanofabrication
Facility, Cornell University, Phillips Hall,
Ithaca, New York, 14853-5401

Abstract. The concepts, technology and the present experimental limits of performance of heterojunction modulation doped field effect transistors are covered. Both lattice-matched and strained, pseudomorphic quantum well channels on GaAs substrates, as well as lattice-matched quantum well channels on InP substrates are included. Power gain frequency limits to 450 GHz, and noise figures as low as .8-.9 db at 60 GHz are presented for 300K operation of the latter devices.

1. Introduction

Microwave and millimeter wave field effect transistors have reached impressive performance levels by the use of heterojunctions. In these structures, a lower band-gap layer holds the electrons, while a higher band-gap layer is doped with donor atoms. As well as lattice-matched combinations on GaAs and InP substrates, thin strained layers have been used to hold the electrons. Very short gates have been realized using electron-beam lithography. This presentation covers the materials used, the fabrication methods, the materials and device assessment methods, and the present performance limits.

2. Materials

The initial results used $Al_{0.3}Ga_{0.7}As/GaAs$, where an undoped .5 - 1.0 μm GaAs buffer layer was grown on the GaAs semi-insulating substrate. The electron sheet density in the GaAs is limited to $.8 - .9 \times 10^{12}/cm^2$ in such a structure, due to the limited conduction-band potential step of .24V. At low temperatures there is a high electron mobility, ranging from $90,000 \text{ cm}^2/\text{V}\cdot\text{s}$ up to $220,000 \text{ cm}^2/\text{V}\cdot\text{s}$ at 77K. The latter result is only possible with low electron sheet density and with a substantial ($\sim 200 \text{ \AA}$) undoped region in the

Al_xGaAs near the heterojunction. Increasing the fraction of Aluminum does not allow higher electron sheet density because the energy of the donors in the Al_xGaAs does not rise more than .16 eV above the GaAs conduction band edge.

In order to increase the donor energy above the conduction band edge, Indium can be added to a thin, pseudomorphic channel layer holding the electrons. With In_{.15}Ga_{.85}As in this channel, electron sheet density values to $1.6 - 1.7 \times 10^{12}/\text{cm}^2$ are achievable, and with In_{.25}Ga_{.75}As the sheet density can reach $2.4 - 2.5 \times 10^{12}/\text{cm}^2$. In this latter case, the conduction band potential step is .44V. Mobility of electrons is lowered a modest amount at 300K, but is severely lowered at 77K, dropping from $90,000 \text{ cm}^2/\text{V-s}$ for no In, to $18,000 \text{ cm}^2/\text{V-s}$ for 25% Indium.

Using InP substrates, Al_{.48}In_{.52}As/Ga_{.47}In_{.53}As structures have been used to achieve improved results. In this case the conduction band potential step at the heterojunction is .52 eV and the electron sheet density can be at least $3 \times 10^{12}/\text{cm}^2$. In addition, electrons have only two thirds as much effective mass, which raises the room temperature mobility by about 50%. The 77K electron mobility is limited by alloy scattering, and to date has not surpassed the $60,000-70,000 \text{ cm}^2/\text{V-s}$ region.

In order to achieve high performance in transistors with short gates, electrons must be confined by a potential barrier from beneath as well as on top. Instead of thick layers of the barrier alloy, a superlattice such as Al_{.3}Ga_{.7}As/GaAs/Al_{.3}Ga_{.7}As etc, is used.

On top of the doped barrier layer, which usually contains Aluminum, there is normally placed a cap layer having no Aluminum. This layer is doped, as needed, to limit the depletion of the desired electron sheet density along the channel. The ohmic contact alloying can more easily penetrate such cap layers having no Aluminum due to the absence of Aluminum oxide.

3. Transistor Structures

The modulation-doped field effect transistors (MODFET's) are fabricated using electron-beam lithography. High performance is achievable with short gates, with $\sim .15 \mu\text{m}$ gate lengths. Such gates are made with a cross section having a mushroom shape, or T-shape, with a short "footprint" but with an enlarged metal conductor region above the semiconductor. Such structures

can be fabricated with $\leq 200 \Omega/\text{mm}$ resistance along their length. Without the mushroom shape, such gates would have 8-10 times as high a resistance. It would require six gate fingers, each with one sixth the length, to achieve the same performance as two fingers with mushroom shape.

The layout of the MODFET pattern should be designed to have low gate-to-drain feedback capacitance, in order to yield a high value of power gain. This allows the unity-power-gain frequency, f_{\max} , to be 1.5 - 2.0 times as high as the unity-current-gain frequency f_T .

On GaAs substrates, the pseudomorphic $\text{In}_y\text{Ga}_{1-y}\text{As}$ channel has interrelated limits on thickness and Indium fraction. Above $y \approx .22$ the surface of the In_yGaAs is often rough, lowering yield. At $y = .25$ the maximum thickness of this layer is limited to $\sim 100 \text{ \AA}$, since dislocations form for thicker layers. As shown in Figure 1, this causes a sharp reduction in mutual transconductance, g_m . For quantum well thickness = 0, this is simply a GaAs channel MODFET. The g_m and f_T are both about 50% higher for the optimum $\text{In}_{.25}\text{Ga}_{.75}\text{As}$ quantum well, compared with a GaAs quantum well. Figure 2 shows the current gain versus frequency for a MODFET with an optimum $\text{In}_{.25}\text{Ga}_{.75}\text{As}$ channel and $.15 \mu\text{m} \times 150 \mu\text{m}$ mushroom gate. The room-temperature f_T shown is the present record value for pseudomorphic $\text{InGaAs}/\text{GaAs}$. (Nguyen, et al, 1989) The room-temperature f_{\max} of a MODFET with the same quantum well and $.15 \mu\text{m} \times 6.0 \mu\text{m}$ gate was 250 GHz. With lower f_T (100 GHz), f_{\max} has been as high as 350 GHz on such devices (Lester et al. 1988).

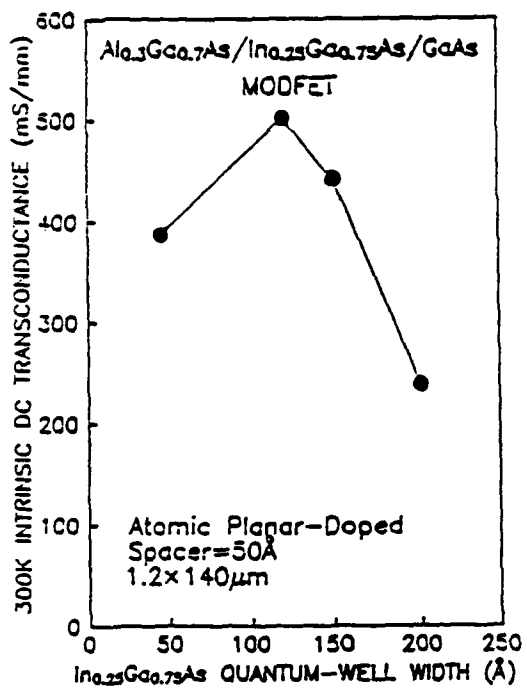


Fig. 1. Mutual transconductance of $\text{In}_{.25}\text{Ga}_{.75}\text{As}/\text{GaAs}$ MODFETs versus strained-layer thickness.

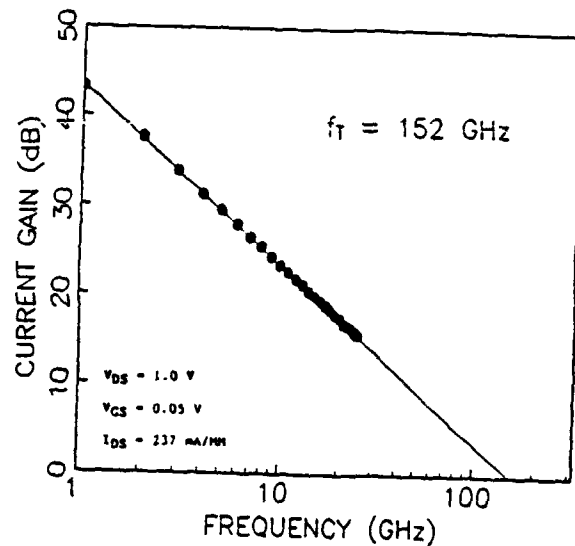


Fig. 2. Current gain performance of $\text{In}_{0.25}\text{Ga}_{0.75}\text{As}/\text{GaAs}$ pseudomorphic $0.15 \times 150 \mu\text{m}$ MODFET versus frequency.

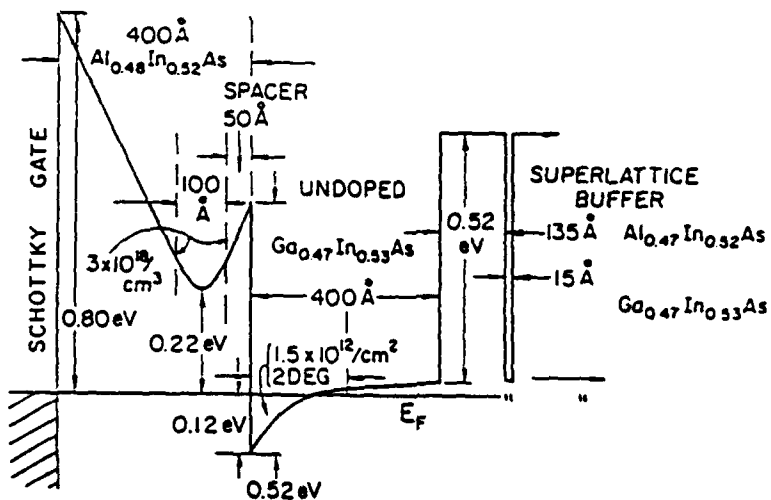


Figure 3. Conduction band potential profile of an $\text{Al}_{0.48}\text{In}_{0.52}\text{As}/\text{Ga}_{0.47}\text{In}_{0.53}\text{As}/\text{InP}$ MODFET with superlattice buffer layer.

Devices of this type have yielded 1.6 db noise figure at 60 GHz for .15 μ m gates at room temperature.

MODFET's with Al_{.48}In_{.52}As barriers, and Ga_{.47}In_{.53}As channels lattice-matched to InP have yielded the highest frequency performance for a given gate length. Figure 3 shows a scale drawing of the conduction band profile for such a device. The conduction band potential step is .52 V at the interface, allowing electron sheet density up to $\sim 3 \times 10^{12}/\text{cm}^2$ as well as $\sim 50\%$ higher mobility values than for quantum well channels on GaAs. In addition, electron average transit velocity is at least one third higher. There are still problems related to gate leakage, channel breakdown, electron traps in the AlInAs, and reliability with these devices on InP, but dedicated research to improve these areas has just begun. These devices have yielded .8-9 db noise figures at 60 GHz for .15 μ m gates at room temperature. The best, room temperature values for f_t (Mishra) and f_{max} (Chao and Smith (a)) are 250 and 450 GHz, respectively for these devices. In comparing devices on GaAs and InP substrates, the expected frequency response as a function of gate length is shown in Figure 4. The quantitative values for the maximum electron sheet density, and average electron transit velocity are given in Table 1.

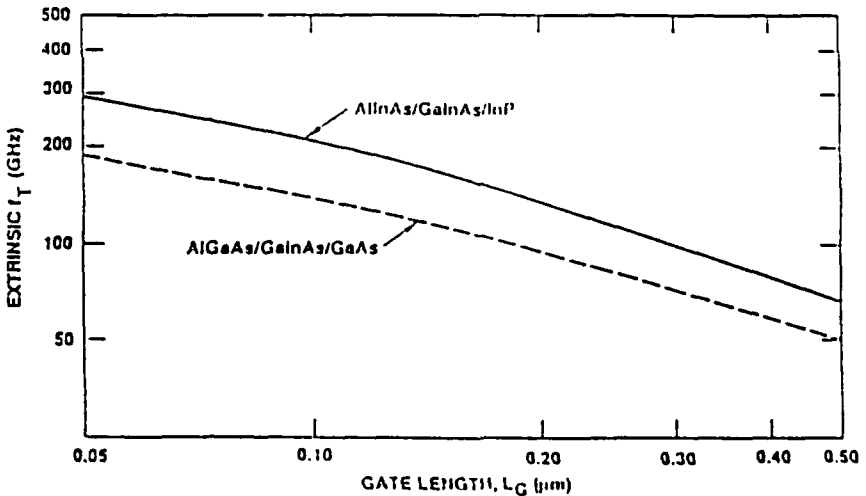


Fig. 4. Expected frequency response of optimum MODFET's on GaAs and InP substrates versus gate length.

TABLE 1

Channel	Electron Sheet Density	Average Electron Transit Velocity
GaAs	$.8\text{-.9}\times 10^{12}/\text{cm}^2$	1.2×10^7 cm/s
In _{.25} Ga _{.75} As	$2.4\text{-.5}\times 10^{12}/\text{cm}^2$	1.8×10^7 cm/s
Ga _{.47} In _{.53} As	$3\text{-.3.2}\times 10^{12}/\text{cm}^2$	2.4×10^7 cm/s

4. Conclusions

It is concluded that MODFET's have the highest frequency response and the lowest noise figures of any transistors. Those MODFET's on InP substrates have the highest f_t and f_{max} and the lowest noise figure, while those MODFET's on GaAs substrates have the highest power (Chao and Smith (b)) and efficiency (Chao and Smith (b)) (.66W/mm at 41% efficiency at 60 GHz and .36 W/mm at 23% efficiency at 94 GHz).

5. Acknowledgements

Support from ONR, ARO, AFOSR, Boeing, IBM, Hughes, GE, Motorola and ITT are gratefully acknowledged.

6. References

Chao P C and Smith P (a) G.E. Syracuse, *private communication*.
 Chao P C and Smith P (b) G.E. Syracuse, *private communication*.
 Lester L, Tiberio R, Wolf E, Smith P, Ho P, Chao P and Duh G, 1988, *Proc. IEDM*, 172-175.
 Mishra U, Hughes Research Laboratory, *private communication*.
 Nguyen L D, Tasker P J, Radulescu D C and Eastman L F, 1989 *IEEE Trans. Elec. Dev.* 36 2243-2248.

High-current lattice-strained $\text{In}_{0.59}\text{Ga}_{0.41}\text{As}/\text{In}_{0.52}\text{Al}_{0.48}\text{As}$ modulation-doped field-effect transistors grown by molecular beam epitaxy

J. B. Kuang

School of Electrical Engineering, Cornell University, Ithaca, New York 14853

Y. K. Chen, D. Sivco, and A. Y. Cho

AT&T Bell Laboratories, Murray Hill, New Jersey 07974

L. F. Eastman

School of Electrical Engineering, Cornell University, Ithaca, New York 14853

(Received 2 May 1990; accepted for publication 30 July 1990)

High-current driving capability is realized in submicron-gate lattice-strained $\text{In}_{0.59}\text{Ga}_{0.41}\text{As}/\text{In}_{0.52}\text{Al}_{0.48}\text{As}$ ($\Delta a/a = 4 \times 10^{-3}$) modulation-doped field-effect transistors. Full-channel drain current in excess of 1.10 and 1.90 A/mm are obtained at 80 K for the singly doped and doubly doped structure, respectively. By using the double modulation technique and a buried *p*-buffer layer, excellent high-frequency performance and flat transconductance characteristics were realized over a very broad range of gate and drain bias voltages.

These devices are very suitable for large-signal or power device operations. The high quality $\text{In}_{0.52}\text{Al}_{0.48}\text{As}$ buffer layer eliminates the hysteresis and current instability (or the kink effect) in submicron-gate devices at both 300 and 80 K.

Excellent high-frequency performance was previously reported in the lattice-matched $\text{In}_{0.53}\text{Ga}_{0.47}\text{As}/\text{In}_{0.52}\text{Al}_{0.48}\text{As}$ modulation-doped field effect transistors (MODFETs).^{1,2} However, most of these devices utilize a single electron supplying layer, and the current driving capability is limited. Lattice-strained $\text{In}_x\text{Ga}_{1-x}\text{As}/\text{In}_{0.52}\text{Al}_{0.48}\text{As}$ ($x > 0.53$) modulation-doped heterostructures promise higher electron mobility and larger conduction band-edge discontinuity than the lattice-matched structures.³⁻⁷ Higher electron mobilities and velocities are expected in the strained structures due to the better electron confinement and reduced scattering.^{8,9} Larger conduction-band-edge discontinuity in the strained structures also results in a better electron confinement and a larger sheet electron concentration. Reduced scattering⁸ in the channel further raises the electron mobility and effective velocity. In this letter we report the realization of high-frequency, high-current MODFETs by utilizing a lattice-strained quantum well channel and doubly doped wide-gap electron supplying layers. A full channel drain current over 1 A/mm is demonstrated in both the strained singly doped (SD) and doubly doped (DD) $\text{InGaAs}/\text{InAlAs}$ MODFET structures with 6% excess indium in the channel. The large current density together with the higher thermal conductivity of InP than GaAs makes these devices potential candidates for high-speed large-signal applications such as millimeter-wave power amplification and laser drivers for multigigabit optical link.

The strained SD and DD heterostructures were grown by molecular beam epitaxy on the semi-insulating InP substrates. Schematic cross-sectional layer structures and the conduction-band-edge diagrams are shown in Figs. 1(a), 1(b), and 1(c), respectively. For the SD structure, both the capping and electron supplying layer have a silicon doping level of $5 \times 10^{18}/\text{cm}^3$. For the DD structure, the silicon doping level of the capping, upper, and lower electron supplying layer are 5×10^{18} , 5×10^{18} , and $3 \times 10^{18}/\text{cm}^3$,

cm^3 , respectively; and the beryllium doping level in the buried *p*-buffer layer is $8 \times 10^{17}/\text{cm}^3$. The $\text{In}_{0.59}\text{Ga}_{0.41}\text{As}$ channel growth was performed with 20% lower Ga flux to achieve the 6% higher indium mole fraction. The potential barrier of the *p*-buffer layer in the DD structure further improves the carrier confinement and isolates the two-dimensional electron gas (2 DEG) from the substrate defects and impurities.

MODFETs were fabricated with a recess-gate process. A planar isolation was realized by boron ion implantation at 35 keV with a dose of $1 \times 10^{13}/\text{cm}^2$. Breakdown voltages exceeding 200 V were measured between two active regions separated by a 15 μm spacing, justifying the effectiveness of the isolation process. From the four-point probe measurements of the annealed Ni/AuGe/Ag/Au ohmic contacts, contact resistances of 0.14 and 0.13 $\Omega \text{ mm}$, specific contact resistivities of 1.79×10^{-6} and $1.89 \times 10^{-6} \Omega \text{ mm}^2$, and sheet resistivities of 110 and 92 Ω/\square were measured at 300 K for the SD and DD structure, respectively. The sheet resistivity was measured with the capping layers. At 80 K, the sheet resistivity dropped below 50 Ω/\square for both structures as the result of the increase in the carrier mobilities and 2 DEG densities. A recess etch was performed to remove the n^+ -InGaAs capping layer before depositing the electron beam defined T-shaped¹⁰ Ti/Pd/Au gates on the 200 \AA undoped InAlAs layer. This is essential to reduce the gate diode leakage current. The measured dc end-to-end gate resistances were smaller than 200 Ω/mm for gate footprints of various submicron dimensions.

Figure 2 shows a typical drain current-voltage characteristics of a $0.36 \times 50 \mu\text{m}^2$ gate device for the DD structure at 300 K. Similar characteristics are obtained in the SD structure with a lower current level. At a bias point of $V_{ds} = 2.5 \text{ V}$ and $V_g = 0 \text{ V}$, the devices are able to deliver a current density of 0.9 (300 K) and 1.07 (80 K) A/mm for the SD structure and 1.5 (300 K) and 1.8 (80 K) A/mm for the DD structure. There is a 20% increase of drain

200 Å	n ⁺	In _{0.53} Ga _{0.47} As	CAPPING LAYER
200 Å	i	In _{0.52} Al _{0.48} As	BARRIER LAYER
300 Å	n ⁺	In _{0.52} Al _{0.48} As	ELECTRON SUPPLYING LAYER
20 Å	i	In _{0.52} Al _{0.48} As	SPACER
225 Å	i	In _{0.59} Ga _{0.41} As	CHANNEL
1 μm	i	In _{0.52} Al _{0.48} As	BUFFER LAYER
SEMI-INSULATING InP SUBSTRATE			

(a)

200 Å	n ⁺	In _{0.53} Ga _{0.47} As	CAPPING LAYER
200 Å	i	In _{0.52} Al _{0.48} As	BARRIER LAYER
300 Å	n ⁺	In _{0.52} Al _{0.48} As	ELECTRON SUPPLYING LAYER
20 Å	i	In _{0.52} Al _{0.48} As	SPACER LAYER
225 Å	i	In _{0.59} Ga _{0.41} As	CHANNEL
30 Å	i	In _{0.52} Al _{0.48} As	SPACER LAYER
120 Å	n ⁺	In _{0.52} Al _{0.48} As	ELECTRON SUPPLYING LAYER
30 Å	i	In _{0.52} Al _{0.48} As	SET-BACK LAYER
25 Å	p ⁺	In _{0.52} Al _{0.48} As	BURIED P-BUFFER LAYER
1 μm	i	In _{0.52} Al _{0.48} As	BUFFER LAYER
SEMI-INSULATING InP SUBSTRATE			

(b)

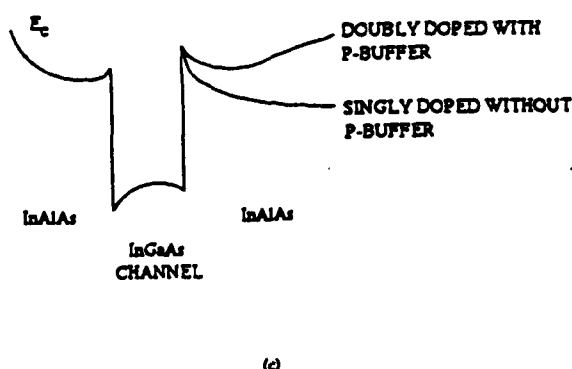


FIG. 1. Epitaxial layer structures of the lattice-strained (a) singly and (b) doubly doped In_{0.53}Ga_{0.47}As/In_{0.52}Al_{0.48}As MODFETs. (c) conduction-band-edge diagrams for both structures.

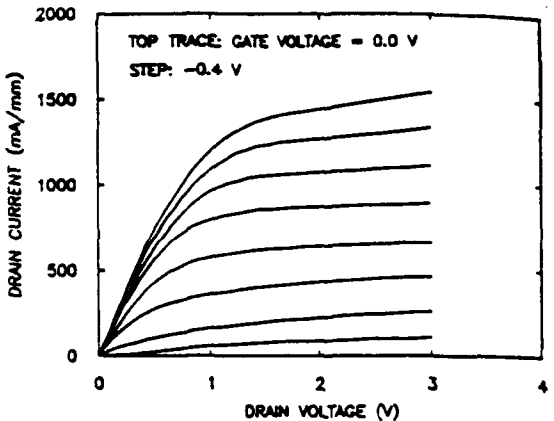


FIG. 2. Current-voltage characteristics of a $0.36 \times 50 \mu\text{m}^2$ gate doubly doped device at 300 K.

current for both structures at 77 K. The full channel drain current is over 1.10 A/mm for the SD structure and 1.90 A/mm for the DD structure at 80 K. The high current level also indicates the effective activation of silicon doping through the high quality epitaxial growth and efficient charge transfer from the electron supplying layer to the quantum well channel. Hysteresis and drain current anomalies (or the kink effects) in the current-voltage curves, as commonly observed in the short-gate InP-based devices, are not present at both 300 and 80 K. We attribute this to the low impurity and defect densities in the high quality InAlAs layer. With an appropriate heat sink for power consumption, the devices can sustain a drain voltage up to 3.5 V.

The peak extrinsic dc transconductance (g_m) is 511 (300 K) and 645 (80 K) mS/mm for the SD structure and 545 (300 K) and 646 (80 K) mS/mm for the DD structure at $V_{ds} = 1.0$ V as shown in Fig. 3. The current density under the high g_m bias condition is still over 0.50 and 0.65 A/mm at both 300 and 80 K for the SD and DD structure, respectively. The improved transconductance and

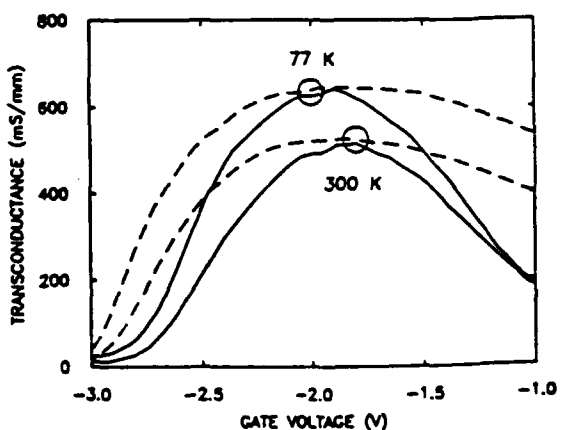


FIG. 3. dc transconductance vs gate voltage for a $0.36 \times 50 \mu\text{m}^2$ gate singly and doubly doped device at 300 and 80 K. (Solid lines) singly doped device; (broken lines), doubly doped device.

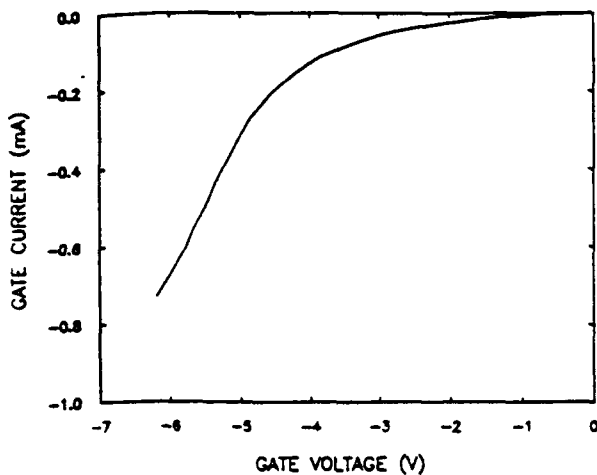


FIG. 4. Typical reverse-biased current-voltage characteristics of a $0.36 \times 50 \mu\text{m}^2$ gate-to-drain Schottky diode at 300 K.

increased drain current at 80 K are the results of better electron confinement and mobility enhancement from the lattice-strained heterostructures. The high g_m is maintained over a broad range of V_{ds} from 0.8 V and up. At $V_{ds} = 1.0$ V, g_m is greater than 520 mS/mm in both structures for a full range of V_g from -1.55 to -2.60 V at 80 K. This bias insensitivity of g_m is very desirable to minimize the harmonic distortions for large-signal operations.

Figure 4 shows the reverse-biased gate-to-drain Schottky diode characteristics of a $0.36 \times 50 \mu\text{m}^2$ gate device at 300 K. A breakdown of -6 V is measured. Although not quite comparable with the similar GaAs/AlGaAs devices, the gates perform reasonably well among the usually leaky InGaAs/InAlAs devices especially under the present condition of high carrier densities. This indicates the effectiveness of the 200 Å undoped InAlAs barrier layer. The pinch-off voltages for both structures are deep. This makes high drain voltage and very negative gate voltage bias conditions impractical due to the gate diode leakage current consideration. (For example, at $V_{ds} = 3.2$ V and $V_g = -3$ V, a 6.2 V reverse voltage is applied to the gate diode.) To operate the devices in the medium and ultimately high power regime, further improvements in the gate characteristics can be achieved by employing a thicker InAlAs barrier layer or increasing Al mole fraction of the InAlAs barrier layer.

The microwave performance of devices was character-

ized with a network analyzer and a pair of microwave probes calibrated by the short-open-load-through technique on an impedance standard substrate. The current gain cutoff frequency f_t extrapolated at -6 dB/octave from h_{21} , is 51 ± 2 and 42 ± 1 GHz for the SD and DD structure, respectively. The maximum stable gain is 11 ± 1 and 11.6 ± 1 dB at 26 GHz for the SD and DD structure, respectively. The lower f_t ($\approx g_m/2\pi[C_{gs} + C_{gd}]$) in the DD structure is due to larger parasitic capacitances ($C_{gs} + C_{gd}$) despite the higher g_m . Both the current and power gains vary very little over a broad gate and drain bias range. Combined with the simultaneous high current density and improved gate breakdown voltage, this structure is very suitable for the high-speed digital and millimeter-wave applications.

In summary, we have fabricated the lattice-strained $\text{In}_{0.59}\text{Ga}_{0.41}\text{As}/\text{In}_{0.52}\text{Al}_{0.48}\text{As}$ MODFETs with a high current driving capability and kink-free characteristics. The increase of conduction-band-edge discontinuity by employing a strained structure is effective in enhancing 2 DEG densities. The broad bias range of gate and drain voltages which achieve high transconductance and high current simultaneously is very attractive for large signal operations. With further optimization in gate characteristics, they are potential candidates for power device applications.

This work was supported in part by GE, ARO, and AT&T.

- 1 U. K. Mishra, J. F. Jensen, A. S. Brown, L. M. Jellouli, L. H. Hackett, and M. J. Delaney, *IEEE Electron Device Lett.* **EDL-9**, 41 (1988).
- 2 P. Ho, P. C. Chao, K. H. G. Duh, A. A. Jabra, J. M. Ballingall, and P. M. Smith, *IEDM Tech. Dig.* 184 (1988).
- 3 U. K. Mishra, A. S. Brown, and S. E. Rosenbaum, *IEDM Tech. Dig.* 180 (1988).
- 4 J. M. Kuo, T. Y. Chang, and B. Lalevic, *IEEE Electron Device Lett.* **EDL-8**, 380 (1987).
- 5 M. D. Jaffe, Y. Sekiguchi, J. Singh, Y. J. Chan and D. Pavlidis, *IEEE Proceedings/Cornell Conference* (Institute of Electrical and Electronics Engineers, Piscataway, NJ, 1987), p. 70.
- 6 G. I. Ng, D. Pavlidis, M. Tutt, J. -E. Oh, and P. K. Bhattacharya, *IEEE Electron Device Lett.* **EDL-10**, 114 (1989).
- 7 A. Fathimulla, J. Abrahams, H. Hier, T. Loughran, and E. Hempfing, in *Proceedings of 15th International Symposium on GaAs and Related Compounds*, edited by J. S. Harris (Institute of Physics, Bristol and Philadelphia, 1988), p. 455.
- 8 W.-P. Hong, G. I. Ng, P. K. Bhattacharya, D. Pavlidis, and S. Willing, *J. Appl. Phys.* **64**, 1945 (1988).
- 9 H. T. Griem, U. K. Mishra, A. S. Brown, C. E. Hooper, J. A. Henige, R. Hart, and L. F. Eastman, presented at *Electron. Material Conf.*, Boulder, CO, June, 1988.
- 10 G.-W. Wang, Y.-K. Chen, W. J. Schaff, and L. F. Eastman, *IEEE Trans. Electron Devices*, **ED-35**, 818 (1988).

The in-plane effective mass in strained-layer quantum wells

B. K. Ridley^a

School of Electrical Engineering, Cornell University, Phillips Hall, Ithaca, New York 14853-5401

(Received 28 March 1990; accepted for publication 3 July 1990)

The problem of calculating the valence-band structure of strained-layer quantum wells in the effective-mass approximation is reviewed. Using the spherical approximation and exploiting the simplicity of the infinitely deep well model we show that the in-plane effective mass is determined by two factors—a splitting contribution which is dominant at large strains, and a quantum confinement contribution. A model for finite-depth wells is presented which gives analytic expressions for the zone-center in-plane mass and associated nonparabolicity factor, and it is applied to the system $\text{In}_x\text{Ga}_{1-x}\text{As}/\text{GaAs}$. The model allows the computation of valence-band structure using no more than a pocket calculator. It is shown to give results in reasonable agreement with experiment.

I. INTRODUCTION

It has been known for over 30 years that uniaxial or biaxial strains can split the heavy- and light-hole valence bands in semiconductors at the zone center.¹ An interesting result of this splitting is the phenomenon of mass reversal in which the heavy-hole band acquires a light mass in, say, the xy plane but retains its heavy mass in the z direction, whereas the light-hole band acquires a heavy mass in the xy plane but retains its light mass in the z direction, the xyz directions being determined by the orientation of the strains. The potential of this structure to exhibit negative differential resistance (NDR) was realized long ago,² and recently its advantages for lasers regarding the provision of a low threshold current,³ reduced intervalence-band absorption, and reduced Auger recombination⁴ has led to a major activity in the investigation of strained layers.⁵ The latter are obtained by growing an epilayer on a lattice-mismatched substrate, and these layers are stable and dislocation-free provided the layer thickness does not exceed a critical value, which is typically 50–1000 Å (the bigger the strain, the smaller the critical thickness). Interest has therefore focused on strained-layer quantum-well structures in which the effects of quantum confinement are added to those associated with strain.

Theoretical work in this area is based on the effective-mass formalism of Luttinger and Kohn,^{6,7} a formalism which works in the case of quantum confinement only provided that the periodic part of the Bloch function in the well is the same as that in the barrier. Where this is not the case a full-blown band-structure calculation cannot be avoided. Even when the effective-mass formalism holds well, keeping track of the altered mixing of heavy- and light-hole states brought about by confinement warrants a numerical treatment. The problem has been discussed by Altarelli⁸ and Marzin.⁹ When the growth of the layer is along a (111) direction the complexity is compounded by the appearance of a substantial electric field via the piezoelectric effect.¹⁰ In many cases in practice the effective-mass approximation is expected to give reasonable results, and we will restrict our

attention to these cases in what follows. For purposes of device modeling it is desirable to minimize the amount of numerical computation, limiting the latter if possible to what can be done on a pocket calculator. To this end there are several simplifying assumptions which can be adopted, and these will be briefly reviewed in the next section. Our aim will be to evolve out of these a simple model which contains the essential features of the physics, and we will apply this to the $\text{In}_x\text{Ga}_{1-x}\text{As}/\text{GaAs}$ system.

II. BASIC THEORY

The basic problem in the context of the effective-mass formalism and $\mathbf{k}\cdot\mathbf{p}$ theory is to obtain the allowed electron energy states taking into account the coupling between two conduction-band states (spin up–spin down), and six valence-band states (three spin up–spin down), but neglecting changes brought about by more remote bands. (This is the first approximation.) The effect of strain via deformation potentials can be incorporated into the Luttinger–Kohn Hamiltonian, as can piezoelectric fields, but we will limit attention to simple biaxial or uniaxial strains along (100) directions so that piezoelectric fields do not exist. Piezoelectricity is connected with the lack of a centre of inversion symmetry in the crystal lattice, and this produces an asymmetry in the energy structure, but this effect is small and we will neglect it. Each eigenfunction is a linear combination of the eight basic wave functions,¹¹ which are themselves linear combinations of $|P\rangle(|x\rangle, |y\rangle, |z\rangle)$ orbitals chosen to properly quantize total angular momentum along the z direction in the presence of the spin-orbit interaction. In bulk material the Hamiltonian is an 8×8 matrix with the allowed energies being given by the solutions of an 8×8 secular determinant. When an interface is present, continuity of wave function and current leads to a 16×16 determinant to solve (32 \times 32 if no inversion symmetry).

While this presents no difficulty in principle many of the inherent details which expand the need for computational power are often of minimal interest—for example, the anisotropic, as distinct from the nonparabolic, features of band structures. Moreover, the interaction of bands widely separated in energy is weak and this can form the basis of a significant simplification. Thus when the band gap is large the

^a Home address: Department of Physics, University of Essex, Colchester, UK

conduction band and valence bands can be decoupled, and when the spin-orbit splitting is large the split-off band can be decoupled from the rest. As a result the 8×8 Hamiltonian matrix splits into two 2×2 matrices and one 4×4 matrix. This is a powerful simplification which is often justifiable in practice. The 2×2 matrices describe bands (conduction band and split-off band) which are spherical and parabolic to a good approximation.

The solution of the 4×4 secular determinant in bulk material gives the energy of the light-hole/heavy-hole bands as a function of \mathbf{k} and its components k_x, k_y, k_z along the cube axes as follows:

$$E = E_s + (\hbar^2/2m) \{ -\gamma_1 k^2 \pm [4\gamma_2^2 k^4 + 12(\gamma_1^2 - \gamma_2^2) \times (k_x^2 k_y^2 + k_y^2 k_z^2 + k_z^2 k_x^2) + 2\gamma_2 (k_x^2 + k_y^2 - 2k_z^2) K^2 + K^4]^{1/2} \}, \quad (1)$$

where $\gamma_1, \gamma_2, \gamma_3$ are the Luttinger parameters,⁷ E_s is the shift in energy due to the hydrostatic component of the stress, and K is the equivalent wavevector associated with the splitting strain energy δ , viz.,

$$K^2 = 2m\delta/\hbar^2. \quad (2)$$

In the case of a biaxial stress,

$$E_s = 2a \frac{(c_{11} - c_{12})}{c_{11}} e_s, \quad \delta = b \frac{(c_{11} + 2c_{12})}{c_{11}} e_s, \\ e_s = \frac{\Delta a_0}{a_0}, \quad (3)$$

where a and b are valence-band deformation potentials, c_{11} and c_{12} are elastic constants, e_s is the strain associated with the difference between lattice constants Δa_0 of well and barrier (the latter assumed to be unstrained), and a_0 is the lattice constant in the well, and we assume that compressive strains are positive. In Eq. (1) the upper sign refers to the heavy-hole (HH) band, the lower to the light-hole (LH) band.

Each of the four eigenfunctions is of the form

$$\Psi = (A |\{\}, \{\}\rangle + B |\{\}, \{\}\rangle + C |\{\}, -\{\}\rangle + D |\{\}, -\{\}\rangle) e^{i\mathbf{k}\cdot\mathbf{r}}. \quad (4)$$

They can be most easily represented as column matrices,¹⁰ thus

$$H_1(\mathbf{k}) = \begin{vmatrix} R_1 \\ -L \\ -M \\ 0 \end{vmatrix} e^{i\mathbf{k}\cdot\mathbf{r}}, \quad H_2(\mathbf{k}) = \begin{vmatrix} 0 \\ -M \\ L \\ R_1 \end{vmatrix} e^{i\mathbf{k}\cdot\mathbf{r}}, \\ L_1(\mathbf{k}) = \begin{vmatrix} -L \\ R_2 \\ 0 \\ -M \end{vmatrix} e^{i\mathbf{k}\cdot\mathbf{r}}, \quad L_2(\mathbf{k}) = \begin{vmatrix} -M \\ 0 \\ R_2 \\ L \end{vmatrix} e^{i\mathbf{k}\cdot\mathbf{r}}, \quad (5)$$

where

$$R_1 = P - Q + E - E_s, \quad R_2 = P + Q + E - E_s,$$

$$P = \frac{\hbar^2}{2m} \gamma_1 k^2, \quad Q = \frac{\hbar^2}{2m} \gamma_2 (k_x^2 + k_y^2 - 2k_z^2) + \delta,$$

$$L = -i \frac{\hbar^2}{2m} 3\sqrt{3} \gamma_1 (k_x - ik_y) k_z, \quad (6)$$

$$M = \frac{\hbar^2}{2m} [\gamma_2 \sqrt{3}(k_x^2 - k_y^2) - i\gamma_1 2\sqrt{3} k_x k_y].$$

The character of the state becomes pure heavy hole or pure light hole when k_x and k_y are zero. In this case L and M , the off-diagonal terms in the Hamiltonian, are zero and

$$E = E_s - \frac{\hbar^2}{2m} (\gamma_1 \mp 2\gamma_2) k_z^2 \mp \delta. \quad (7)$$

Thus, R_1 is finite and R_2 is zero when the upper sign is taken, which corresponds to the heavy-hole state with effective mass ratio equal to $(\gamma_1 - 2\gamma_2)^{-1}$. The lower sign gives the pure light-hole state with effective-mass ratio equal to $(\gamma_1 + 2\gamma_2)^{-1}$. The two states are split by an energy 2δ . Since the deformation constants a and b are negative, compressive strains make δ negative, which means that the HH band lies above the LH band (Fig. 1.)

The character of the bands becomes increasingly mixed with increasing k_x , [the wave-vector component in the (x,y) plane] with the effective mass in the (x,y) plane showing mass reversal. The extent of this mass reversal varies with direction in the plane, the magnitude of the anisotropy being determined by the difference between the Luttinger parameters γ_2 and γ_3 . In many cases this difference is small and it is often convenient and justified to take a spherical average and henceforth ignore such anisotropy. It is straightforward to show that

$$\langle k_x^2 k_y^2 + k_y^2 k_z^2 + k_z^2 k_x^2 \rangle = \frac{1}{3} k^4. \quad (8)$$

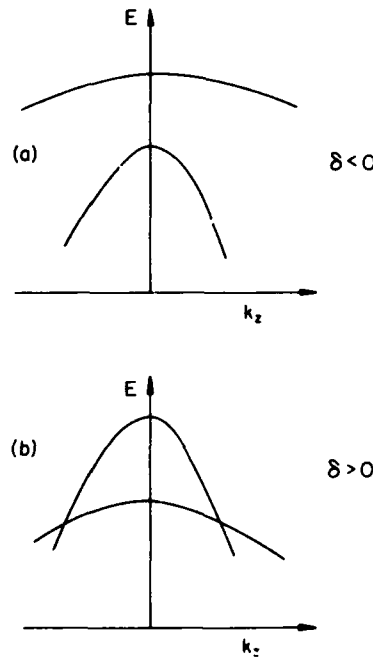


FIG. 1. Valence-band structure (schematic) for (a) compressional stress ($\delta < 0$), (b) tensional stress ($\delta > 0$). Note the possibility of degeneracy in the latter case.

Thus, in the spherical approximation, which we will adopt from now on,

$$E = E_0 + \frac{\hbar^2}{2m} [-\gamma_1 k_z^2 \pm (4\bar{\gamma}^2 k_z^4 + 2\bar{\gamma}(k_z^2 - 2k_z)K^2 + K^4)^{1/2}], \quad (9)$$

where

$$\bar{\gamma}^2 = (2\gamma_2^2 + 3\gamma_1^2)/5 \quad (10)$$

and we put $\gamma_2 = \gamma_1 = \bar{\gamma}$ elsewhere.

Introducing an interface means that we have to combine forward and backward traveling waves of the same parity on one side, and fit to evanescent functions on the other to obtain bound states conserving amplitude and current flow. If the potential is asymmetric, such as in the case of a single heterojunction, we must consider both spins separately, since spin degeneracy is not maintained when the system lacks a center of inversion symmetry. Here we will limit our discussion to the symmetric quantum-well case, so we need consider only one spin.

In choosing the combination of forward and backward traveling waves in the quantum well it is not merely a matter of reversing the sign of k_z , because more than one quantization of angular momentum is involved in general as a consequence of the mixed light-hole/heavy-hole character of the waves. A specular reflection is equivalent to a rotation in the (xy) plane followed by a space inversion. Rotation affects a state through the rotation operator

$$R_z = e^{-i\pi J_z}, \quad (11)$$

where J_z is the component of the total angular momentum along the z direction, which in our case takes on the values $\frac{1}{2}, -\frac{1}{2}, -\frac{3}{2}$. This causes the sign to oscillate according to $-1, +1, -1, +1$. Thus suitable wave functions for the quantum well are

$$H_1(\mathbf{k}, k_z) = \begin{vmatrix} R_1 \cos k_z z & & \\ -iL^* \sin k_z z & e^{i\mathbf{k} \cdot \mathbf{r}} & \\ -M^* \cos k_z z & & \\ 0 & & \end{vmatrix},$$

$$L_1(\mathbf{k}, k_z) = \begin{vmatrix} -L \cos k_z z & & \\ iR_2 \sin k_z z & e^{i\mathbf{k} \cdot \mathbf{r}} & \\ 0 & & \\ -M^* \sin k_z z & & \end{vmatrix}. \quad (12)$$

These two wave functions are degenerate at a particular energy E for wave vectors $k_z = k_H$ (say) for the HH band and $k_z = k_L$ for the LH band, so that, for $\mathbf{k} = 0$,

$$(\gamma_1 + 2\bar{\gamma})k_z^2 - K^2 = (\gamma_1 - 2\bar{\gamma})k_z^2 + K^2. \quad (13)$$

The envelope function inside the well is then a linear combination of the form

$$\Psi_{\text{well}} = AH_1(\mathbf{k}, k_H) + BH_1(\mathbf{k}, k_L) + CL_1(\mathbf{k}, k_H) + DL_1(\mathbf{k}, k_L). \quad (14)$$

Note that in the presence of strain k_H or k_L may be imaginary even though they are in the well. In the barrier we take a

similar linear combination, but, for bound states, k_H and k_L are both imaginary and V_0 , the barrier height, is added to the energy. The allowed energies are obtained by solving the 8×8 determinant.

For $\mathbf{k}_{\parallel} = 0$ the situation simplifies since $H_1(0, k_L) = 0$ and $L_1(0, k_H) = 0$, and we obtain from the boundary conditions at $z = \pm L/2$ the familiar conditions

$$\tan k_z L/2 = F$$

or

$$\cot k_z L/2 = -F, \quad (15)$$

$$F = [m_w^*(V_0 - E_Q)/m_B^*E_Q]^{1/2},$$

where $k_z = k_H$ or k_L , m_w^* and m_B^* are the z -direction effective masses in the well and barrier, respectively, and E_Q is the quantum confinement energy, which is the kinetic energy of the hole measured from the bottom of the quantum well. But when $\mathbf{k}_{\parallel} \neq 0$ we are back to our 8×8 determinant.

III. SIMPLE MODEL

There is one case where an analytic solution can be found, namely, when the well is infinitely deep. In this case the wavefunction vanishes at $z = L/2$ and there is no current to conserve. As a result the 8×8 determinant reduces to a 4×4 determinant. Working this out gives the following equation:

$$[E^2 + E(P_H + P_L) + P_H P_L - Q_H Q_L - MM^*] \times \sin k_H L \sin k_L L - 12(\hbar^2/2m)^2 \bar{\gamma}^2 k_{\parallel}^2 k_H k_L \\ \times (1 - \cos k_H L \cos k_L L) = 0, \quad (16)$$

where P_H, P_L and Q_H, Q_L are given in Eq. (16) with $k_z = k_H, k_L$. (In the spherical approximation we replace γ_3 by $-\gamma$.) When $\mathbf{k}_{\parallel} = 0$ the solution is

$$k_H L = n\pi \quad \text{or} \quad k_L L = n\pi, \quad (17)$$

where n is a nonzero integer. However, we note that k_H (and k_L) deviates from the familiar condition of Eq. (17) when $\mathbf{k}_{\parallel} \neq 0$. The quantized wave function in the confinement direction is thus dependent on \mathbf{k}_{\parallel} . Reference to Eq. (9) shows that the change of energy with k_{\parallel} then arises from terms directly dependent on k_{\parallel} plus a contribution from the variation of the confinement energy (i.e., k_z^2) on k_{\parallel} . Both of these contributions combine to determine the in-plane effective mass.

When k_{\parallel} is small, specifically when

$$k_z^2 \ll k_{\parallel}^2 \quad (2\bar{\gamma}k_z^2 - K^2), \quad (18)$$

Eq. (16) becomes, in the spherical approximation,

$$2k_H k_L (1 - S_H)(1 - S_L) \sin k_H L \sin k_L L \\ + 3k_{\parallel}^2 (1 - \cos k_H L \cos k_L L) = 0, \quad (19)$$

where we have introduced the dimensionless quantities S_H, S_L , viz.

$$S_H = K^2/2\bar{\gamma}k_H^2, \quad S_L = K^2/2\bar{\gamma}k_L^2. \quad (20)$$

These strain ratios measure the strength of the strain relative to the strength of the confinement. Putting $k_H = k_{H0} + \Delta k_H$, $\Delta k_H \ll k_{H0}$, where $k_{H0}L = n\pi$, we can determine the variation of the heavy-hole confinement wave vector

with k_H, k_L being given by Eq. (13). We can also perform a similar calculation for the light-hole band. We find that Δk_H is simply proportional to k^2 . Consequently, if we expand Eq. (9) to first order in k^2 an in-plane effective mass for the HH band can be defined for the n th subband as follows:

$$\frac{m}{m^* (\text{HH})} = (\gamma_1 - \eta_H \bar{\gamma}) + \frac{3(\gamma_1 - 2\bar{\gamma}) [\cos k_L L + (-1)^{n+1}]}{(1 - S_H)(1 - S_L) k_L L \sin k_L L}, \quad (21)$$

with k_L (and hence S_L) determined by Eq. (13) when $k_H = n\pi/L$, and

$$\eta_H = (2 + S_H)/(1 - S_H). \quad (22)$$

Note that there are two contributions on the right-hand side of Eq. (21) which we may term the splitting component and the confinement component. Similarly, for the LH band,

$$\frac{m}{m^* (\text{LH})} = (\gamma_1 + \eta_L \bar{\gamma}) + \frac{3(\gamma_1 + 2\bar{\gamma}) [\cos k_H L + (-1)^{n+1}]}{(1 - S_H)(1 - S_L) k_H L \sin k_H L}, \quad (23)$$

with k_H (and hence S_H) determined by Eq. (13) when $k_L = n\pi/L$, and

$$\eta_L = (2 + S_L)/(1 - S_L). \quad (24)$$

When the strain is zero these expressions reduce to those of Nedorezov.¹¹

Equations (21)–(24) are valid provided S_H or $S_L \neq 1$. When $S_H = 1$ it turns out [see Eq. (13)] that $k_H = k_L$, and $S_L = 1$ also. This situation can happen only for positive strain energies, corresponding to lattice tension, when the LH band is above the HH band and they cross in the confinement (z) direction at $k_H = k_L = n\pi/L$, independent of k according to Eq. (19). Solving Eq. (9) in this case for small k gives

$$E = (\hbar^2/2m) [-\gamma_1(k_H^2 + k^2) \pm 2k_H k_L \bar{\gamma} \sqrt{3}]. \quad (25)$$

It should be noted that special cases occur for all LH and HH subband degeneracies, i.e., when $k_H = n_1\pi/L$, $k_L = n_2\pi/L$ correspond to the same energy. Whenever these occur, Eqs. (21) and (23) are no longer valid. A description in these cases is straightforward to obtain, but we will not pursue the topic of subband degeneracies further.

The big drawback to the model as it stands is its dependence on the assumption of an infinitely deep well, which is known to lead to a very poor estimate of subband energy in real cases. It turns out, however, that the in-plane mass is very insensitive to well width in the infinitely deep well model, the variations in the splitting and confinement components tending to cancel one another out. This encourages the assumption that the mass is not sensitive to the details of the confinement and hence we can use the infinite-well model to give us an estimate of the zone-center mass. In order to do this we adopt an "equivalent infinitely deep well" (EIW) model. In this we obtain, say for the HH confinement, k_H by

solving the correct boundary conditions with $k_L = 0$ via Eq. (15), and hence define S_H . We then take the confinement contribution to the in-plane effective mass to be the same as in the case of an infinitely deep well of width L^* such that $k_H L^* = n\pi$. This means that we can use Eq. (21) with $L = L^*$ and $k_L L^*$ determined from Eq. (13) with $k_H L^* = n\pi$. Effectively we are lumping all the effects due to the portions of the 8×8 determinant which were zero in the derivation of Eq. (16) into the effective well width L^* . This procedure uses the correct confinement energy and hence preserves the correct ratio of strain to confinement strengths and uses the infinite-well model to estimate the confinement contribution to the effective mass.

It is also useful to determine the degree of nonparabolicity and this, too, can be done in the EIW model (though the algebra is somewhat tedious). We define a nonparabolicity factor α as follows:

$$\hbar^2 k^2 / 2m^* = E (1 + \alpha E), \quad (26)$$

where E is the in-plane kinetic energy. To obtain α we expand k_H and k_L as follows:

$$k_H^2 = k_{H0}^2 + a k^2 + (b/k_{H0}^2) k^4$$

and

$$k_L^2 = k_{L0}^2 + c k^2 + (d/k_{L0}^2) k^4 \quad (27)$$

in Eqs. (9) and (16). Here a, b, c , and d are coefficients to be determined (not to be confused with deformation potentials, etc., used earlier!). We obtain for a HH band:

$$\alpha = \alpha_1 + \alpha_2,$$

$$\alpha_1 = -\left(\frac{m^*}{m}\right)^2 \frac{3\bar{\gamma}^2 S_H [4 - S_H + 4a(1 - S_H)]}{2\delta(1 - S_H)^3},$$

$$\alpha_2 = -\left(\frac{m^*}{m}\right)^2 \frac{(\gamma_1 - 2\bar{\gamma})^2 b}{E_{H0}}, \quad (28)$$

where

$$a = -\frac{3[\cos k_{L0} L^* + (-1)^{n+1}]}{(1 - S_H)(1 - S_L) k_{L0} L^* \sin k_{L0} L^*}, \quad (29)$$

$$k_{L0} L^* = \frac{[\gamma_1 - 2\bar{\gamma}(1 - 2S_H)]}{\gamma_1 + 2\bar{\gamma}} n^2 \pi^2, \quad (30)$$

$$E_{H0} = (\hbar^2/2m)(\gamma_1 - 2\bar{\gamma}) k_{H0}^2, \quad (31)$$

$$b = (e - f \cot k_{L0} L^*)/g, \quad (32)$$

In the expression for b , we have

$$e \approx a^2 k_{L0}^2 L^* (1 - S_H)(1 - S_L)$$

$$\approx a [k_{L0}^2 L^* (1 - S_L)(4a - 1 + \eta_H) + n^2 \pi^2 (1 - S_H)(4c - 1 + \eta_L)] - 6n^2 \pi^2 c, \quad (33)$$

$$f = 2acn\pi k_{L0} L^* (1 - S_H)(1 - S_L),$$

$$g = 4k_{L0}^2 L^* (1 - S_H)(1 - S_L).$$

Since k_L is chosen to give the same energy as k_H the factors a and c are related, viz.,

$$c = \left(\frac{\gamma_1 - 2\bar{\gamma}}{\gamma_1 + 2\bar{\gamma}}\right) a = \left(\frac{\gamma_1 - 2\bar{\gamma}}{\gamma_1 + 2\bar{\gamma}}\right) (\eta_H + \eta_L) \quad (34)$$

For a LH band we interchange S_H and S_L , a and c , k_H , and

TABLE I. Parameters for GaAs and InAs. $E_g(300 \text{ K}) = 1.43 - 1.53x + 0.45x^2$.

	Ξ_d	a	b	E_g	c_{11}	c_{12}	a_s
	(eV)			$(10^{11} \text{ dyn cm}^{-1})$			(Å)
GaAs	+ 7.0	- 2.0	- 1.7	1.43	11.88	5.38	5.6533
InAs	+ 4.7 ^a	- 1.3 ^a	- 1.7	0.35	8.33	4.53	6.0584
	γ_1	γ_2	γ_3	γ	m_h^*/m	m_l^*/m	m_l^*/m
GaAs	6.85	2.10	2.90	2.61	0.613 ^b	0.0829 ^b	0.067
InAs	20.5	8.37	9.29	8.93	0.379 ^b	0.0261 ^b	0.027

^a Derives from $\Xi_d - a = 6 \text{ eV}$ and $\Delta E_c / \Delta E_v = \Xi_d / a = 7.2$.

^b Derived from the Luttinger parameters in the spherical approximation.

k_{L0} , and change the sign of $\bar{\gamma}$ and the strain energy δ in Eqs. (28) – (33).

These expressions yield the correct result of vanishing nonparabolicity when either $\bar{\gamma}$ approaches zero or the strain splitting energy is large and negative (compression). Taken with the expressions for zone-center mass [Eqs. (21) and (23)] they provide a complete analytical description of the band structure near the zone center, which is applicable to arbitrary well depths and widths within the EIW approximation and is exact for infinitely deep wells.

It is time to summarize the discussion of this section. A study in the case of an infinitely deep well shows that the in-plane effective mass near the zone center is determined by two components, one depending on the splitting of the HH and LH bands brought about by strain but modified by quantum confinement, the other depending on how the confine-

ment changes with in-plane motion. These components quantify the degree of HH-LH mixing out from the zone center. In the case of a well of finite depth the confinement energies can be determined simply only at the zone center. However, provided the splitting and confinement components of the mass are close to those for an infinitely deep well—which the independence of mass on well width suggests is true—an EIW model can be used to determine the zone-center mass and how it varies away from the zone center.

IV. APPLICATION TO $\text{In}_x\text{Ga}_{1-x}\text{As}/\text{GaAs}$ QUANTUM WELLS

We have applied these ideas to the system $\text{In}_x\text{Ga}_{1-x}\text{As}/\text{GaAs}$. The parameters¹² used in the calculation are given in Table I. The extrapolations between GaAs and InAs were all assumed to be linear except for the band gap. The distribution of band-edge discontinuities arising from alloying was taken to be the same as obtained from the GaAs dilatational deformation constants, viz., 77% for the conduction band. Figure 2 shows the variation of subband energies at $k = 0$ and overall band gap (E_1 to $HH1$) with indium composition up to 40% assuming a 50-Å well. Note that the LH band drops below the GaAs valence-band edge implying that light holes are unconfined. The system is type I for heavy holes but type II for light holes. (This will not be the case if the interaction with the split-off band is strong.)

The dependence of subband structure on well width for $x = 0.3$ is shown in Fig. 3. For $L = 50 \text{ \AA}$ there is only one electron subband and two HH subbands. Figure 4 depicts the variation of in-plane mass with composition and with

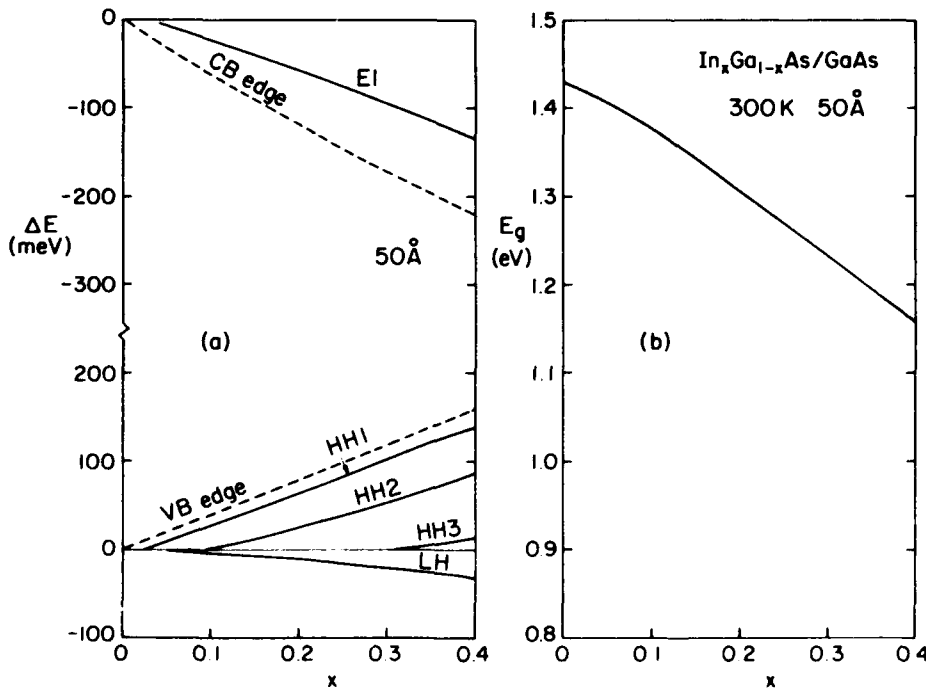


FIG. 2. Energy levels as a function of indium composition (x) for a 50-Å $\text{In}_x\text{Ga}_{1-x}\text{As}/\text{GaAs}$ quantum well. (a) Subband levels and band edges; (b) energy gap ($E_1 - HH1$).

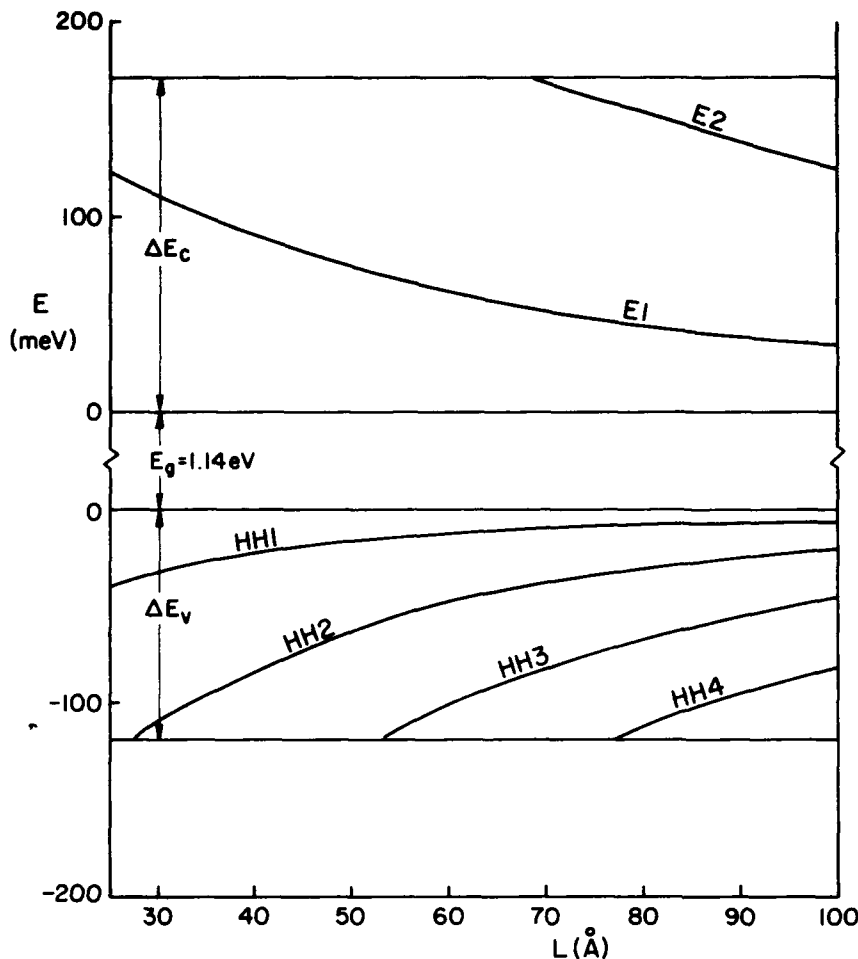


FIG. 3. Subband structure as a function of well width for $x = 0.3$. The discontinuities in the conduction-band (ΔE_c) and valence-band (ΔE_v) edges are also shown.

well-width calculated using Eq. (21) with the equivalent infinitely deep well approximation. This shows that the zone-center mass remains remarkably constant with varying well width for the odd-numbered subbands. Figure 5 shows the dependence of the non-parabolicity factor on x and L .

It is interesting to compare these results with the experi-

mental results obtained from a study of magnetoluminescence by Jones *et al.*¹³ The comparison is shown in Table II. We have used a 7:2 ratio for the band offsets. The energy gaps differ by 3.5%, 1.7%, and 1.7%, respectively, for the three samples, which is a very reasonable agreement. Apart from the case of the sample with 25% In the masses exhibit

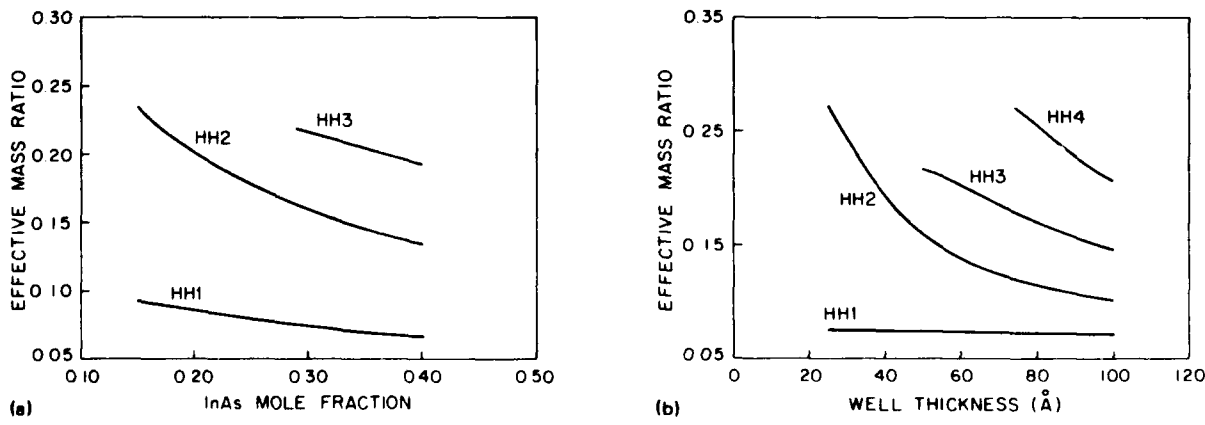
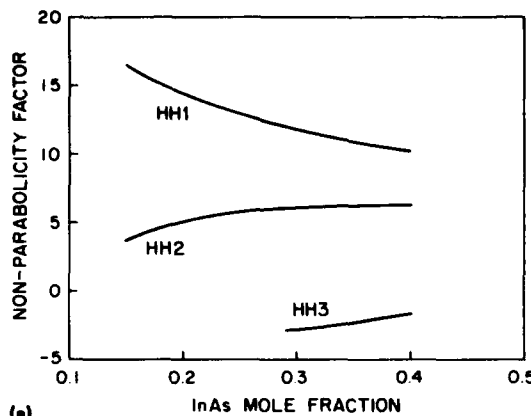


FIG. 4. Variation of zone-center effective mass with (a) composition for a 50-Å well and (b) well width for $x = 0.3$.



(a) InAs MOLE FRACTION

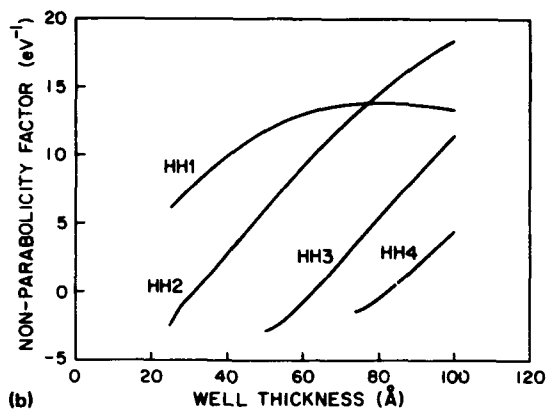


FIG. 5. Dependence of the nonparabolicity factor α on (a) composition for a 50-Å well and (b) well width for $x = 0.3$.

TABLE II. Comparison of EIW predictions with experiment.

Specimen	In %	L (Å)	E_c (meV)		$m^*(HH)/m$		α (eV) ⁻¹	
			Expt.	Theor.	Expt. (± 8%)	Theor.	Expt. (± 20%)	Theor.
AK242	15	125	1388.1	1340	0.084	0.088	53.3	22.4
BC042	20	80	1326.2	1304	0.086	0.084	29.8	18.3
TO195	25	90	1288.3	1266	0.094	0.077	18.1	15.7

excellent agreement. Comparison with the experimental nonparabolicity factors shows only rough agreement—better for higher In contents—but the same trend is exhibited. Overall, the comparison suggests that the EIW model is a good one.

V. CONCLUSIONS

We conclude that a relatively simple analytic model for the valence-band structure can provide a reasonably sound basis for calculating parameters of direct relevance to quantum-well lasers and other devices. The model is applicable for arbitrary strains and arbitrary quantum confinement except where “accidental” light-hole/heavy-hole degeneracies occur.

ACKNOWLEDGMENTS

I would like to thank Professor Lester Eastman for providing the opportunity to visit Cornell. I have benefited from discussions with him, Bill Schaff, Luke Lester, and Pierre Mandeville. I am particularly indebted to Luke Lester for his invaluable assistance with some of the calculations. This work is partially supported by the Army Research Office

under Contract No. DAAL03-89-K-0006 and the Office of Naval Research.

- ¹ G. E. Pikus and G. L. Bir, Sov. Phys.—Solid State **1**, 1502 (1959).
- ² B. K. Ridley and T. B. Watkins, Proc. Phys. Soc. **78**, 293 (1961).
- ³ G. C. Osbourn, P. M. Biefeld, and P. L. Gourley, Appl. Phys. Lett. **41**, 172 (1982).
- ⁴ A. R. Adams, Electron. Lett. **22**, 249 (1986).
- ⁵ For reviews of the subject see, for example: G. Bastard and J. A. Brum, IEEE J. Quantum Electron. **QE-22**, 1625 (1986); E. Yablonovitch and E. O. Kane, J. Lightwave Technol. **6**, 1292 (1988); and E. P. O'Reilly, Semicond. Sci. Technol. **4**, 121 (1989).
- ⁶ J. M. Luttinger and W. Kohn, Phys. Rev. **97**, 869 (1955).
- ⁷ J. M. Luttinger, Phys. Rev. **102**, 1030 (1956).
- ⁸ M. Altarelli, *Heterojunctions and Semiconductor Superlattices*, edited by G. Allan, G. Bastard, N. Boccara, M. Lannoo, and M. Voos (Springer, Berlin, 1986), p. 12; J. M. Marzin, *ibid.*, p. 161.
- ⁹ D. L. Smith and C. Mailhiot, J. Appl. Phys. **63**, 2717 (1988).
- ¹⁰ L. C. Andreani, A. Pasquarello, and F. Bassani, Phys. Rev. B **36**, 5887 (1987).
- ¹¹ S. S. Nedorezov, Sov. Phys.—Solid State **12**, 1814 (1971).
- ¹² Landolt-Bornstein, *New Series Group III* (Springer, Berlin, 1982), Vol. 17a.
- ¹³ E. D. Jones, S. K. Lyo, I. J. Fritz, J. F. Klem, J. E. Schirber, C. P. Tigges, and T. J. Drummond, Appl. Phys. Lett. **54**, 2227 (1989).

Free optical vibrations of an infinite plate of homogeneous isotropic elastic matter

B. K. Ridley*

School of Electrical Engineering, Phillips Hall, Cornell University, Ithaca, New York 14852-5401

(Received 4 March 1991)

We adapt the standard theory of the free acoustic vibrations of an infinite plate of homogeneous isotropic elastic matter to the corresponding case of optical vibrations. Treating nonpolar material first, we show that the effect of the free surface is to couple LO and TO modes, and we demonstrate the existence of the optical analog of Rayleigh waves. Interface and guided modes are both present, and their respective mode patterns are derived. In polar materials the coupling between LO and TO is different because of the frequency splitting due to the ionic fields, but surface modes are still present. This result contradicts the conclusion of the hydrodynamic model that surface modes do not exist. The polar character also allows the existence of surface polaritons. It is shown that the standard description of these modes, which neglects the elastic properties of the material, is physically invalid. The effect of the free surface is to couple surface polaritons and LO modes, and a description is given of the mode patterns that may occur. General expressions for energy flux are given, and boundary conditions for the general case are suggested. This treatment goes some way towards reconciling the various theoretical models of phonon confinement that have been advanced recently.

I. INTRODUCTION

A description of the free acoustic vibrations of an infinite plate of homogeneous isotropic elastic matter has been available for over a century,¹ but a corresponding description for optical vibrations has not been given, to the author's knowledge. Here we report such a description for nonpolar material, and subsequently for polar material. The motivation was to establish a consistent account of longitudinally polarized (LO) and transversely polarized (TO) optical modes in a thin layer treated as an isotropic elastic and dielectric continuum to act as a basis for calculating the electron-phonon and hole-phonon scattering rates in layered semiconductors. Here we limit attention to the free-standing plate since this is the simplest system that illustrates the basic physics. The latter emerges in the form of an unavoidable coupling of LO and TO modes brought about by the presence of a surface. Such a coupling between acoustic modes (LA and TA) is well known, but its significance for optical modes has not been widely appreciated hitherto.

Models of confined optical modes which are currently in the literature achieve differing levels of sophistication. The earliest and simplest was the dielectric-continuum (DC) model in which only electrical boundary conditions were used to determine LO mode patterns.^{2,3} Such a model, clearly, could not describe confinement in nonpolar material, and it soon came into serious conflict with the predictions of linear chain models⁴ through its lack of boundary conditions, which referred to mechanized stability. A more successful, but still overly simple, model described LO confinement using hydrodynamic (HD) boundary conditions,⁵ in which it was argued that since an LO mode was characterized by zero electric displacement it contained no electromagnetic energy, and so only purely mechanical conditions had to be satisfied at a

boundary. The HD model showed much closer agreement with linear chain models, though it was soon pointed out that HD boundary conditions were not strictly consistent with the actual ionic motion at the interface.⁶ Nevertheless, the HD model displayed the twin virtues of conserving energy and establishing mechanical stability through its expansion of the Born-Huang model to include dispersion. On the other side of the balance sheet, it displayed the perceived defect of allowing tangential electric fields, and with them, the scalar potential, to be discontinuous at the interface.

As three-dimensional models of the lattice dynamics—usually referred to as microscopic (*M*) models—became more sophisticated, two aspects emerged. One was the primacy of mechanical conditions, and the other was the added complexity introduced by the elastic anisotropy of the crystals considered (mostly GaAs and AlAs). Huang and Zhu attempted to reconcile the DC and *M* models by *ad hoc* addition of scalar potentials so both electric and mechanical boundary conditions were satisfied, and by a reinterpretation of off-axis modes. Bechstedt and Gerecke⁷ attempted a similar reconciliation. Both pairs of workers obtained a hybridization of LO guided modes with Fuchs-Kliewer⁸ (FK) surface polaritons. The additions conceived by Huang and Zhu, besides being *ad hoc*, destroyed the orthogonality of the modes, but this has been rectified recently by Haupt and Wendler¹⁰ who have gone on to calculate electron-phonon scattering rates. Some unsatisfactory elements in all of these approaches have been pointed out recently.¹¹

A continuum theory of confined optical modes should be able to stand on its own and be internally self-consistent. It should also be applicable to nonpolar and polar materials. Only when these criteria are satisfied can a judgment be made concerning the validity of apply-

ing it to a real system composed of atoms. The HD model satisfies these criteria by limiting itself strictly to LO modes and seeing any discontinuity of the scalar potential that may arise as resolvable only on an atomic scale. The models mentioned above start from the basis of the DC model, which is clearly not self-consistent. In what follows we develop a continuum model that goes beyond the HD model in that it treats TO modes and the LO-TO interaction and which rediscovered the HD model as a special case. It bases itself on the firmly established theory of elasticity.

Our approach is straightforward. We first identify the dispersion of optical modes with the macroscopic elastic properties of the material. This immediately allows us to take over the theory established for acoustic modes in nonpolar material and apply it to optical modes. In doing so we discover the optical-mode analog of Rayleigh waves. The transition to polar material is effected simply by taking into account the splitting of LO and TO frequencies and introducing a new mode — the surface polariton. Throughout, we assume that the medium is elastically isotropic, which allows us to keep LO and TO modes distinct and allows us to orientate Cartesian axes irrespective of crystallographic direction. We take the x axis parallel to the direction of propagation in the plane of the plate and the z axis to be perpendicular to the plane of the plate. Modes with displacements in the plane of incidence (xz) are the LO mode and the p -polarized TO mode (or just p -TO); the mode with dis-

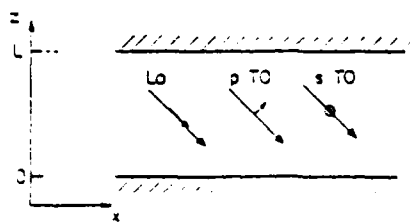


FIG. 1. Coordinate system and mode designation. Depicted are the propagation and polarization directions of the plane-wave components that together with their reflections make up waves with a standing component in the z -direction, which propagate along the x axis.

placement at right angles to the plane of incidence (i.e., along the y direction) is the s -polarized TO mode (or s -TO) (Fig. 1).

II. OPTICAL PHONONS

The dispersion relation for long-wavelength optical phonons in nonpolar material can be written as follows:

$$(\omega^2 - \omega_0^2)u(\mathbf{k}) = -H(\mathbf{k})u(\mathbf{k}), \quad (1)$$

where

$$H(\mathbf{k}) = \begin{bmatrix} Ak_x^2 + B(k_y^2 + k_z^2) & Ck_xk_y & Ck_xk_z \\ Ck_yk_x & Ak_y^2 + B(k_x^2 + k_z^2) & Ck_yk_z \\ Ck_zk_x & Ck_zk_y & Ak_z^2 + B(k_x^2 + k_y^2) \end{bmatrix} \quad (2)$$

is a 3×3 matrix, $u(\mathbf{k})$ is the relative displacement, and ω_0 is the frequency at $\mathbf{k} = 0$. We take $H(\mathbf{k})$ to be identical to the matrix for acoustic modes, from which it follows that

$$\begin{aligned} A &= v_L^2 = c_{11}/\rho, \quad B = v_T^2 = c_{44}/\rho, \\ C &= (c_{12} + c_{44})/\rho, \end{aligned} \quad (3)$$

where v_L , v_T are the velocities of LA and TA modes, c_{11} , etc. are the elastic constants, and ρ is the mass density. Thus the dispersion relations for LO and TO modes are

$$\begin{aligned} \omega^2 &= \omega_0^2 - v_L^2 k^2 \text{ LO} \\ &= \omega_0^2 - v_T^2 k^2 \text{ TO (s and } p\text{).} \end{aligned} \quad (4)$$

where $k^2 = k_x^2 + k_y^2 + k_z^2$ for all directions provided the material is elastically isotropic, viz.,

$$c_{11} - c_{12} - 2c_{44} = 0. \quad (5)$$

We will assume this to be the case.

Dispersion arises as a consequence of the elastic stresses produced by a traveling optical wave. The

equivalent strains are given by

$$\begin{aligned} S_1 &= -\frac{\partial u_x}{\partial x}, \quad S_2 = -\frac{\partial u_y}{\partial y}, \quad S_3 = -\frac{\partial u_z}{\partial z}, \\ S_4 &= -\frac{1}{2} \left(\frac{\partial u_z}{\partial y} + \frac{\partial u_y}{\partial z} \right), \end{aligned} \quad (6)$$

$$\begin{aligned} S_5 &= -\frac{1}{2} \left(\frac{\partial u_z}{\partial x} + \frac{\partial u_x}{\partial z} \right), \\ S_6 &= -\frac{1}{2} \left(\frac{\partial u_y}{\partial x} + \frac{\partial u_x}{\partial y} \right). \end{aligned}$$

The minus signs arise as a consequence of the out-of-phase vibration of the two atoms in the unit cell. The stresses are given by the usual set of equations:

$$\begin{aligned}
 T_1 &= c_{11}S_1 + c_{12}(S_2 + S_3), \\
 T_2 &= c_{11}S_2 + c_{12}(S_3 - S_1), \\
 T_3 &= c_{11}S_3 + c_{12}(S_1 + S_2), \\
 T_4 &= 2c_{14}S_4, \\
 T_5 &= 2c_{14}S_5, \\
 T_6 &= 2c_{14}S_6.
 \end{aligned} \tag{7}$$

Equations (6) and (7) allow us to calculate dilatational and shear stresses produced by a travelling optical wave.

The assumption of isotropy allows us to decompose any displacement u into a longitudinally polarized part u_L and a transversely polarized part u_T

$$u = u_L + u_T \tag{8}$$

with u_L and u_T defined by¹²

$$\begin{aligned}
 \nabla \times u_L &= 0, \\
 \nabla \cdot u_T &= 0.
 \end{aligned} \tag{9}$$

Of course, u_L and u_T must have the same time dependence, i.e. the same frequency.

III. NONPOLAR MATERIAL

The boundary condition which must be satisfied when the surface is free is that the dilatational stress perpendicular to the surface and shear stress across the surface vanish. The situation is simplest for s -polarized TO modes. A solution is

$$u_y = e^{ik_L z} (A e^{ik_T z} + B e^{-ik_T z}), \tag{10}$$

which satisfies $\nabla \cdot u = 0$. It must also satisfy

$$T_3 = 0, \quad T_4 = 0, \quad T_5 = 0 \tag{11}$$

at $z = 0$ and $z = L$. For this wave the stresses T_3 and T_5 are zero everywhere. To obtain $T_4 = 0$ we must have

$$u_y = e^{ik_L z} \cos k_L z, \quad k_L L = n \pi, \tag{12}$$

where n is an integer. In this case no mixing with other modes is required.

The surface couples LO and p -polarized TO modes. Thus we take

$$\begin{aligned}
 u_x &= k_x e^{ik_L z} (A e^{ik_T z} + B e^{-ik_T z}) \\
 &\quad - k_T e^{ik_T z} (C e^{ik_T z} + D e^{-ik_T z}), \\
 u_z &= k_L e^{ik_L z} (A e^{ik_T z} - B e^{-ik_T z}) \\
 &\quad - k_x e^{ik_T z} (C e^{ik_T z} - D e^{-ik_T z}).
 \end{aligned} \tag{13}$$

We distinguish the z components of the LO and TO wave vectors k_L and k_T , respectively. Equation (9) is satisfied for the individual LO and TO components, and it is clear that the condition $T_4 = 0$ holds everywhere. The wave-vector component along the surface must be common to both components. They must also have the same frequency, from which (Fig. 2)

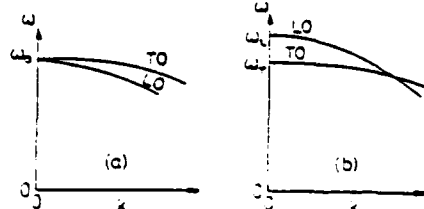


FIG. 2. Schematic dispersion relationship of (a) nonpolar and (b) polar material.

$$\omega^2 = \omega_0^2 - v_L^2(k_x^2 + k_L^2) = \omega_0^2 - v_T^2(k_x^2 + k_T^2). \tag{14}$$

It is convenient to define a "plate" velocity v and a parameter s such that

$$\omega_0^2 - \omega^2 = v^2 k_x^2 \quad \text{and} \quad s = v^2 / v_T^2, \tag{15}$$

from which

$$k_L^2 = (\gamma s - 1) k_x^2, \quad k_T^2 = (s - 1) k_x^2, \tag{16}$$

$$\text{where } \gamma = v_T^2 / v_L^2 = c_{14} / c_{11}.$$

As indicated in the Appendix, the boundary conditions can be satisfied provided the following equation is true:

$$\begin{aligned}
 (qr - pr)^2 \sin k_L L \sin k_T L \\
 - 2qrpt[\cos(k_L - k_T)L - 1] = 0,
 \end{aligned} \tag{17}$$

where

$$\begin{aligned}
 p &= \gamma(s-2), \quad q = 2\gamma\sqrt{s-1}, \\
 r &= 2\sqrt{\gamma s - 1}, \quad t = s-2.
 \end{aligned} \tag{18}$$

This admits of two waves. One is a guided mode consisting of coupled phased-matched LO and TO waves, the other is a surface mode consisting of coupled evanescent LO and TO waves. The latter is the optical analog of the Rayleigh wave in acoustics. Some mode patterns are described below.

A. Guided modes

These waves have phase-matched components with the following wave vectors:

$$k_L L = n_L \pi, \quad k_T L = n_T \pi, \quad n_T - n_L = 2m, \tag{19}$$

where n_L , n_T , and m are all integers. The displacement in the z direction can be described by sine or cosine. The sine solution is

$$\begin{aligned}
 u_x &= 2A e^{ik_L z} \left[k_L \cos k_L z - k_T \frac{p}{q} \cos k_T z \right], \\
 u_z &= 2iA e^{ik_L z} \left[k_L \sin k_L z - k_T \frac{p}{q} \sin k_T z \right],
 \end{aligned} \tag{20}$$

and the cosine solution is

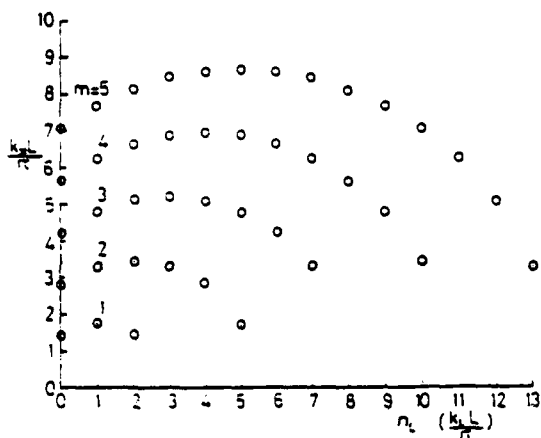


FIG. 3. Relation between k_L and k_x for guided modes in nonpolar material with $\gamma = \frac{1}{3}$. L is the width of the plate and $2m = n_T - n_L$ ($n_L = k_L L / \pi$, $n_T = k_T L / \pi$).

$$u_x = 2iAe^{ik_x x} \left[k_x \sin k_L z - k_T \frac{r}{t} \sin k_T z \right], \quad (21)$$

$$u_z = 2Ae^{ik_x x} \left[k_L \cos k_L z - k_x \frac{r}{t} \cos k_T z \right].$$

Figure 3 shows the relationship between k_L and k_x when $\gamma = \frac{1}{3}$. The spectrum can be seen as consisting of branches defined by the integer m . Figure 4 depicts the corresponding dispersion. All branches are associated with a velocity factor $s = 3$, corresponding to a velocity v close to v_L . Note that the choice of γ ($= c_{44}/c_{11}$) to be one-third in these examples is reasonable in view of the actual ratios of elastic constants found among semiconductors.

These guided waves are a profound hybridization of

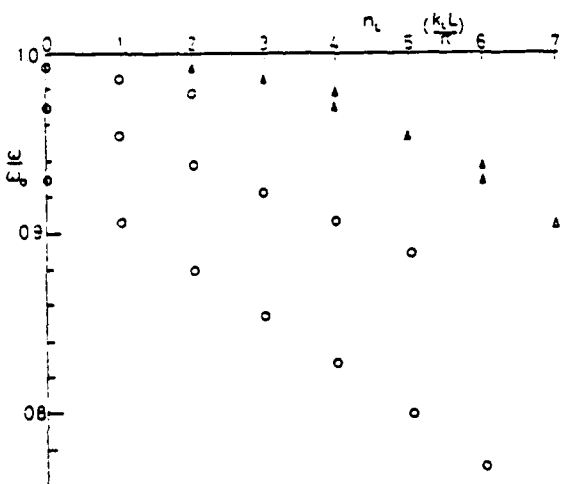


FIG. 4. Dispersion for guided modes in nonpolar material with $\gamma = \frac{1}{3}$ and $\omega_0 L / v_T \pi = 20$. (○ LO modes; △ TO modes.) ($n_L = k_L L / \pi$)

LO and TO modes, which arises because their frequencies lie close together. The frequency of the TO mode is the higher as a consequence of the smaller velocity of TA modes. One consequence of this is that the smallest TO vector component in the z direction that is allowed is one where $n_L = 1$ and $n_T = 3$, to satisfy Eq. (19). Confinement eliminates $n_T = 1$ and $n_T = 2$.

B. Surface modes

No surface-wave solutions exist for s -polarized TO modes, but Eq. (17) allows both k_L and k_T to be imaginary. For brevity we quote mode patterns only for $L \rightarrow \infty$ and $L \rightarrow 0$, since simple expressions are obtained in these limits.

For $L \rightarrow \infty$, the antisymmetric solution is, with $k_L = i\alpha_L$ and $k_T = i\alpha_T$,

$$u_x = 2Ae^{ik_x x} \left[k_x e^{-\alpha_L L/2} \cosh \alpha_L (z - L/2) + i\alpha_T \frac{r}{q} e^{-\alpha_T L/2} \cosh \alpha_T (z - L/2) \right], \quad (22)$$

$$u_z = 2Ae^{ik_x x} \left[-i\alpha_L e^{-\alpha_L L/2} \sinh \alpha_L (z - L/2) + k_L \frac{r}{q} e^{-\alpha_T L/2} \sinh \alpha_T (z - L/2) \right]$$

and the symmetric solution is

$$u_x = 2Ae^{ik_x x} \left[-k_x e^{-\alpha_L L/2} \sinh \alpha_L (z - L/2) - i\alpha_T \frac{r}{q} e^{-\alpha_T L/2} \sinh \alpha_T (z - L/2) \right], \quad (23)$$

$$u_z = 2Ae^{ik_x x} \left[i\alpha_L e^{-\alpha_L L/2} \cosh \alpha_L (z - L/2) - k_x \frac{r}{q} e^{-\alpha_T L/2} \cosh \alpha_T (z - L/2) \right].$$

In this limit Eq. (17) reduces to

$$qr + pt = 0, \quad (24)$$

which leads to a cubic equation for s , the velocity factor, viz.,

$$s^3 - 8s^2 + 8(3 - 2\gamma)s - 16(1 - \gamma) = 0. \quad (25)$$

This equation is just that found in the theory of Rayleigh waves.¹²

With $\gamma = \frac{1}{3}$ this reduces to

$$(s - 4)(3s^2 - 12s + 8) = 0. \quad (26)$$

The solutions are, therefore,

$$s = 4, \quad s = 2 \left[1 + \frac{1}{\sqrt{3}} \right], \quad s = 2 \left[1 - \frac{1}{\sqrt{3}} \right]. \quad (27)$$

Only the last is consistent with having k_L and k_T imaginary. We thus obtain the relationship between α_L , α_T , and k_x , viz.,

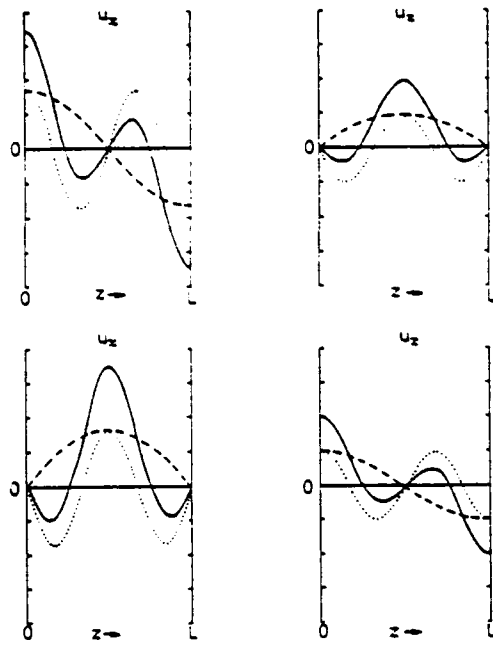


FIG. 5. Mode patterns for $n_L = 1, n_T = 3$ in nonpolar material. (Dashed line, LO; dotted line, TO; continuous line, LO - TO.)

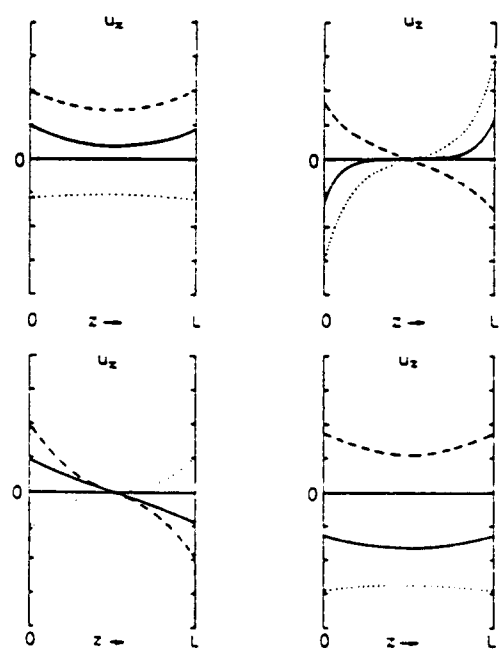


FIG. 6. Mode patterns for surface waves in nonpolar material (designations as in Fig. 5).

$$\alpha_L = \left[\frac{1}{3} \left(1 + \frac{2}{\sqrt{3}} \right) \right]^{1/2} k_x, \quad (28)$$

$$\alpha_T = \left[\frac{2}{\sqrt{3}} - 1 \right]^{1/2} k_x.$$

Note that the LO component drops off from the surface more rapidly than does the TO component.

For $L \rightarrow 0$ only the antisymmetric mode survives, the mode pattern being that of Eq. (22) with $\exp(-\alpha_T L/2) = 1$. In this case we find

$$s = 2(1 - 2\gamma), \quad (29)$$

from which

$$\alpha_L = (1 - 2\gamma + 4\gamma^2)^{1/2}, \quad \alpha_T = (4\gamma - 1)^{1/2} k_x. \quad (30)$$

This completes our description of the allowed modes of a nonpolar plate. A depiction of mode patterns is given in Figs. 5 and 6.

IV. POLAR MATERIAL

When the two atoms in the unit cell are oppositely charged their oscillations are accompanied by long-range electric fields that modify the elastic restoring forces and alter the frequencies of LO and TO modes. The dispersion relation for long-wavelength optical modes becomes modified along the following lines:

$$(\omega_L^2 - \omega_T^2)u(k) = [-H(k) - (\omega_L^2 - \omega_T^2)I(k)]u(k), \quad (31)$$

where ω_L, ω_T are the LO and TO zone-center frequencies, and

$$I(k) = \frac{1}{k^2} \begin{vmatrix} k_x^2 & k_x k_y & k_x k_z \\ k_y k_x & k_y^2 & k_y k_z \\ k_z k_x & k_z k_y & k_z^2 \end{vmatrix}. \quad (32)$$

The LO frequency is shifted upwards relative to ω_0 of Sec. III. The main effect is this shift in frequency. For simplicity we will continue to regard the material as elastically isotropic with effective elastic constants modified by the polar fields. Consequently we can employ the analysis of the previous section, merely changing the definition of certain terms.

Thus we maintain the distinction between irrotational and divergenceless modes according to Eq. (9). It is convenient to modify the definition of the plate velocity v as follows:

$$\omega_L^2 - \omega^2 = v^2 k_x^2 \quad (33)$$

from which it follows that Eq. (16) becomes

$$k_L^2 = (\gamma s - 1)k_x^2, \quad k_T^2 = (s - 1)k_x^2 - k_0^2, \quad (34)$$

where

$$k_0^2 = \frac{\omega_L^2 - \omega_T^2}{v^2}. \quad (35)$$

The secular equation, Eq. (17), remains valid, but now Eq. (18) becomes

$$\frac{n}{N} \frac{dn}{dt} + \frac{\pi^2}{3} k_B^2 T_e N \frac{dT_e}{dt} = -\frac{\hbar\omega}{\tau} [n_e(\omega) - n(\omega)] N \hbar \omega. \quad (6)$$

$$\frac{dn(\omega)}{dt} = \frac{\hbar\omega}{\tau} [n_e(\omega) - n(\omega)] \frac{N}{2n} - \frac{[n(\omega) - n_e(\omega)]}{\tau_p}. \quad (12)$$

$$p = \gamma(s-2), \quad q = 2\gamma[(s-1)k_x^2 - k_0^2]^{1/2}/k_x, \quad (36)$$

$$r = 2\sqrt{\gamma s - 1}, \quad \iota = (s-2) - (k_0^2/k_x^2).$$

The splitting of the LO and TO frequencies profoundly modifies the ability of the surface to couple these modes together. Over the frequency range $\omega_L - \omega_T$ coupling of guided LO modes can only be accomplished with rapidly varying TO evanescent modes, and for $\omega \leq \omega_T$, only short-wavelength LO modes can be involved. Because of these consequences, a description of coupled modes tends to stretch any continuum model to its limits of validity and perhaps beyond it. With the caveat we will proceed first to describe the guided modes.

A. Guided modes

It may be noted that our results for *s*-polarized TO modes remain unaffected by the ionic nature of the material, and so we turn immediately to the coupling between guided LO and evanescent TO modes. Taking $k_T \approx ik_0$ and assuming for simplicity that k_0 is large, we obtain.

$$u_x = 2Ae^{ik_x x} \left[ik_x \sin k_L z - k_0 \frac{r}{t} [e^{-k_0 z} - \cos(k_L L) e^{-k_0 L} e^{k_0 z}] \right], \quad (37)$$

$$u_z = 2Ae^{ik_x x} \left[k_L \cos k_L z - k_x \frac{r}{t} [e^{-k_0 z} + \cos(k_L L) e^{-k_0 L} e^{k_0 z}] \right]$$

with $k_L L \approx n_L \pi$, n_L an integer (Fig. 7). In this coupling the contribution of the TO mode to the dilational stress is negligible, but the presence of the TO mode is still vital to cancel out the shear stress. If shear is neglected, no TO mode need be involved, and this is exactly the implicit assumption underlying the HD model, whose boundary condition $\nabla \cdot u = 0$ at the surface is exactly the same as our condition $T_z = 0$ when $\gamma = 0$.

It is interesting to observe that the mode pattern of Eq.

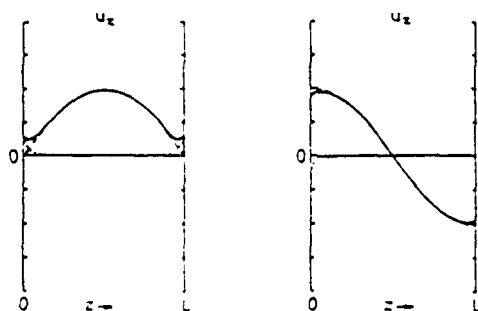


FIG. 7. Mode patterns for $n_L = 1$ in polar material (with $k_x = k_L$) (designations as in Fig. 5). Mode patterns for surface waves are approximately those of Fig. 6 in the absence of the TO component.

(37) satisfies the electromagnetic boundary conditions. The electric and magnetic fields associated with the TO mode are vanishingly small, so they do not enter. The LO mode has zero magnetic field and zero electric displacement D . Thus $D_z = 0$, and since $k_L = n_L \pi$, the tangential electric field vanishes at each surface. The continuity of D_z and E_x is then satisfied by having no fields in the vacuum.

The coupling between guided LO and guided TO for $\omega \leq \omega_T$ gives the mode patterns already given in Eqs. (2) and (21) but now with ω_T replacing ω_L in Eq. (33), $k_T L = n_T \pi$, $k_L L = n_L \pi$ and $n_L - n_T = 2m$.

$$k_L^2 = \gamma k_0^2 + k_x^2(\gamma s - 1), \quad k_T^2 = (s-1)k_x^2 \quad (38)$$

and

$$p = \gamma[k_0^2 + (s-2)k_x^2]/k_x^2, \quad q = 2\gamma\sqrt{s-1}, \quad (39)$$

$$r = (2/k_x) \sqrt{\gamma k_0^2 + k_x^2(\gamma s - 1)}, \quad \iota = (s-2).$$

B. Surface modes

There are still no surface *s*-polarized TO modes, but in general, surface waves consisting of mixed LO-*p*-polarized TO modes do exist, and their mode patterns for $L \rightarrow \infty$ are described by Eqs. (22) and (23) with p , q , $\alpha_L = ik_L$, $\alpha_T = ik_T$, given by Eqs. (34)-(36). Specific magnitudes must satisfy Eq. (14), which now leads to a quartic for the velocity factor s :

$$s^4 - 2(4-\alpha)s^3 - [8(3-2\gamma) + 12\alpha - \alpha^2]s^2 - [16(1-\gamma) + 8\alpha(3-2\gamma) - 4\alpha^2]s - 4\alpha^2 = 0, \quad (40)$$

where

$$\alpha = k_0^2/k_x^2.$$

Note that when $\alpha = 0$ Eq. (40) reduces to the nonpolar equation [Eq. (25)]. In the limit $\alpha \rightarrow \infty$, the solution is

$$s = 2, \quad (41)$$

independent of γ , from which

$$\alpha_L^2 = (1-2\gamma)k_x^2, \quad \alpha_T^2 = k_0^2 - k_x^2. \quad (42)$$

In this limit solutions exist provided $\gamma \leq \frac{1}{2}$. Waves propagate with surface phase velocity equal to $2^{1/2}v_T$. The antisymmetric solution is

$$u_x = 2Ak_x e^{ik_x x} \left[e^{-\alpha_L L/2} \cosh \alpha_L (z - L/2) - 2\frac{\alpha_L}{k_0} e^{-k_0 L} \cosh k_0 (z - L/2) \right], \quad (43)$$

$$u_z = 2iA\alpha_L e^{ik_x x} \left[-e^{-\alpha_L L/2} \sinh \alpha_L (z - L/2) + 2\frac{k_x^2}{k_0^2} e^{-k_0 L/2} \sinh k_0 (z - L/2) \right]$$

and the symmetric solution is

$$n_e(\omega) = n_o(\omega) - \frac{P(1-\alpha)}{N(\hbar\omega)}, \quad (20)$$

where P is the steady-state power density input.

The time constants characterizing the response are τ_T .

are strong enough to establish a common electron-hole temperature there is no need to consider well capture explicitly—it occurs as rapidly as the thermalization process.

Energy relaxation of the strongly coupled electron-hole

$$u_x = 2A k_x e^{ik_x z} \left\{ -e^{-\alpha_L L/2} \sinh_L(z - L/2) - 2 \frac{\alpha_L}{k_0} e^{-k_0 L/2} \sinh k_0(z - L/2) \right\} \quad (44)$$

$$u_z = 2iA \alpha_L r^{ik_x z} \left\{ e^{-\alpha_L L/2} \cosh \alpha_L(z - L/2) - 2 \frac{k_x^2}{k_0^2} e^{-k_0 L/2} \cosh k_0(z - L/2) \right\}.$$

The existence of this optical-mode analog to Rayleigh waves in polar material, as well as its appearance in non-polar material, depends upon the shear modulus being nonzero. If $\gamma = 0$, Eq. (42) shows that $\alpha_L^2 = k_x^2$. In this case the LO component has the property $\nabla \times \mathbf{u} = 0$ as well as $\nabla \cdot \mathbf{u} = 0$. Such a mode must have zero amplitude, which is consistent with the prediction of the HD model¹³ that no surface modes are possible in a free-standing plate. However, this conclusion derived from the HD model appears to be incorrect for real elastic solids, even though Eqs. (43) and (44) show that the amplitudes of the TO components are vanishingly small. We note that in this limit ($a \rightarrow \infty$), the solutions obtained above are valid for all plate thicknesses of interest. However, we also note that the tangential component of the electric field, which is proportional to u_z , is not zero at the surface, and so conventional electric boundary conditions are violated.

C. Surface polaritons

One well-known consequence of polarity is that it allows electromagnetic waves to directly couple with TO modes to form surface polaritons, as described by Fuchs and Kliewer.⁹ We will refer to these as FK modes. Their dispersion is depicted in Fig. 8. For large k_x the mode patterns are of the following forms: antisymmetric,

$$u_x = 2A e^{ik_x z} e^{-k_x L/2} k_x \cosh k_x(z - L/2), \quad (45)$$

$$u_z = -2iA e^{ik_x z} e^{-k_x L/2} k_x \sinh k_x(z - L/2)$$

and symmetric.

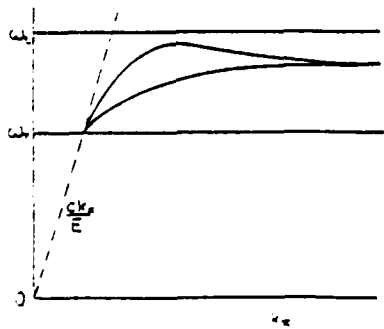


FIG. 8. Fuchs-Kliewer dispersion.

$$u_x = +2iA e^{ik_x z} e^{-k_x L/2} k_x \sinh k_x(z - L/2), \quad (46)$$

$$u_z = -2A e^{ik_x z} e^{-k_x L/2} k_x \cosh k_x(z - L/2).$$

When k_x is large compared with the wave vector of light at the same frequency, these solutions share the same frequency that lies between ω_T and ω_L and is given by

$$\omega_{FK} = \frac{\epsilon_s + \epsilon_0}{\epsilon_\infty + \epsilon_0} \omega_T, \quad (47)$$

where ϵ_s , ϵ_∞ are the static and high-frequency permittivities and ϵ_0 is the permittivity of the vacuum. For simplicity in our discussion we will assume that this condition is met.

Two comments can be made. First, it would appear from Eqs. (45) and (46) that we are dealing with a null mode since both $\nabla \cdot \mathbf{u}$ and $\nabla \times \mathbf{u}$ are zero. This, however, is not really so since the decay constant in hyperbolic terms is only approximately equal to the wave vector k_x . In fact the modes are TO modes with finite, but in the present approximation, vanishingly small rotation, which describes the rate of change of magnetic field. The solutions quoted are those obtained neglecting retardation (i.e., assuming the velocity of light to be infinite). They match smoothly with an evanescent electromagnetic wave in the vacuum.

The second comment is that these solutions violate the condition that the elastic stress vanish at the surface. Fuchs-Kliewer modes, conventionally described, are therefore unphysical. This rather important defect can be rectified by coupling with an LO guided mode of the same frequency, as was done in Sec. IV A. For $L \rightarrow \infty$ only cosine waves couple, and the corresponding mode

$$u_x = 2A e^{ik_x z} [ik_x \sinh k_L z + ik_L (e^{-k_x z} - \cosh k_L z e^{-k_x L} e^{k_x z})], \quad (48)$$

$$u_z = 2A e^{ik_x z} [k_L \cosh k_L z - k_L (e^{-k_x z} - \cosh k_L z e^{-k_x L} e^{k_x z})]$$

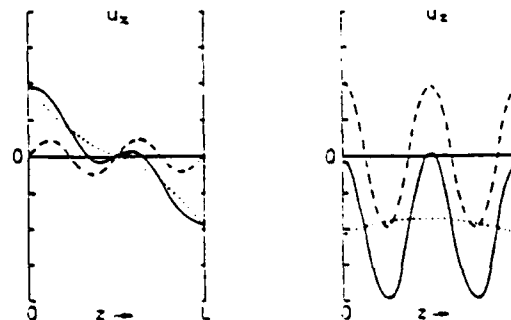


FIG. 9. Mode patterns for hybridized FK modes in polar material (with $KL = 4\pi$, $k_x L = \pi$). (Dashed line, LO; dotted line, FK; continuous line, LO - FK.) Note that this combination of FK and LO is possible only if the two modes have the same frequency. In general only certain values of k_x are allowed.

with $k_L L = n\pi$, satisfying

$$\omega_{FK}^2 = \omega_z^2 - \omega_g^2 (k_x^2 + k_z^2). \quad (49)$$

This mode pattern (Fig. 9) satisfies all elastic and electromagnetic boundary conditions. Note that when n is an odd integer, corresponding to an asymmetric guided mode, the coupling is to the asymmetric FK mode, and when n is an even integer both components are symmetric. In other words, like parity hybridizes with like parity.

A further discussion of hybridization of FK and LO modes taking into account FK dispersion will be reported soon in the future.

V. DISCUSSION

Our extension of classical elasticity theory to include optical modes has allowed us to describe the mixing of LO and TO modes at a free surface and to obtain the confined phonon spectrum. In particular, it has allowed us to demonstrate the existence of surface optical modes, which are analogous to Rayleigh waves. Hitherto only HD theory has predicted interface modes, but only at internal surfaces and only for LO modes. DC theory and the more sophisticated versions mentioned in the Introduction do not predict interface modes other than FK polaritons, so our conclusions here are quite new. Deciding the ontology of surface waves is of some importance for the electron-phonon interaction, since under some circumstances surface modes can interact strongly with electrons.¹⁴ For the same reason it is important to ascertain the strength of the interaction with FK polaritons. It has been argued elsewhere¹⁵ that such an interaction has the nature of a magnetic ($A \cdot p$) rather than of an electrical ($e\phi$) interaction, but clearly an even greater reappraisal of the FK interaction is now necessary as a result of our demonstration of hybridization of FK and LO modes.

The foregoing treatment has included nothing but the simplest cases and has merely sketched a rough outline of the topic. An extension to the quantum-well situation is underway, where continuity of stress replaces the vanishing of stress, and continuity of energy flow is entailed. It is clear that a self-consistent picture of confined modes can emerge from this program, so it is of interest to ask how valid such a picture can be as a description of optical waves in real matter. There are at least four problems, and there may be more. These have to do with the following: (1) The spatial variation of the mode pattern, (2) the relation of relative displacement (u) to ionic displacement, (3) the elastic anisotropy of real crystals, and (4) The electrical boundary conditions. We will comment on each in turn.

(1) It has already been remarked in Sec. IV that the polarity of the medium typically forced one of the components of a LO-TO hybridization to be rapidly varying, the more so the stronger the polarity, i.e., the more disparate the LO and TO zone-center frequencies. When the spatial variation of the mode function becomes significant over a primitive unit cell, the atomic nature of

the medium cannot be ignored. The important parameters are the wave vector k_0 , Eq. (35), and the dimension of the unit cell a_0 . So for a continuum theory to be valid we expect

$$|k_0 a_0| < 1. \quad (50)$$

For GaAs, $k_0 a_0 \approx 1$.

(2) The relation between HD boundary conditions and those arising from the linear-chain model was illuminated by Akero and Ando.⁹ When the force constants on either side of the interface are the same, and when the interface is taken to lie midway between atom A and atom B , the condition for mechanical stability simply entails the continuity of the displacements u_A and u_B , viz.,

$$\begin{aligned} \left[u_A - \frac{a_0}{2} \frac{\partial u_A}{\partial z} \right]_1 &= \left[u_A - \frac{a_0}{2} \frac{\partial u_A}{\partial z} \right]_2, \\ \left[u_B - \frac{a_0}{2} \frac{\partial u_B}{\partial z} \right]_1 &= \left[u_B - \frac{a_0}{2} \frac{\partial u_B}{\partial z} \right]_2. \end{aligned} \quad (51)$$

(Note there are no shear stresses here.) The parameter a_0 is now the interatomic spacing, assumed to be identical in both materials, and it is also assumed that u_A and u_B are describable by slowly varying envelope functions. Optical-mode relative displacement u for long wavelengths is related to u_A and u_B as follows:

$$u_A = -\frac{u}{1 + (M_A/M_B)}, \quad u_B = \frac{u}{1 + (M_B/M_A)}, \quad (52)$$

where M_A, M_B are the atomic masses. Substitution into Eq. (51) yields the connection rule

$$\begin{bmatrix} u \\ a_0 \frac{\partial u}{\partial z} \end{bmatrix}_1 = T_{12} \begin{bmatrix} u \\ a_0 \frac{\partial u}{\partial z} \end{bmatrix}_2, \quad (53)$$

where

$$T_{12} = \frac{r_1}{r_2} \begin{bmatrix} \frac{1}{2}(R + R^{-1}) & \frac{1}{2}(R - R^{-1}) \\ R - R^{-1} & \frac{1}{2}(R + R^{-1}) \end{bmatrix}. \quad (54)$$

Here $r = r_m + r_m^{-1}$, $r_m = (M_A/M_B)^{1/2}$, $R = r_{m1}/r_{m2}$. This connection rule satisfies continuity of energy flow. The corresponding connection rule for the continuum theory is

$$T_{12} = \begin{bmatrix} 1 & 0 \\ 0 & \begin{bmatrix} r_1 \\ r_2 \end{bmatrix}^2 \end{bmatrix}, \quad (55)$$

which agrees with microscopic theory only when $R = 1$, i.e., the mass ratios are common. In reality, the interface is never as precisely located as conventional microscopic theory assumes, and the position and properties of the interface affect the off-diagonal elements in Eq. (54). Consequently, boundary conditions relating relative displace-

tively. The new factors, f , r , and p are all dimensionless. The first, f , may be termed the injection hot-phonon factor; it is a measure of the energy injected into the phonon system and hence of the increase of phonon number in a mode. The second factor, r , is the recombination-heating

The departure from ideal behavior is often described in terms of a nonlinear gain coefficient ϵ_{nl} such that $g = g_0/(1 + \epsilon_{nl}S)$. The parameter ϵ_{nl} is found from the ratio of the damping rate γ to the square of the resonance frequency, f^2 . This ratio, usually named K , is proportional to ϵ_{nl} at

ment and elastic stresses in a continuum theory may not be a major source of error.

(3) Elastic anisotropy adds significant complexity. In directions other than the major crystallographic ones there is no clear distinction between LO and TO, and the degree of surface-induced hybridization depends upon direction following the directional dependence of dispersion. However, orientational effects of this sort are not likely to add anything qualitatively new to the picture obtained on the basis of an isotropic model. In any case, a straightforward application to the problem of the electron-phonon interaction will require some angular averaging. Anisotropy is therefore not likely to lead to significant problems.

(4) There is no question but that a transversely polarized wave of electromagnetic character must satisfy electromagnetic boundary conditions. The same is true of static fields. The question however is open concerning the applicability of electric boundary conditions to LO fields. We noticed that the surface optical modes described in Sec. IV B did not satisfy these conditions. Nor do linear-chain models in certain situations. Indeed, it was this problem that brought the DC model into clear conflict with microscopic models. The same question arises in the context of plasma waves. The special property of LO waves is that they have no electrical energy because the permittivity is zero. Electrical fields under this circumstance cannot exist in the absence of ionic polarization. At the surface of an ionic solid the electric field must therefore drop to zero over a distance of the order of atomic dimensions. If this is true, there is as much need for a continuum theory to address the issue as it would be for it to address the problem of continuity of interatomic forces, or indeed the continuity of matter. A surface or an interface is already a discontinuity of matter plus its properties, including polarization and associated fields, which suggests that it is unnecessary to add nonmechanical boundary conditions. If this view is adopted, it becomes clear that the DC model, insofar as it refers to the confinement of LO modes, is fundamentally flawed, and discontinuities of LO fields are to be expected. On the other hand, if this is denied, then one of the things that follows is that the surface modes of Sec. IV B cannot survive. This implies that surface modes exist in nonpolar material but not in polar material irrespective of the strength of polarity, provided the latter is nonzero. We appear to have exchanged one type of discontinuity for another. Note one final comment. The necessity for any boundary condition must be justified by arguments based on the physics of the situation. Hitherto there appears to be no such argument specifically directed at $\epsilon(\omega)=0$ LO modes for ensuring the continuity of the tangential component of the electric field.

It turns out, however, that both elastic and electromagnetic boundary conditions can be satisfied by invoking a scheme of triple hybridization involving LO, TO, and FK modes and distinguishing carefully between scalar and vector potentials.

We conclude with some comments on energy flow. General expressions for the energy flow in the z -direction may be written as follows.

$$S_z = -\frac{\bar{\rho}\omega v_L^2}{2i} (u_z^* \nabla \cdot u - u_z \nabla \cdot u^*) \text{ LO},$$

$$= -\frac{\bar{\rho}\omega v_T^2}{2i} [u_z^* (\nabla \times u)_y - u_z (\nabla \times u^*)_y] \text{ TO}, \quad (56)$$

where $\bar{\rho}$ is the reduced density. The solutions we have derived all obey $S_z = 0$. In the general case a basic boundary condition must be the continuity of S_z . Similarly we must have continuity of the stress components. These considerations suggest that if the z axis is perpendicular to the interface, the general boundary conditions to be satisfied for LO and TO modes are

$$S_z, T_y, T_x, T_z \text{ continuous}. \quad (57)$$

In general, we must add the usual electromagnetic boundary conditions.

ACKNOWLEDGMENTS

The author is grateful to the U.S. Office of Naval Research and to the Army Research Office (Contract No. DAAL03-90-G-0083) for their support of this project. He is also indebted to Dr. M. Babiker and Dr. N. Constantinou for many discussions, and to Professor L. Eastman for his encouragement of the project at Cornell and for his hospitality.

APPENDIX

The displacement of Eq. 13) must satisfy the following boundary conditions at $z=0$ and L :

$$T_3 = -c_{11} \left[(1-2\gamma) \frac{\partial u_z}{\partial x} - \frac{\partial u_z}{\partial z} \right] = 0, \quad (A1)$$

$$T_5 = -c_{44} \left[\frac{\partial u_z}{\partial z} + \frac{\partial u_z}{\partial x} \right] = 0. \quad (A2)$$

This entails the vanishing of the determinant

$$\begin{vmatrix} p & p & -q & -q \\ r & -r & t & -t \\ pf_L & pg_L & -qf_T & -qg_T \\ rf_L & rg_L & tf_T & -tg_T \end{vmatrix} = 0, \quad (A3)$$

where

$$p = 1 - 2\gamma - (k_L^2/k_T^2), \quad q = 2\gamma k_T/k_x, \\ r = 2k_L/k_x, \quad t = (k_T^2/k_x^2) - 1, \\ f_L = e^{-k_L L}, \quad g_L = e^{-k_L L}, \\ f_T = e^{-k_T L}, \quad g_T = e^{-k_T L}. \quad (A4)$$

This leads to the secular equation

$$qr - pt^2 \sin k_T L \sin k_L L - 2qrpt[\cos(k_L - k_T)L - 1] = 0 \quad (A5)$$

with the constraint on the frequency, namely,

$$\omega^2 = \omega_0^2 - v_L^2(k_x^2 + k_L^2) = \omega_0^2 - v_T^2(k_x^2 + k_T^2). \quad (A6)$$

The amplitudes are as follows:

$$B = \frac{[qr(f_T - g_T) - pt(2f_L - f_T - g_T)]}{\Delta} A. \quad (A7)$$

$$C = \frac{qr(f_L - g_L - 2g_T - pt(f_L - g_L))}{\Delta} \cdot \frac{p}{q} A. \quad (A8)$$

$$D = \frac{qr(2f_T - f_L - g_L) - pt(f_L - g_L)}{\Delta} \cdot \frac{p}{q} A, \quad (A9)$$

$$\Delta = qr(f_T - g_T) + pt(f_T + g_T - 2g_L). \quad (A10)$$

Sometimes it is useful to express the secular equation (A5) as follows:

$$(qr \sin \theta_L \cos \theta_T + pt \cos \theta_L \sin \theta_T) \times (qr \cos \theta_L \sin \theta_T + pt \sin \theta_L \cos \theta_T) = 0. \quad (A11)$$

where

$$\theta_L = k_L L/2 \text{ and } \theta_T = k_T L/2.$$

*Permanent address: Department of Physics, University of Essex, Colchester CO4 3SQ, United Kingdom.

¹Lord Rayleigh, Proc. London Math. Soc. 20, 225 (1989) [*Lord Rayleigh Collected Papers* (Cambridge University Press, London, 1902), Vol. 3, p. 249].

²R. Lassnig, Phys. Rev. B 30, 7132 (1984).

³L. Wendler and R. Pechstedt, Phys. Status Solidi B 138, 197 (1986).

⁴E. Molinari, A. Fasolino, and K. Kunc, Superlatt. Microstruct. 2, 397 (1986).

⁵M. Babiker, J. Phys. C 19, 683 (1986).

⁶H. Akero and T. Ando, Phys. Rev. B 40, 2914 (1989).

⁷K. Huang and B-F Zhu, Phys. Rev. B 38, 2183 (1988); 38, 13377 (1988).

⁸F. Bechstedt and H. Gerecke, Phys. Status Solidi B 156, 151 (1989); 156, 565 (1989).

⁹R. Fuchs and K. L. Kliewer, Phys. Rev. 140A, 2076 (1965).

¹⁰R. Haupt and L. Wendler, Phys. Rev. B 44, 1850 (1991).

¹¹B. K. Ridley and M. Babiker, Phys. Rev. B 45, 9096 (1991).

¹²For example, L. D. Landau and E. M. Lifshitz, *Theory of Elasticity*, 3rd ed. (Pergamon, New York, 1986), p. 88.

¹³N. Constantinou and B. K. Ridley, J. Phys. Condens. Matter 2, 7465 (1990).

¹⁴B. K. Ridley, Phys. Rev. B 39, 5282 (1989).

A continuum theory of optical phonon hybrids
and their interaction with electrons in a quantum well

B.K. Ridley

Department of Physics, University of Essex, Colchester, England.

ABSTRACT

Hybrid optical modes, consisting of a unique linear combination of LO, TO and IP (interface polariton) modes satisfying both elastic and electromagnetic boundary conditions, are described in a continuum approximation. Mode patterns and mode dispersion are obtained which agree with microscopic calculations. Inter- and intrasubband electron scattering rates are obtained which also agree with those derived on the basis of microscopic models.

1. INTRODUCTION

Continuum theories^{1,2} of confined LO modes hitherto fail to satisfy both elastic and electromagnetic boundary conditions and do not, in general, describe properly the mode patterns and mode dispersion obtained in microscopic calculations.^{3,4,5} In structures where wells and barriers are many unit cells thick, continuum theory has an important role to play in facilitating the calculation of electron scattering rates and of phonon decay rates, and, not least, in providing a conceptual framework. Here we describe how hybrid optical modes consisting of unique linear combinations of LO, TO and IP (interface polariton) modes solve the boundary-condition problem, and provide a description which agrees remarkably well with the results of microscopic theory.

2. LO, TO AND IP HYBRIDS

Assuming a quadratic dispersion for LO and TO modes and electromagnetic dispersion for IP modes in an elastically isotropic medium, we take the relative ionic displacement u to be a linear combination of LO, TO and IP components which share the same frequency and the same in-plane wavevector, which makes the combination unique:

$$u = u_{LO} + u_{TO} + u_{IP}$$

1.

with an associated electric field E given by

$$E = -\rho_0(u_{LO} + su_{IP}),$$

2.

where $\rho_0 = e^*/\epsilon_0 V_0$ is the space-charge density, e^* is the effective ionic charge, ϵ_0 is the free-space permittivity and V_0 is the volume of a primitive unit cell. We have assumed that the TO mode has vanishingly small electric field. The parameter $s = (\omega^2 - \omega_{TO}^2)/(\omega_{LO}^2 - \omega_{TO}^2)$ is the usual fraction of the LO space-charge density which is associated with an IP mode of frequency ω , and ω_{LO} , ω_{TO} are the LO, TO zone-centre frequencies. The displacement components obey longitudinal and transverse conditions: $\Delta \times u_{LO} = 0$, $\Delta \cdot u_{TO} = 0$, $\Delta \cdot u_{IP} = 0$.

For elastically infinitely rigid interfaces (roughly corresponding to the AlAs/GaAs interface) the boundary conditions are $u = 0$, E_x continuous, D_z continuous at $z = \pm a/2$, where x is along the plane, z is perpendicular to it, and a is the well-width. The hybrids whose frequencies lie near to ω_{LO} (as distinct from ω_{TO}) are the ones which interact most strongly with electrons. Mode patterns for these turn out to be given by

$$u_x = ik_x A e^{i(k_x x - \omega t)} [\sin k_L z - a_T \sinh k_T z - a_p \sinh k_x z] \quad (a)$$

Odd

3.

$$u_z = k_L A e^{i(k_x x - \omega t)} [\cos k_L z - a_T (k_x^2/k_L k_T) \cosh k_T z - a_p (k_x/k_L) \cosh k_x z] \quad (b)$$

or

$$u_x = k_x A e^{i(k_x x - \omega t)} [\cos k_L z - b_T \cosh k_T z - b_p \cosh k_x z] \quad (a)$$

Even

$$u_z = ik_L A e^{i(k_x x - \omega t)} [\sin k_L z + b_T (k_x^2/k_L k_T) \sinh k_T z + b_p (k_x/k_L) \sinh k_x z] \quad (b)$$

where

$$\omega^2 = \omega_{LO}^2 - v_L^2 (k_L^2 + k_x^2) = \omega_{TO}^2 - v_T^2 (k_x^2 - k_T^2) = [c^2/\epsilon(\omega) \mu_0] (k_x^2 - k_T^2).$$

Here v_L, v_T are velocities describing the dispersion, c is the velocity of light, $\epsilon(\omega) = \epsilon_\infty (\omega^2 - \omega_{LO}^2)/(\omega^2 - \omega_{TO}^2)$, μ_0 is the permeability, and k_p is the evanescent wave-vector of the IP mode, which in eqs. 3 and 4 has been taken to be equal to k_x , assuming the non-retarded limit. The parameters a_T, a_p, b_T, b_p are given by

$$a_T = \frac{[1 - p_1 \tanh(k_x a/2)] \sin(k_L a/2)}{\cosh(k_T a/2)}, \quad a_p = p_1 \frac{\sin(k_L a/2)}{\cosh(k_x a/2)}, \quad p_1 = \frac{1}{s(\tanh(k_x a/2) + r)} \quad (a)$$

5.

$$b_T = \frac{1 - p_2 \coth(k_x a/2) \cos(k_L a/2)}{\sinh(k_T a/2)}, \quad b_p = p_2 \frac{\cos(k_L a/2)}{\sinh(k_x a/2)}, \quad p_2 = \frac{1}{s(\coth(k_x a/2) + r)} \quad (b)$$

In these equations $r = \epsilon(\omega)/\epsilon_B$, where ϵ_B is the permittivity in the barrier, assumed for simplicity to be frequency independent, and it is further assumed that k_T is a large evanescent wavevector such that $\tanh(k_T a/2) \approx 1$. The real wavevector of the LO component, k_L , is determined from the dispersion relations, which are

$$\text{Odd modes: } \cot(k_L a/2) = (k_x/k_L) [p_1 + (k_x/k_T) (1 - p_1 \tanh(k_x a/2))] \quad (a)$$

6.

$$\text{Even modes: } \tan(k_L a/2) = - (k_x/k_L) [p_2 + (k_x/k_T) (1 - p_2 \coth(k_x a/2))] \quad (b)$$

In the barriers $u = 0$ and there are only evanescent electric fields.

Mode patterns for small in-plane wavevector, k_x , are depicted in Fig. 1 for the four highest frequency modes. These are closely like patterns obtained in microscopic theory. Fig. 2 depicts the dispersion for a 100 Å well. Odd modes are affected by the IP dispersion, even modes are not. In particular, the LO1 mode rapidly evolves into a mode near the original LO3 frequency. This "disappearance" of the LO1 mode is characteristic of the effect of hybridization and was first pointed out by Huang and Zhu³ in their microscopic theory. It is interesting that this property is also obtained in a continuum theory.

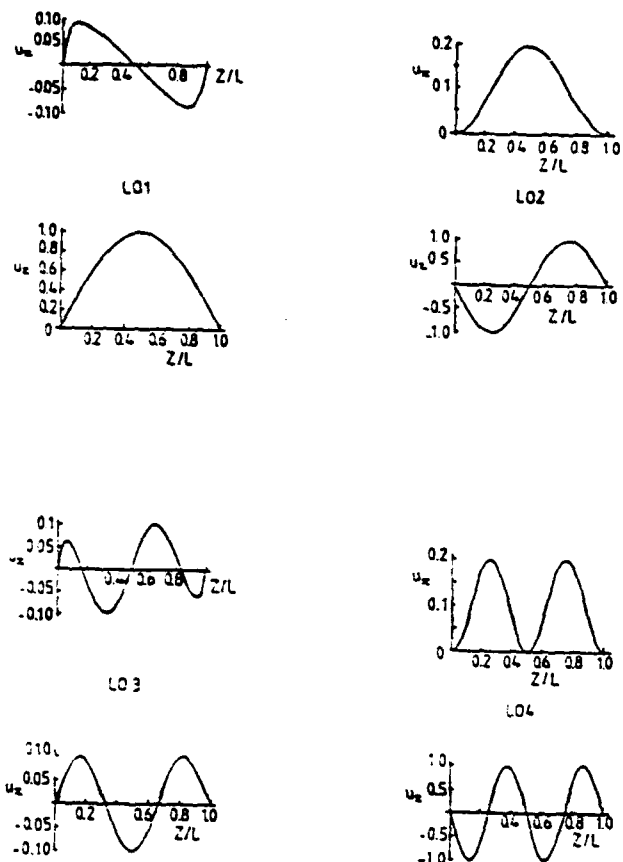


Fig. 1 Relative ion displacements for the four highest frequency hybrids in the limit $k_x a \rightarrow 0$.

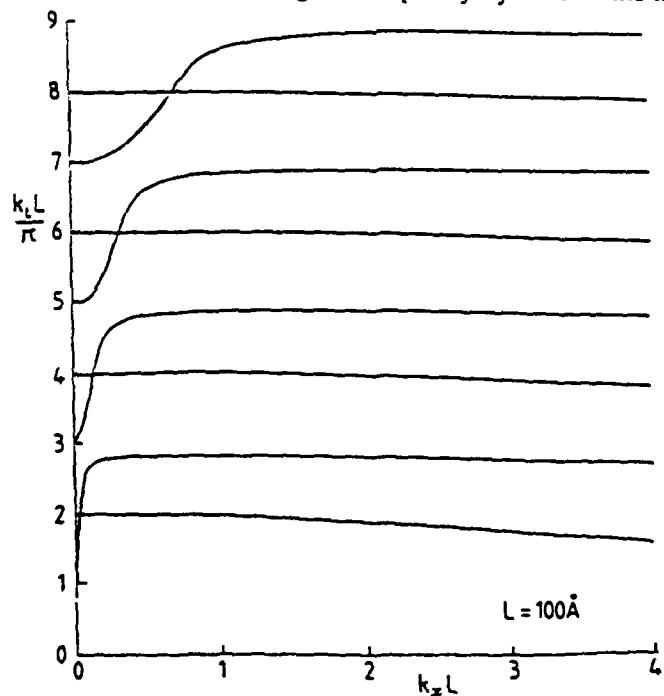


Fig. 2 Dispersion plots of k_L versus k_x , solutions of eq. 6, for $a = 100 \text{ \AA}$.

3. THE ELECTRON-HYBRIDON INTERACTION

These hybrids have mainly mechanical energy, as have phonons, but the interaction with electrons is partly electric and partly magnetic, the LO component contributing a scalar potential, ϕ , the IP component a vector potential \vec{A} . Thus

$$\phi = \rho_0 A e^{i(k_x x - \omega t)} \sin k_L z \quad (a)$$

Odd

7.

$$\hat{A}_x = \frac{\rho_0 k_x}{\omega} A e^{i(k_x x - \omega t)} a_p \sin k_x z \quad (b)$$

$$\hat{A}_z = -\frac{i \rho_0 k_x}{\omega} A e^{i(k_x x - \omega t)} a_p \cosh k_x z \quad (c)$$

$$\phi = -\rho_0 A e^{i(k_x x - \omega t)} \cos k_L z \quad (a)$$

Even

8.

$$\hat{A}_x = -\frac{i \rho_0 k_x}{\omega} A e^{i(k_x x - \omega t)} b_p \cosh k_x z \quad (b)$$

$$\hat{A}_z = -\frac{\rho_0 k_x}{\omega} A e^{i(k_x x - \omega t)} b_p \sinh k_x z \quad (c)$$

It is interesting that in general neither ϕ nor \hat{A} is continuous at the interface, but what matters is the interaction with an electron, $H = -e\phi + (e/m) \vec{A} \cdot \vec{p}$, and this turns out to be continuous provided that the electron travels coherently with the wave, i.e. with a group velocity equal to ω/k_x . This condition generalizes the usual electrostatic argument for ϕ to be continuous to the time-dependent situation. It should be noted, in this context, that in microscopic theories hitherto, electric fields have been always associated with a scalar potential, an association which ignores the time-dependent properties of the system.

The hybrid field can be quantized to give "hybridons" and the scattering rates of intrasubband processes can be computed using the Fermi Golden Rule. Fig. 3 shows the intrasubband rate for an electron in the lowest subband of an infinitely deep well in GaAs when the electron energy = $\hbar\omega$. The interaction is solely with GaAs hybridons. Comparison is made with the predictions of the hydrodynamic model, the dielectric continuum model, the bulk-phonon model and the Huang-Zhu model.⁶ The agreement with the latter model, which is based on a scheme of assigning envelope functions to the results of microscopic theory, at small well-widths, is striking. Fig. 4 shows the rates for the intersubband process of an electron at the bottom of subband 2 scattering into subband 1 via the emission of a (converted) LO1 hybridon. (Addition of contributions from LO3 etc. would close the gap between our result and that using Huang and Zhu modes.)

4. CONCLUSIONS

The continuum model of hybridization successfully predicts confined-mode patterns and electron scattering rates. It shows that hybridization causes the rates to lessen with decreasing well-width. Previous models showed this reduction to be true only for LO mode interaction but not for the IP interaction. Hybridization forces the IP interaction into the LO mold. It is only in a material like AlAs where LO dispersion is too weak to allow hybridization over all the frequency range between ω_{LO} and ω_{TO} that IP modes can retain their characteristic behaviour.

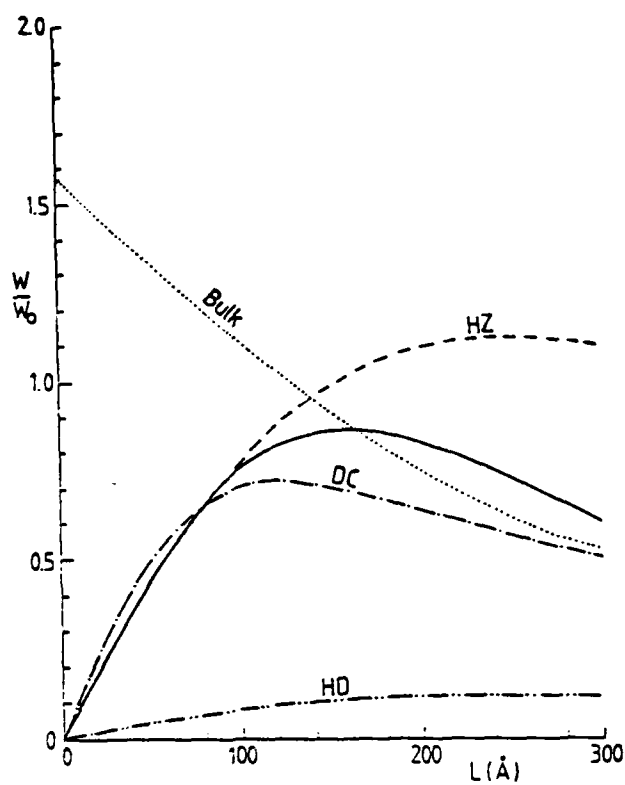


Fig. 3 Intrasubband scattering rate for an electron with energy $\hbar\omega$ interacting with LO2, in an infinitely deep GaAs well. (HD = hydrodynamic model, DC = dielectric continuum model, HZ = Huang-Zhu model).

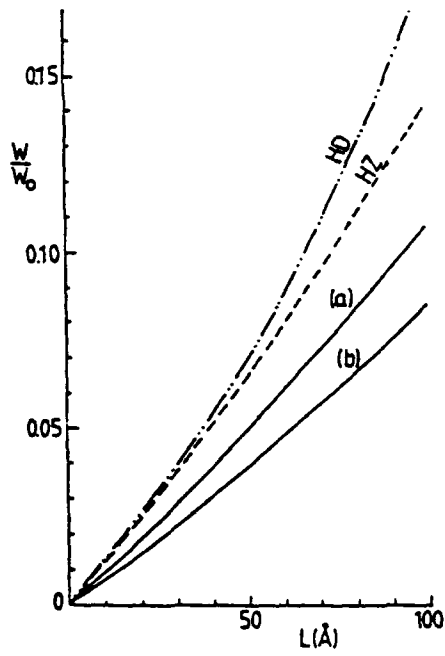


Fig. 4 Intersubband scattering rate for an electron at the bottom of subband 2 scattering to subband 1 emitting a "converter" LO1 hybirdon.

ACKNOWLEDGEMENTS

This work is supported by the US Office of Naval Research and by the US Army Research Office.

REFERENCES

1. R. Fuchs and K.L. Kiewer, Phys. Rev. A140 2076 (1965)
2. M. Babiker, J. Phys. C. 19 683 (1986)
3. K. Huang and B-F. Zhu, Phys. Rev. B38 2183 and 13,377 (1988).
4. F. Bechstedt and H. Gericke, Phys. Stat. Sol. b154 565 and b156 157 (1989)
5. A. Fasolino, E. Molinari and K. Khunc, Phys. Rev. B41 8302 (1990)
6. S. Rudin and T.L. Reinecke, Phys. Rev. B41 7713 (1990) and B43 9288 (1991)L

Hot carriers and the frequency response of quantum well lasers

L. F. Lester and B. K. Ridley^a

School of Electrical Engineering, Cornell University, Phillips Hall, Ithaca, New York 14853-5401

(Received 20 April 1992; accepted for publication 22 June 1992)

A simple analytical model is obtained to describe the effect of carrier heating on the frequency response of a quantum well laser. The principal factors are taken to be injection heating, recombination heating, and hot phonons. The model is applied to the GaAs/GaInAs strained layer system and is shown to qualitatively account for many of the nonideal features observed. The nonlinear effects cannot be described satisfactorily by a single phenomenological "gain suppression" factor. However, at low drives the conventional gain suppression factor can be expressed in terms of the phonon lifetime and the temperature-relaxation time. The response is mediated by several time constants which, in our example, combine to give an effective time constant of about 10 ps. The modulation frequency response becomes seriously impaired when the differential gain is lowered by a factor of 2 and the time constants describing scattering and phonon lifetime are increased by a factor of 2.

I. INTRODUCTION

The effect of carrier heating on the performance of injection lasers has been considered by a number of authors.¹⁻⁴ The source of heating has been considered to be the total power dissipated,¹ Auger processes,² recombination,^{3,4} and free-carrier absorption,^{3,4} and recent work has related carrier heating to so-called nonlinear gain suppression directly³ and in combination with hole burning.⁴ That carrier heating occurs in lasers is well established⁵ and femtosecond studies suggest that it alone can explain gain suppression.⁶ Since much of the foregoing work has been on bulk lasers, it is of interest to study carrier heating in quantum wells and in particular to elucidate its effect on the modulation frequency response, and that is the topic of this article.

Our interest will be focused on high-speed (and therefore short) quantum well strained layer lasers in which the effective masses of the electrons and holes in their lowest subbands are similar in magnitude.⁷ The main source of external heating in the quantum well case is that provided by energetic carriers injected at the top of the well. These relax via intercarrier collisions and via optical phonon emission, thus heating both carrier and phonon gases. Of the heating mechanisms invoked in previous work we retain only recombination heating and regard the contribution from Auger processes and free-carrier absorption as being negligible. Comprehensive work on energy relaxation in bulk and quantum well material, recently reviewed,⁸ shows clear evidence that at high carrier densities the role of hot phonons cannot be neglected. We have therefore assumed that the most important factors to be taken into account are injection heating, recombination heating, and hot phonons, and we explore how they influence the performance of a laser. As far as we are aware such an analysis has not been carried out previously.

The system to be described is a complex one consisting

of several populations (electrons, holes, photons, phonons) dynamically coupled together. Detailed modeling can only be carried out numerically. Our purpose in this article is not to attempt a numerical analysis but instead it is to construct an analytic model which embodies the fundamental physical processes involved and which illustrates the factors of importance. Such a model is a preliminary (in our view a necessary preliminary) to a computer simulation.

This article is organized as follows: In Sec. II, we discuss energy relaxation in a degenerate gas. A number of investigations for GaAs show that at densities of order 10^{18} cm⁻³ a time constant characterizing electron-electron scattering and plasmon emission is of order 60 fs or less.⁸ Given the assumed near equality of electron and hole masses, that allows us to adopt the simplification of a common carrier temperature established virtually instantaneously. We simplify the electron (hole)-phonon interaction in a quantum well by ignoring hybridization of the LO, TO, and IP (interface polariton) modes and take the rate to be proportional to the density of subband states. This allows us to write down simple coupled equations for the carrier temperature and the phonon number, taking the degenerate limit and we briefly explore the linear response of the system. This leads to the identification of a new time constant which characterizes the temperature relaxation in a degenerate gas. In Sec. III, the equations are combined with the standard ones for photon and carrier densities, and the injected energy is related to the current density. The linear response of this coupled system of carriers, phonons, and photons is analyzed and the resultant response function is compared with the ideal (no carrier heating) case. A distinction is discovered between the frequency of maximum response and the frequency of relaxation oscillations, and the inadequacy of describing the nonlinear effects which are predicted by a single gain suppression factor is pointed out. In Sec. IV, the theory is applied to the GaAs/Ga_{0.7}In_{0.3}As strained layer laser and the response function is found for a number of situations in all of which the current density and photon flux is taken to be high in

^aHome address: Department of Physics, University of Essex, Colchester, England.

order to illustrate the nonlinearities. Qualitative features of nonideal behavior observed in practice are well reproduced by the theory. However, because of the simplistic nature of the model no attempt is made to obtain a quantitative fit. The article concludes in Sec. V with a brief discussion.

Our aim throughout is to present a simple analytic model in order to illustrate the processes involved. We conclude that carrier heating itself does not seriously impair the frequency bandwidth, but that it complicates the response and forces a reappraisal of how nonlinear effects should be interpreted.

II. ENERGY RELAXATION

The rate of increase in energy density, U , can be expressed in terms of the rate of change of occupation probability, $f(E)$, of a state with energy E as follows:

$$\frac{dU}{dt} = \int E \frac{df(E)}{dt} N(E) dE, \quad (1)$$

where $N(E)$ is the density of states function. In cases where the occupation probability changes solely by the emission and absorption of optical phonons of energy $\hbar\omega$ Eq. (1) can be written in the following form:

$$\begin{aligned} \frac{dU}{dt} = & \int EN(E)dE \int \frac{2\pi}{\hbar} (M^2(E, E') \{n(\omega)f(E')[1-f(E)] - [n(\omega)+1]f(E)[1-f(E')]\} \\ & \times \delta(E' - E + \hbar\omega)N(E')dE' + (M^2(E, E'') \{[n(\omega)+1]f(E'')[1-f(E)] - n(\omega)f(E)[1-f(E'')]\} \\ & \times \delta(E'' - E - \hbar\omega)N(E'')dE''), \end{aligned} \quad (2)$$

where $M^2(E, E')$ is the squared matrix element for the transition, $n(\omega)$ is the phonon occupation number, and the second integral is over allowed final states. This integral is particularly simple when the matrix element is independent of phonon wave vector, for then:

$$\begin{aligned} \frac{dU}{dt} = & \int EN(E)dE \left(\frac{1}{\tau(E \pm \hbar\omega, E)} \{n(\omega)f(E - \hbar\omega) \right. \\ & \times [1-f(E)] - [n(\omega)+1]f(E)[1-f(E - \hbar\omega)]\} \\ & + \frac{1}{\tau(E + \hbar\omega, E)} \{[n(\omega)+1]f(E + \hbar\omega)[1-f(E)] \right. \\ & \left. - n(\omega)f(E)[1-f(E + \hbar\omega)]\} \right), \end{aligned} \quad (3)$$

where $\tau(E \pm \hbar\omega, E)$ is the scattering time constant for the process. The two types of electron-phonon interaction of importance are the polar and the nonpolar (in a polar material). To a good approximation the nonpolar interaction—relevant for holes and electrons in L —is mediated by a matrix element which is independent of wave vector, but the polar interaction is not so simple in general. However, in a two-dimensional (2D) system the dependence of the polar interaction on wave vector is weakened by confinement, and where confinement is strong Eq. (3) is approximately valid even for the polar case. A further simplification which can be made for a 2D system in which only the lowest energy subband is occupied is that the scattering time, which is inversely proportional to the single spin density of states, can be taken to be energy-independent if nonparabolicity is ignored. In what follows, both of these simplifying features will be adopted.

With $\tau(E) = \tau$ and $N(F) = N$ plus the assumption that the distribution function is of Fermi-Dirac form characterized by an electron temperature T_e , the integrals in Eq.

(3) can be evaluated analytically in the degenerate limit viz.: $\exp(E_F/k_B T_e) > 1$, where E_F is the Fermi energy measured from the subband edges. Since degeneracy, or near degeneracy, is a prerequisite for laser action we have taken the degenerate limit in order to obtain simple analytical results which illustrate hot-carrier effects. Thus, for a 2D degenerate electron gas the rate of increase in energy density reduces to

$$\frac{dU}{dt} = -\frac{\hbar\omega}{\tau} [n_e(\omega) - n(\omega)] N \hbar\omega, \quad (4)$$

where $n_e(\omega)$ is the Bose-Einstein occupation number when the phonon temperature T_p equals the electron temperature. The rate is zero when $T_e = T_p = T_L$, where T_L is the lattice temperature, as it should at thermodynamic equilibrium. The factor $N \hbar\omega$ is the effective density of electrons which can interact with the phonons, which represents a fraction $\hbar\omega/E_F$ of the total. In a nondegenerate system the corresponding equation would have the total carrier density replacing $N \hbar\omega$. Thus, degeneracy reduces the energy relaxation rate by the fraction $\hbar\omega/E_F$.

In a nondegenerate gas, energy relaxation translates linearly to temperature relaxation, but this is not the case when the gas is degenerate. In 2D the mean energy $\langle E \rangle$ is given for $\exp(E_F/k_B T_e) > 1$ by

$$\langle E \rangle = \frac{1}{2} E_F \left[1 + \frac{\pi^2}{3} \left(\frac{k_B T_e}{E_F} \right)^2 \right]. \quad (5)$$

[Note that in the derivations of Eqs. (4) and (5), identical methods were used in evaluating the integrals, and these equations are therefore mutually consistent.] With $U = n \langle E \rangle$ and $E_F = n/N$, where n is the electron density, Eq. (4) becomes

$$\frac{n}{N} \frac{dn}{dt} + \frac{\pi^2}{3} k_B T_e N \frac{dT_e}{dt} = -\frac{\hbar\omega}{\tau} [n_e(\omega) - n(\omega)] N \hbar\omega. \quad (6)$$

The temperature relaxation rate then depends upon the carrier density relaxation rate as well as the energy relaxation rate. Indeed, if the latter is zero the temperature rises as the carrier density falls, and this effect was termed recombination heating by Bimberg and Mycielski.^{9,10} On the other hand, if the carrier density remains constant the temperature relaxation rate is given by

$$k_B \frac{dT_e}{dt} = -\frac{\hbar\omega}{\tau_p} [n_e(\omega) - n(\omega)], \quad (7)$$

where the new time constant is given by

$$\tau_p^* = \frac{\tau^* k_B T_e}{3\hbar\omega}. \quad (8)$$

This time constant would enter a description of the temperature fall off after, say, the optical injection of hot electrons, as observed by time-resolved photoluminescence, provided no hot phonon effects were present.

To calculate the effect of hot phonons we adopt the simplifying assumption that a phonon temperature can be defined for the modes interacting most strongly with the electrons. We then assume that the rate of change of occupation number can be expressed as follows:

$$\frac{dn(\omega)}{dt} = -\frac{dU}{dt} \frac{V}{N_\omega \hbar\omega} - \frac{[n(\omega) - n_0(\omega)]}{\tau_p}, \quad (9)$$

where N_ω is the number of phonon modes, V is the volume of the quantum well, $n_0(\omega)$ is the occupation number at thermodynamic equilibrium, and τ_p is the phonon lifetime. We assume all phonons involved have the same frequency and decay at the same rate, which is very nearly true. To establish the number of modes we observe that momentum and energy conservation restricts the phonon wave vector, q , to lie between q_{\max} and q_{\min} where for emission:

$$q_{\max} = k[1 + (1 - \hbar\omega/E)^{1/2}],$$

$$q_{\min} = k[1 - (1 - \hbar\omega/E)^{1/2}],$$

for absorption:

$$q_{\max} = k[(1 - \hbar\omega/E)^{1/2} + 1],$$

$$q_{\min} = k[(1 + \hbar\omega/E)^{1/2} - 1],$$

where E , k are the energy and in-plane wave vector of the electron. In our model of degeneracy we can for simplicity take $0 < q < 2k_F$, where k_F is the wave vector on the Fermi surface. The number of modes is then given by

$$N_\omega = \frac{(2k_F)^2}{4\pi L_w} V = 2nV, \quad (11)$$

where L_w is the well width and V is the well volume. [Note that Eq. (11) overestimates the number of modes if degeneracy is weak and hence leads to an underestimation of hot-phonon effects.] Thus,

$$\frac{dn(\omega)}{dt} = \frac{\hbar\omega}{\tau} [n_e(\omega) - n(\omega)] \frac{N}{2n} - \frac{[n(\omega) - n_0(\omega)]}{\tau_p}. \quad (12)$$

The phonon number in the steady state is then given by

$$n(\omega) = \frac{n_0(\omega) + n_e(\omega) (N \hbar\omega/2n) (\tau_p/\tau)}{1 + (N \hbar\omega/2n) (\tau_p/\tau)} \quad (13)$$

and $n(\omega) = n_0(\omega)$ only when $n_e(\omega) = n_0(\omega)$. In extremely degenerate systems such that $(N \hbar\omega/2n) (\tau_p/\tau) \ll 1$, hot-phonon effects are negligible. But typically, $\tau_p/\tau \gg 1$, and so hot-phonon effects can occur even when, as we have been assuming, $(\hbar\omega/E_F) \ll 1$.

We have implicitly assumed that the normalization volumes of the carriers and phonons are identical, but in general this will not be so. For example, vibrations may be excited in the barriers in addition to being excited in the wells. Following an analogy with the situation for photons in a semiconductor laser, we can introduce a phonon confinement factor, Γ_p , which is generally less than unity, and interpret the scattering rate, τ^{-1} , as

$$\frac{1}{\tau} = \frac{\Gamma_p}{\tau_0} \quad (14)$$

where τ_0 is the scattering time for $\Gamma_p = 1$.

The linear response of the coupled system can be described by introducing a power source P on the right-hand side of Eq. (6) with a small modulation at an angular frequency Ω . We obtain

$$k_B \delta T = \frac{\Omega^2 \tau_T (1 + \alpha + i\Omega \tau_p) (\delta P \tau / N \hbar\omega)}{\Omega^2 - \Omega^2 + i\Omega[(1/\tau_T) + (1/\tau_p)(1 + \alpha)]}, \quad (15)$$

where

$$\alpha = (N \hbar\omega/2n) (\tau_p/\tau),$$

and

$$\Omega^2 = (\tau_T \tau_p)^{-1},$$

$$\tau_T = \frac{\pi^2}{3} \left(\frac{k_B T_e}{\hbar\omega} \right)^3 \frac{\tau}{n_e(\omega) [n_e(\omega) + 1]} \quad (16)$$

$$U = \frac{\pi^2}{2N_e} \left[1 + \frac{\pi^2}{3} \left(\frac{k_B T_e V_e}{n} \right)^2 \right] + \frac{\rho^2}{2N_h} \left[1 + \frac{\pi^2}{3} \left(\frac{k_B T_e N_h}{n} \right)^2 \right] \\ U = \frac{n^2}{2N_e} \left[1 + \frac{\pi^2}{3} \left(\frac{k_B T_e}{n} \right)^2 N_e N_h \right]. \quad (17)$$

The dc response is

$$k_B \delta T = \tau_T (1 + \alpha) (\delta P \tau / N \hbar\omega). \quad (18)$$

Normalizing to the dc response leads finally to the response function $R(\Omega)$ given by

$$R(\Omega) = \frac{\Omega^2 (1 + i\Omega \tau_p^*)}{\Omega^2 - \Omega^2 + i\Omega[(1/\tau_T) + (1/\tau_p)]}. \quad (19)$$

where $\tau_p^* = \tau_p/(1 + \alpha)$. In Eq. (17), $n_e(\omega)$ is given by

$$n_e(\omega) = n_o(\omega) + \frac{P(1-\alpha)}{N(\hbar\omega)}. \quad (20)$$

where P is the steady-state power density input.

The time constants characterizing the response are τ_T , τ_p , and τ_h^* . Typically, at room temperature, each of the three time constants is of order $10 \times \tau$, i.e., of the order of 1 ps. In other words, degeneracy and hot-phonon effects reduce the energy relaxation rate by an order of magnitude. This reduction is due partly to the reduced number of electrons which can participate and partly due to a hot-phonon effect. It should be noted, however, that the hot-phonon effect weakens with increasing degeneracy as more and more phonon modes become available and the occupation of each becomes progressively less ($\alpha \rightarrow 0$). In choosing the degeneracy limit we underestimate the hot-phonon effects somewhat.

III. LASER DYNAMICS

In a semiconductor quantum well laser carrier heating occurs through the act of injecting electrons and holes across band-edge discontinuities. If the latter are ΔE_c and ΔE_v for the discontinuities in the conduction band and valence band then an amount of energy $\Delta E_g = \Delta E_c - \Delta E_v$ is injected for every electron-hole pair. In the presence of a substantial photon flux there will also be heating associated with free-carrier absorption, but for simplicity we will assume that this is small compared with that unavoidably associated with the injection process. The questions to be answered are: how is that injected energy dissipated? and how does heating affect performance of the laser?

To answer these questions we will assume for simplicity that complete carrier thermalization occurs virtually instantaneously so that a single temperature, T_τ , instantaneously characterizes the quasi-Fermi distributions of electrons and holes. For 300 meV electrons in bulk GaAs in a concentration of order 10^{18} cm^{-3} the mean free path associated with plasmon emission and single particle processes is about 500 Å according to the calculations of Rorison and Herbert,¹¹ corresponding to a time constant of about 40 fs. Monte Carlo estimates of thermalization time in a quantum well of GaAs gives 200 fs.¹² These times are certainly short enough to warrant our assumption as regards electrons. This will also be true for holes provided the hole mass is similar to that of the electron which it is in strained layer lasers of GaAs/InGaAs. In bulk material, the disparity between electron and hole masses means that equalization of electron and hole temperatures is slow, full thermalization taking times of order 10 ps.^{13,14} But in the case of strained layer lasers thermalization times will be of order 100 fs. Thus, our assumption will be reasonably valid for (working) strained layer lasers, and may be a reasonable approximation for quantum well lasers in general, but it is certainly invalid for bulk lasers.

Our assumption of instantaneous thermalization allows us to make a further simplification, over and above that concerning a common temperature, regarding well capture. In detail this process is difficult to describe accurately, but if it is assumed that carrier-carrier interactions

are strong enough to establish a common electron-hole temperature there is no need to consider well capture explicitly—it occurs as rapidly as the thermalization process.

Energy relaxation of the strongly coupled electron-hole degenerate gases is via the emission of optical phonons (or, more accurately, hybridons, the quanta of the hybrid LO, TO, and IP modes which occur in layered systems, but we will continue to use the more familiar term), through the Fröhlich interaction for both types of carrier and through the deformation potential interaction for holes. In general, different phonon modes are involved because of the difference in mass of the electrons and holes and because the deformation potential interaction involves TO as well as LO modes. We should therefore consider four separate phonon populations viz. LO (electrons), LO (holes), TO (holes), TO (holes), and more if IP modes are involved. To avoid this complication we assume that we can work with a single set of phonon modes whose occupation is an average of the true LO and TO occupation numbers and whose associated emission and absorption rates are characterized by a single time constant τ . Such an assumption is relatively crude, but it does not seriously falsify the basic physics. We come back to this point later.

The equation describing energy relaxation is now

$$\frac{dU}{dt} = -\frac{\hbar\omega}{\tau} [n_e(\omega) - n(\omega)] N \hbar\omega - \nabla J_E. \quad (21)$$

where U is the total energy density of the electron-hole gas in a single well, ω is an average phonon frequency, $N/\tau = (N/\tau)_e + (N/\tau)_h$, and J_E is the energy current density. The latter may be related to the current density, J , as follows. The particle currents J_e and J_h are related to J via $J = eJ_e = eJ_h$, and thus $J_E = e(\Delta E_c J_e + \Delta E_v J_h)$, where ΔE_c and ΔE_v are the relevant band-edge discontinuities in the wells minus the subband energies. At steady state electrical neutrality entails that $J_e = J_h$ and hence $J_E = \eta \Delta E_g J/e$, where η is the injection efficiency. If d is the cavity width, the divergence of the energy current is $-\eta \Delta E_g J/2de$, and this corresponds to minus the rate of increase in energy density in the whole cavity. If there are N_w wells, the rate of increase in energy density in one well is therefore $\eta \Delta E_g J/e N_w L_w$.

For both degenerate electrons and holes, we have from Eq. (5),

$$U = \frac{n^2}{2N_e} \left[1 + \frac{\pi^2}{3} \left(\frac{k_b T_e N_e}{n} \right)^2 \right] + \frac{p^2}{2N_h} \left[1 + \frac{\pi^2}{3} \left(\frac{k_b T_h N_h}{n} \right)^2 \right]. \quad (22)$$

In the case of electrical neutrality and no background doping of significance, $n = p$, where

$$U = \frac{n^2}{2N_e} \left[1 + \frac{\pi^2}{3} \left(\frac{k_b T_e}{n} \right)^2 N_e N_h \right], \quad (23)$$

where N_e is the reduced density of states per unit energy interval, and $N_e N_h$ are the density of states per unit en-

ergy interval in the conduction and valence subbands. Equation (21) becomes

$$\frac{n}{N} \frac{dn}{dt} + \frac{\pi^2}{3} k_B^2 T_e (N_e + N_h) \frac{dT_e}{dt} = -\frac{\hbar\omega}{\tau} [n_e(\omega) - n(\omega)] N \hbar\omega + FJ, \quad (24)$$

where we have introduced an effective electric field $F = \eta \Delta E_g / e N_w L_w$, and n is the density of electrons (or holes) in a single well.

The phonon occupation is to be described by the following equation

$$\frac{dn(\omega)}{dt} = \Gamma_p \frac{\hbar\omega}{\tau} [n_e(\omega) - n(\omega)] \frac{N}{2n} - \frac{[n(\omega) - n_e(\omega)]}{\tau_p} \quad (25)$$

in which Γ_p is a factor less than unity introduced to allow for the diversity of phonon modes involved, and it can serve also to include effects due to differences of confinement. It will henceforth be referred to as the phonon mode factor.

Addition of the rate equations describing the photon flux density, S , and the electron density complete the set. These are

$$\frac{dS}{dt} = v \Gamma g S - \frac{S}{\tau_s}, \quad (26)$$

$$\frac{dn}{dt} = -v g S - \frac{n}{\tau_r} + \frac{\eta J}{e N_w L_w}, \quad (27)$$

where v is the group velocity of the photon, Γ is the photon confinement factor, g is the gain, τ_s is the photon lifetime, and τ_r is the spontaneous recombination lifetime. We have ignored the contribution of the spontaneous emission to the photon density rate. The gain is given by

$$g = g_{\max} [f(E_e) - f(E_h)], \quad (28)$$

$$g_{\max} = \frac{2e^2 m^* (p_{cv}^2 / 2m)}{\epsilon_0 m \hbar^2 \omega \eta_r c L_w}, \quad (29)$$

where m^* is the reduced electron-hole mass, p_{cv} is the momentum matrix element including spin selection, ϵ_0 is the permittivity of free space, m is the free electron mass, ω is the photon angular frequency, η_r is the refractive index, and c is the velocity of light in *vacuo*. For simplicity, line broadening has been ignored. For thermalized Fermi-Dirac distributions and $n=p$,

$$f(E_e) - f(E_h) = 1 - \exp[-n/N_e k_B T_e] - \exp[-n/N_h k_B T_e] \quad (30)$$

and thus a given gain determines the ratio $n/T_e = C$. At steady state, the gain is given in Eq. (26) by

$$g = \frac{1}{v \Gamma \tau_s} \quad (31)$$

and from Eq. (27),

$$S = \frac{1}{v g} \left[\frac{\eta J}{e N_w L_w} - \frac{n}{\tau_r} \right]. \quad (32)$$

The linear response of the coupled carrier-phonon-photon system can be obtained in the usual way, and noting that $dg/dT_e = -C dg/dn$. The response function turns out to be

$$R(\Omega) = \frac{\Omega_p^2 (1 + i\alpha\Omega - b\Omega^2)}{\Omega_p^2 - \Omega^2 + i\zeta\Omega - i\Omega^3 + e\Omega^4}, \quad (33)$$

where the relaxation angular frequency is given by

$$\Omega_p^2 = \frac{\Omega_0^2 (1 + f)}{\Delta} \quad (34)$$

with

$$\Omega_0^2 = v g_s S / \tau_s, \quad f = \frac{\Gamma_p k_B F J \tau_p}{2C(\hbar\omega)^2 n_e(\omega) [n_e(\omega) + 1]}, \quad (35a)$$

$$\Delta = 1 + \frac{\tau_p}{\tau_r} + \frac{\tau_T \tau^*}{\tau_r \tau} + \Omega_0^2 \left[\tau_p \tau_s + \tau_T \left(\tau_p + \frac{\tau_s \tau^*}{\tau} \right) (1 + r) \right]. \quad (35b)$$

Here $g_s = dg/dn$, $C = n/T_e$, $r = 3C^2/p^2 k_B^2 V_e V_h$, and

$$\tau_T = \frac{\pi^2}{3} \left(\frac{k_B T_e}{\hbar\omega} \right)^3 \frac{N_e N_h}{N_e N_h} \frac{\tau}{n_e(\omega) [n_e(\omega) + 1]}, \quad (36)$$

$$\tau^* = \tau + \frac{\Gamma_p N \hbar\omega \tau_p}{2 T_e C}. \quad (37)$$

τ_T is just a generalization of the temperature relaxation time of Eq. (17) and τ^* is essentially $\tau(1+\alpha)$. The other parameters in Eq. (33) are given by

$$a = \frac{\tau_p + (\tau_T/\tau) [\tau^* (1 + r - p) - p(\tau_T/\tau_r)]}{1 + f - p(\tau_T \tau^* / \tau \tau_r)}, \quad (38)$$

$$b = \frac{\tau_T \tau_p (1 + r - p)}{1 + f - p(\tau_T \tau^* / \tau \tau_r)}, \quad (39)$$

where $p = rN$, $\Delta E_g / T_e C$, which, like r and f , is dimensionless and

$$c = \frac{1}{\Delta} \left[\frac{1}{\tau_r} + \Omega_0^2 \left(\tau_p + \tau_s (1 + f) + \frac{\tau_T \tau^*}{\tau} (1 + r) \right) \right], \quad (40)$$

$$d = \frac{1}{\Delta} \left[\tau_p + \frac{\tau_T}{\tau} \left[\tau^* + \tau \left(\frac{\tau_s}{\tau_r} + \Omega_0^2 \tau_p \tau_s (1 + r) \right) \right] \right], \quad (41)$$

$$e = \frac{\tau_T \tau_p}{\Delta}. \quad (42)$$

Several new factors enter the above analysis. First, to calculate the response function [Eq. (33)], one notes that the cavity losses determine the gain according to Eq. (31), which in turn determines $C = n/T_e$ for all currents above threshold. A choice of T_e then determines n and all the other steady state quantities including the current density and the differential gain. Since g_s decreases with increasing T_e , this phenomena is a source of nonlinear gain. The occupation numbers, $n(\omega)$ and $n_e(\omega)$, are determined under steady-state conditions from Eqs. (13) and (21), respec-

tively. The new factors, f , r , and p are all dimensionless. The first, f , may be termed the injection hot-phonon factor; it is a measure of the energy injected into the phonon system and hence of the increase of phonon number in a mode. The second factor, r , is the recombination-heating coefficient; it is a measure of the rise in temperature associated with a fall in carrier density. The third factor, p , is the direct-heating coefficient, which is a measure of the rise in temperature associated with the injected energy. A notable pattern in the expressions for a and b [Eqs. (38) and (39)] is the term $(1+r-p)$. This reflects the variation of photon density with carrier density and temperature, as these vary with current density. Thus, increasing current density results in increasing carrier density, which manifests itself as the unity in the expression. Increasing temperature reduces photon density hence the negative sign of p , and the positive sign of r reflects the fact that increasing carrier density induces cooling. These are thus competing mechanisms at work here.

The above response is significantly more complex than the standard one obtained by neglecting carrier heating altogether. To obtain the standard result it is necessary to eliminate both sources of heating—recombination and injection. The latter is zero if $F=0$, where $f=0$ and $p=0$. It is interesting that this does not produce much simplification. This points to the main source—recombination heating. To eliminate this means making both τ and τ_p approach zero—letting only τ_p approach zero merely diminishes hot-phonon effects, and letting only τ approach zero merely emphasizes the role of hot phonons. If this is done, $a=b=d=e=0$, and the standard result is obtained *viz.*

$$R(\Omega) = \frac{\Omega_0^2}{\Omega_0^2 - \Omega^2 + i\Omega} \quad (43)$$

with $c = \tau^{-1} + \Omega_0^2 \tau_p$.

The free oscillations of the system, corresponding to the response to a sudden increase in current density when a voltage step is applied, is described by entailing that the denominator in Eq. (33) vanish. Replacing Ω by $\Omega + i\gamma$ gives two equations which determine the relaxation frequency and the damping rate, *viz.*:

$$e\Omega^4 - \Omega^2(1 + 6\gamma^2 e - 3\gamma d) - \Omega^2 - \gamma c + \gamma^2 - d\gamma^3 + e\gamma^4 = 0, \quad (44a)$$

$$4e\gamma^3 - 3d\gamma^2 + 2\gamma(1 - 2e\Omega^2) - c - d\Omega^2 = 0. \quad (44b)$$

These equations are most easily solved numerically. At low drives there exists a fast solution which is approximately given by

$$\Omega^2 = \frac{1}{e} + 2\gamma^2, \quad \gamma = \frac{3d}{4e}, \quad (45)$$

which describes the temperature relaxation process. There is also a slow solution, which is very roughly given by

$$\Omega^2 = \frac{(2 + 3cd)\Omega_p^2 - c^2}{2 - cd}, \quad \gamma = \frac{c - d\Omega_p^2}{2(1 + cd)}. \quad (46)$$

The departure from ideal behavior is often described in terms of a nonlinear gain coefficient ϵ_{nl} such that $g = g_0/(1 + \epsilon_{nl}S)$. The parameter ϵ_{nl} is found from the ratio of the damping rate γ to the square of the resonance frequency, Ω_p^2 . This ratio, usually named K , is proportional to ϵ_{nl} at low drives. From Eq. (46)

$$K = 2\pi^2 \frac{(c - d\Omega_p^2)(2 - cd)}{(1 - cd)[(2 - 3d)\Omega_p^2 - c^2]}. \quad (47)$$

In the limit of small current densities

$$K = \frac{2\pi^2 c}{\Omega_0^2 - c^2/2} \approx 2\pi^2 \left(\tau_s + \tau_p + \frac{\tau_{70}\tau_0^*}{\tau} (1 + r) \right), \quad (48)$$

where τ_0^* and τ_{70} are the time constants when the carrier temperature equals that of the lattice. Small-signal analysis gives $K = 2\pi^2(\tau_s + \epsilon_{nl}/vg_{on})$ and so, comparing with Eq. (48), we obtain

$$\epsilon_{nl} = vg_{on} \left(\tau_p + \tau_{70} \frac{\tau_0^*}{\tau} (1 + r) \right), \quad (49)$$

where g_{on} is the linear differential gain. At room temperature the total time constant in the brackets is typically about 8 ps, and so with $g_{on} \approx 10^{-15} \text{ cm}^2$, $\epsilon_{nl} \approx 10^{-17} \text{ cm}^3$, which is the order typically observed. However, at high drives the nonlinear effects cannot be characterized by a single constant parameter, as a perusal of Eq. (47) indicates, and it is not possible to distinguish fast solutions and slow solutions as clearly. Generally we can expect the frequency observed in relaxation oscillations to be different from that of the peak of the frequency response.

IV. APPLICATION TO GaAs/Ga_{1-x}In_xAs STRAINED-LAYER LASERS

We consider the system in which $x=0.3$. Nothing definite is known about the strength of electron and hole interactions with optical modes in this system. An estimate can be made along the following lines. Band-structure calculations, supported by the results of magneto-optical experiments, suggest that the electron and hole masses in the lowest subbands are about equal and thus the strengths of the electron and hole Fröhlich interactions should be about equal if the hole overlap integral is unity. The latter should be true since the hole subband has in-plane symmetry at energies sufficiently removed from the next higher subband. In GaInAs lattice-matched to InP ($x=0.53$) it is known that the Fröhlich interaction is much stronger for the GaAs-like mode than for the InAs-like mode,¹⁵ so we ignore the effect of this latter mode. For $x=0.3$ the GaAs-like LO mode has an energy of about 34 meV compared with 36 meV in GaAs, and thus will be essentially unconfined. (GaAs modes with energies between 34 and 36 meV will be confined in the barriers to some extent.) Thus the interaction can be approximated by a 2D carrier interacting with bulk-like LO modes. (Complications associated with interface polariton and hybridization will be ignored.) From the results of Nash *et al.*¹⁵ we deduce a coupling

parameter α_{LO} of 0.055 (compared with 0.068 for GaAs) and hence a characteristic basic time constant τ_0 of 175 fs where

$$\frac{1}{\tau_0} = 2\alpha_{LO}\omega. \quad (50)$$

Comparison with bulk rates suggests that for an electron with energy $\frac{1}{2}\hbar\omega$ and higher. This is the corresponding scattering time and this is also true for quantum wells.¹⁶

In a working laser with carrier densities exceeding 10^{18} cm^{-3} , it is necessary to take screening into account. The 2D plasma frequency is approximately

$$\omega_p^2 = \frac{(2\pi)e^2qL_w}{2m^* \epsilon}, \quad (51)$$

where $2n$ is the electron plus hole densities, $\epsilon = \epsilon_s$ if $\omega_p > \omega_{LO}$, and $\epsilon = \epsilon_s$ if $\omega_p < \omega_{LO}$, ϵ_s , ϵ_h are the high-frequency and static permittivities, and q is the wave vector of the 2D plasma wave. Taking q to be the wave vector $q_\omega = (2m^*\omega/\hbar)^{1/2}$, about which the allowed in-plane wave vectors of LO modes distribute themselves, $\omega_p = \omega_{LO}$ for $L_w = 50 \text{ \AA}$ when $n \approx 3 \times 10^{17} \text{ cm}^{-3}$. Since typical densities are over 10^{18} cm^{-3} we can assume $\omega_p > \omega_{LO}$ and as a crude approximation assume that the screening is static, which implies reducing the Fröhlich rate by a factor involving q_ω and the screening vector, $q_s = e^2m^*/\pi\epsilon_s\hbar^2$ (normal expression $\times 2$ for electrons + holes) viz.:

$$\frac{1}{\tau_F} = \frac{1}{\tau_0} \frac{1}{[1 - (q_s/q_\omega)(2/3)]}, \quad (52)$$

where the factor $\frac{1}{3}$ takes into account that only phonons traveling in the plane are screened. This increases the time constant to 368 fs.

Being short-range, the deformation potential interaction is not as affected by screening. The scattering rate in an infinitely deep well is¹⁷

$$\frac{1}{\tau_p} = \frac{3D_0^2 m^*}{4\rho\pi^2\omega L_w}, \quad (53)$$

where D_0 is the deformation potential constant and ρ is the mass density. With $D_0 = 7 \times 10^4 \text{ eV cm}^{-1}$ and $L_w = 50 \text{ \AA}$, $\tau_p = 2.61 \text{ ps}$. Unfortunately an accurate expression for D_0 is not available—the value chosen here is that for the L valleys in Ge—but clearly some inaccuracy here will be relatively unimportant in view of the relative weakness of this interaction.

In Eq. (21) we can now express the total scattering rate, taking into account our assumption that $N_e = N_h$, as follows:

$$\frac{1}{\tau} = \frac{2}{\tau_F} + \frac{1}{\tau_p}. \quad (54)$$

whence $\tau = 170 \text{ fs}$. In these processes the same set of phonon modes is involved in both the electron and hole Fröhlich scattering, and is roughly one third of the non-polar scattering. Thus a fraction $[(2/\tau_F) + (1/\tau_p)]\tau$, that is, 0.946, of scattering processes involve the same set of phonon modes, i.e., the LO modes, and so we can regard

TABLE I. Material parameters

m^*/m_e	0.07	τ_p	4 ps
$\hbar\omega$	34 meV	τ_{max}	6700 cm^{-1}
τ	170 fs	τ_F	3.6
L_w	50 \AA	Γ	0.086
L_b	250 \AA	τ_p	1 ps
V_s	5	τ_p	2 ns
Γ_p	0.158		

the effects of hot TO phonons as being negligible. As regards confinement it is not possible, in the absence of any theoretical study of optical modes in this system, to do anything other than offer a crude estimate. Although we expect the GaAs-like LO modes to be relatively unconfining, this does not mean we can confidently give equal weight to well and barrier and accept a confinement factor of the form $L_w/(L_w + L_b)$; where L_w , L_b are the widths of the well and barrier, because the frequency mismatch between well and barrier will result in there being different amounts of oscillator strength in the well and barrier. Nevertheless, for consistency of the model—the scattering has been assumed to be via bulk-like modes—we will ignore this aspect and use the simple form mentioned above. This means that the phonon mode factor introduced in Eq. (25) is

$$\Gamma_p = \left(\frac{2}{\tau_F} + \frac{1}{3\tau_D} \right) \tau \frac{L_w}{L_w + L_b}. \quad (55)$$

The phonon lifetime has been taken to be the same as in GaAs at room temperature.¹⁸ Other parameters are listed in Table I. We consider the response of a laser containing five quantum wells, 100 μm long. The maximum gain (cm^{-1}) was obtained from Eq. (29) with $p_{cr}^2/2m = 2.3 \text{ eV}$, being the value for GaAs multiplied by the ratio of the photon energy to the GaAs band gap. This calculation assumed an injection efficiency of 100% and a threshold current density of 280 A/cm^2 . Figure 1 shows the square modulus of the response function [Eq. (33)] for the ideal case (no carrier heating) and in Fig. 2 for different

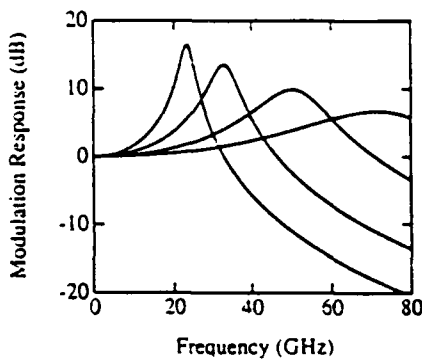


FIG. 1. Ideal frequency response. The current density (10^4 A cm^{-2}) and light intensity (MW cm^{-2}) respectively for each curve are, in order of peak frequency: (1) 0.375, 1.19; (2) 0.725, 2.39; (3) 1.70, 5.74; (4) 3.62, 12.3.

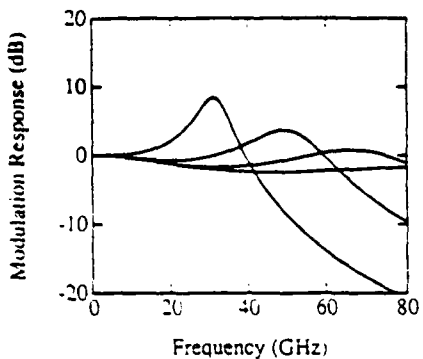


FIG. 2. Frequency response with $\Delta E_g = 0.30$ eV. The carrier temperature (K), current density (10^4 A cm $^{-2}$), and light intensity (MW cm $^{-2}$), respectively, are in order of peak frequency: (1) 310, 0.648, 2.12; (2) 325, 1.70, 5.74; (3) 350, 3.62, 12.3; (4) 400, 8.11, 27.7.

steady-state carrier temperatures when the lattice temperature is 300 K and $\Delta E_g = 300$ meV. Comparison with observed responses in a 100 μ m cavity length, 5 well laser in Fig. 3¹⁹ shows that the model qualitatively describes the trends reasonably well. (We discuss the quantitative aspects later.) Figure 4 shows the square of the peak frequency (ω_{peak}^2) as a function of photon density for different levels of injected energy. From this plot, we can see that as the injection energy rises, the peak frequency is increasingly suppressed at high photon densities. Modeling these responses according to the simple nonlinear gain model described above, we obtain nonlinear gain coefficients of 3.5×10^{-17} and 8.3×10^{-17} cm 3 for $\Delta E_g = 0.3$ and 0.75 eV, respectively. Without carrier heating these responses would be a straight line as demonstrated by the ideal performance. In fact, at low photon densities, a straight line is obtained at low current densities for all injected energies, which goes some way in explaining the linear behavior observed by Lester *et al.*¹⁹ We should further point out that the relaxation frequency of Eq. (34) is not a good guide to what frequencies are attainable. Its variation with photon density is virtually independent of the injected energy, being principally determined by the characteristic time constants of the system.

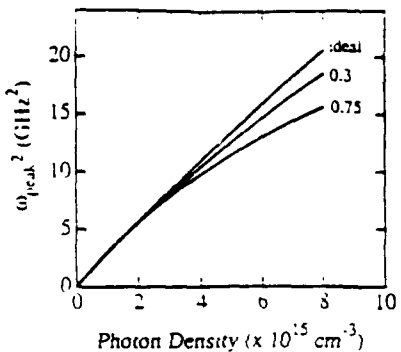


FIG. 4. Squared angular frequencies as a function of photon density (10^{15} cm $^{-3}$). The curves are (from top down) (1) ideal, (2) $\Delta E_g = 0.30$ eV, and (3) $\Delta E_g = 0.75$ eV.

Figure 5 shows the response when $\Delta E_g = 0$, i.e., zero energy input. In this case the steady-state temperature stays at 300 K for all input current densities, but recombination heating and hot-phonon effects are still present. Note that the sag at low frequencies has been eliminated. Figure 6 shows the response for $\Delta E_g = 0.75$ eV, corresponding to higher barriers, which turns out to be similar to that for $\Delta E_g = 0$, though the low-frequency sag has returned, but in a much reduced form. At first sight this is a surprising result—one expects that pumping in more energy would make things worse—but this is not the case. In fact the situation with $\Delta E_g = 0.3$ eV is worse than either of the others. The cause of this peculiar behavior is to be found in the factor $(1+r-p)$ discussed earlier. Basically, the response is damped by the processes of photon loss, phonon loss, and recombination heating, all of which contribute an effective time constant of about 10 ps, and this determines the magnitude of the factor c in the denominator of $R(\omega)$. This damping is offset to some degree by the factors a and b in the numerator. Where c is only weakly dependent on ΔE_g via the factor f , this is not so for a and b , both of which are heavily dependent on the factor $(1+r-p)$. When the latter is negative, the frequency dependence of the numerator under some circumstances can be small, and so the damping effects are maximum. This cu-

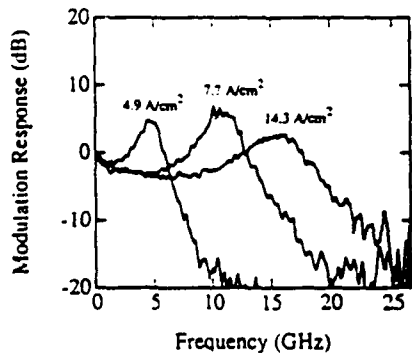


FIG. 3. Observed frequency response of a $100 \times 5 \mu\text{m}^2$, five quantum well strained layer laser (see Ref. 19).

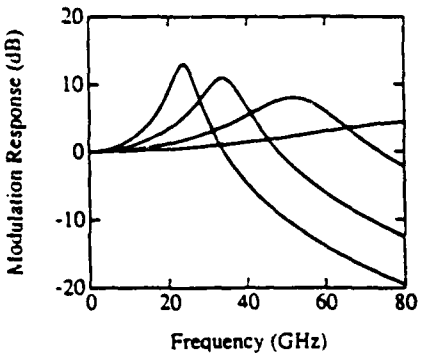


FIG. 5. Frequency response with $\Delta E_g = 0$. Current densities and light intensities as for the ideal case (Fig. 1).

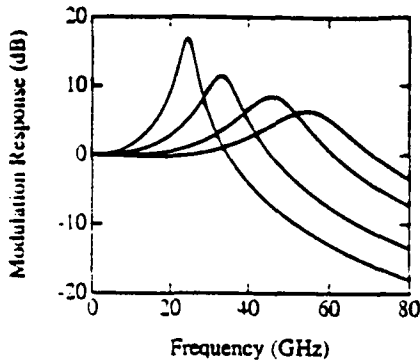


FIG. 6. Frequency response with $\Delta E_g = 0.75$ eV. The carrier temperature (K), current density (10^6 A cm $^{-2}$), and light intensity (MW cm $^{-2}$), respectively, and are in order of peak frequency: (1) 325, 0.375, 1.08; (2) 350, 0.725, 2.16; (3) 400, 1.63, 5.69; (4) 450, 2.66, 9.27.

rious behavior reflects the competition between recombination cooling and injection heating in a degenerate gas.

Because of the simplification and approximations adopted in the model and in its application to the GaAs/Ga_{0.7}In_{0.3}As system, it is interesting to see the effect of varying some of the magnitudes which enter the response. Figure 7 shows the result of doubling the scattering time constant and the phonon lifetimes for the case when $\Delta E_g = 0.3$ eV. Although some reduction in frequency occurs

the main effect is to enhance the low frequency droop and generally to damp the response. Many factors can reduce the differential gain and Fig. 7 also illustrates the effect of reducing g_n by a factor of 2 and maintaining the longer time constants. The frequency at peak response is reduced as expected by a factor of roughly $\sqrt{2}$, and the droop is greatly enhanced, giving response curves much nearer to those observed.¹⁹

V. DISCUSSION

The model chosen by us to illustrate the effects of carrier heating contains many simplifying features. These include equal electron and hole masses, parabolic bands, infinitely deep wells, instantaneous thermalization within the gas of carriers, the applicability of degenerate statistics, and the neglect of level broadening and lattice heating. Close quantitative agreement with published work was not obtained and was not expected, but we hope we have shown that carrier heating produces complex effects that simulate the main elements of nonlinear gain, although it is pointed out that these effects cannot be quantified in terms of a single phenomenological factor, ϵ_{nl} . Thus, the relaxation frequency observed in a pulse experiment is affected differently by nonlinearity than is the frequency of maximum response. Moreover, the droop in response at low frequencies caused by injection heating is not described by the usual phenomenological expression for nonlinearity. This is not surprising in view of the intricate interplay of the dynamics of injection heating, recombination heating, and phonon heating. Interestingly, the frequency response remains useful out towards 100 GHz, which suggests that carrier heating itself need not be a limitation. This is important since the use of quantum wells entails the fact of injection heating, although as we have illustrated in Fig. 5, even without injection heating the process of recombination heating with hot phonons is present and introduces "nonlinear gain" effects. Nevertheless, the amount of injection heating is a function of the material structure of the laser and is therefore manipulable in principle.

In our illustration the differential gain (g_n) was between 2 and 3×10^{-15} cm $^{-2}$. Although differential gains of this magnitude have been reported, the more usual figures found are a factor of 2 or 3 smaller. Lower gains can easily come about through the combined effect of nonparabolicity, lifetime broadening, finite well depth, well width fluctuations, and hole burning. Another important variable is the injection efficiency (η). There can be significant loss of carriers in ridge lasers by sideways diffusion and in mesa lasers by surface recombination. Probably η in small lasers does not exceed 0.80 and may be as low as 0.5.

Another simplifying assumption is that of instantaneous thermalization. As long as the electron and hole masses are about equal, this assumption is not likely to lead to major error as far as intrasubband processes are concerned. However, the large momentum change involved in intersubband transitions—including the process of well capture—may introduce further time constants of the order of 1–10 ps. The population in each subband would then have to be considered individually, leading to a signifi-

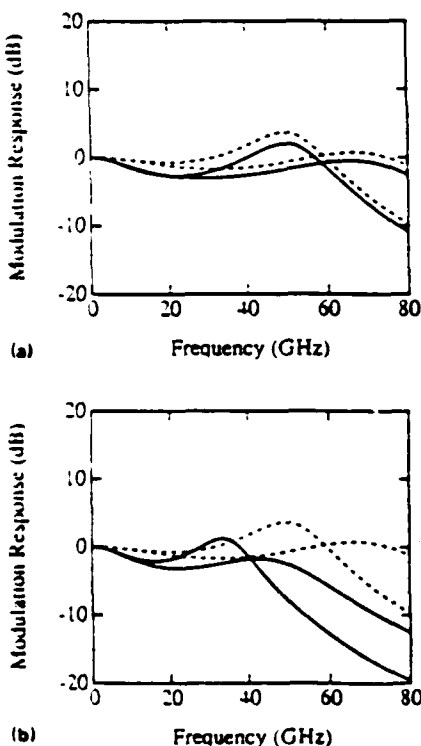


FIG. 7. Frequency response for $\Delta E_g = 0.30$ eV with longer time constants and a lower differential gain. (a) Scattering time $\tau = 340$ fs and $\tau = 8$ ps. (b) As (a) but in addition, a halved differential gain. The dashed curves represent responses at the same current density, but with the time constants and differential gain as in Fig. 2.

ently enhanced complexity. This aspect needs further investigation, but it is unlikely that the effective relaxation time constant—in our present model, of magnitude 20 ps—would be increased beyond 20 ps. Figures 7(a) and 7(b) illustrate the degradation in the frequency response when time constants are long and the differential gain is weak for the case in which $\Delta E_3 = 0.3$. As can be seen in Fig. 7(a), longer time constants do not produce a shift in the resonance peak, but do significantly exacerbate the sag in the modulation response. Figure 7(b) shows the expected result that the resonance peak changes with the square root of the differential gain.

There are several factors like those mentioned above that make realistic modeling difficult, but there is one factor we have yet to mention which is of prime importance to the achievement of high-frequency performance, and that is the photon flux intensity which the laser can support without being damaged. Because we have wished to illustrate carrier heating effects, we have chosen high current densities with corresponding photon flux intensities in the range 1–30 MW cm⁻², but it is rare to find real lasers with damage thresholds much above 10 MW cm⁻². It is likely that this damage threshold, rather than carrier (or even lattice) heating, which will determine the bandwidth of the laser.

In summary, we have presented a model of carrier heating, that incorporates recombination heating, injection heating, and hot-phonon effects, and have applied the model to the case of a quantum well laser and its frequency response. Carrier heating was shown to lead to nonlinear gains and to a modified frequency response. Application to the GaAs/InGaAs strained layer laser showed that a characteristic relaxation time constant of order 10 ps determined the behavior, and this time constant was derived from the phonon lifetime and the temperature relaxation time in the degenerate population in addition to the more familiar photon lifetime. It was pointed out that a distinction between the frequency of relaxation oscillations and the frequency of maximum response must be drawn, and that the various nonlinear effects could not be quantita-

tively described satisfactorily with a single nonlinear gain parameter. It was shown that the combination of weak gain and long relaxation times can have a devastating effect on the frequency response.

ACKNOWLEDGMENTS

It is a pleasure to acknowledge the help and guidance of Professor Lester Eastman with many discussions on this topic. One of us (BKR) is once again indebted to his hospitality at Cornell. The project was supported by U.S. Army Grant DAAL01-89-C-0927, GE Electronics Laboratory, DARPA, and ONR.

- ¹V. I. Malakhova, A. G. Plyavenek, L. A. Rivlin, S. I. Filiminov, and S. D. Yakubovich, Sov. J. Quantum Electron. **18**, 442 (1988).
- ²J. Nagel and C. Weisbuch, SPIE **943**, 76 (1988).
- ³B. N. Gomati and A. P. DeFonzo, IEEE J. Quantum Electron. **26**, 1689 (1990).
- ⁴M. Willatzen, A. Uskov, J. Mork, H. Oleson, B. Tromborg, and A. P. Janho, IEEE Photon. Tech. Lett. **3**, 606 (1992).
- ⁵J. Nagel, S. Hersee, M. Razeghi, M. Krakowski, B. de Cremoux, and C. Weisbuch, Surf. Sci. **174**, 148 (1986).
- ⁶M. P. Kester and E. P. Ippen, Appl. Phys. Lett. **51**, 1765 (1987).
- ⁷B. K. Ridley, J. Appl. Phys. **68**, 4667 (1990).
- ⁸B. K. Ridley, Rep. Prog. Phys. **54**, 169 (1991).
- ⁹D. Bimberg and J. Mycielski, Phys. Rev. **31**, 5490 (1985).
- ¹⁰D. Bimberg and J. Mycielski, J. Phys. C: Solid State Phys. **19**, 2363 (1986).
- ¹¹J. M. Rorison and D. C. Herbert, J. Phys. C: Solid State Phys. **19**, 3991 (1986).
- ¹²S. M. Goodnick and P. Lugli, Solid-State Electron. **31**, 463 (1988).
- ¹³W. Potz, M. A. Osman, and D. K. Ferry, Solid-State Electron. **31**, 673 (1988).
- ¹⁴C. W. W. Bradley, R. A. Taylor, and J. F. Ryan, Solid-State Electron. **32**, 1173 (1989).
- ¹⁵K. J. Nash, M. S. Skolnick, and S. J. Bass, Semicond. Sci. Technol. **2**, 329 (1987).
- ¹⁶F. A. Riddoch and B. K. Ridley, J. Phys. C Solid State Phys. **16**, 6971 (1983).
- ¹⁷B. K. Ridley, J. Phys. C Solid State Phys. **15**, 5899 (1982).
- ¹⁸D. von der Linde, J. Kuhl, and H. Klinzinger, Phys. Rev. Lett. **44**, 1505 (1980).
- ¹⁹L. F. Lester, W. J. Schaff, X. Song, S. D. Offsey, and L. F. Eastman, Proc. IEEE Cornell Conf., Ithaca, NY, (IEEE New York, 1991), p. 221.